

APPLICATIONS OF VARIATIONAL PARTIAL DIFFERENTIAL EQUATION
MODELS IN MEDICAL IMAGE PROCESSING

By

FENG HUANG

A DISSERTATION PRESENTED TO THE GRADUATE SCHOOL
OF THE UNIVERSITY OF FLORIDA IN PARTIAL FULFILLMENT
OF THE REQUIREMENTS FOR THE DEGREE OF
DOCTOR OF PHILOSOPHY

UNIVERSITY OF FLORIDA

2004

Copyright 2004

by

Feng Huang

To my parents and my wife.

ACKNOWLEDGMENTS

I wish to express my sincere and deepest appreciation to my advisor, Professor Yunmei Chen, for her guidance, advice and support throughout my graduate study at UF. Her enthusiasm, patience and intelligence have helped me achieve more in my studies. I would like to thank other members of my committee (David Wilson, Scott McCullough, Murali Rao, Yijun Liu and Randy Duensing) for their help, valuable suggestions and kind encouragement. I would also like to thank my colleagues for their support and discussions on various topics. Thanks go to Sheshadri Thiruvankadam, James Akao, Charley Saylor, Weihong Guo, Andrew Rubin, Jungha An, Xiqiang Zheng.

Chapter 2 was the result of collaboration with Yunmei Chen, Murali Rao, David Wilson, Sheshadri Thiruvankadam, Weihong Guo, Jungha An, Hemant D. Tagare and Edward A. Geiser. Several publications based on the work in this chapter. Chapter 3 is a joint work with Yunmei Chen, Randy Duensing, Charley Saylor, James Akao and Scott McCullough. The work was submitted to IEEE Transaction on Medical Imaging. Chapter 4 was coauthored with Yunmei Chen, Randy Duensing, James Akao and Andrew Rubin. The work was submitted to Magnetic Resonance on Medicine. Chapter 5 was written in collaboration with Yunmei Chen, Yijun Liu, Weihong Guo, Qingguo Zeng, Xiqiang Zheng, Guojun He and Xiaolu Yan.

This work was supported in part by Invivo Corporation (Gainesville) and McLaughlin Dissertation Fellowship.

TABLE OF CONTENTS

	<u>page</u>
ACKNOWLEDGMENTS	iv
LIST OF TABLES	ix
LIST OF FIGURES	x
LIST OF ABBREVIATIONS	xii
ABSTRACT	xiv
CHAPTER	
1 INTRODUCTION	1
1.1 Motivating Applications	2
1.1.1 Segmentation of Ultrasound Cardiac Image	2
1.1.2 Noise Tomography	2
1.1.3 Calibration of Sensitivity Map	3
1.1.4 Intensity Correction	4
1.1.5 Fiber Tracking	5
1.2 Review of Conception	6
1.2.1 Description of General Tomography Problem	6
1.2.2 Mumford-Shah Model	6
1.2.3 Total Variation Denoising	7
1.2.4 Level Set	8
1.2.5 Distance Function	10
1.2.6 Mutual Information	11
1.2.7 Inpainting	12
1.3 Numerical Techniques	13
1.3.1 Choice of Heaviside Function	13
1.3.2 Computation of $\kappa = \operatorname{div} \frac{\nabla u}{ \nabla u }$	13
1.3.3 Initial Signed Level Set and Reinitialization	14
1.3.4 Fast Sweep Method for Level Set Based Optimization	15
1.4 Contributions of Our Study	16
1.4.1 Segmentation with Prior Information	16
1.4.2 Inpainting	16

1.4.3	Modified Mumford-Shah Model for Tomography.....	17
1.4.4	Fiber Tracking.....	18
2	SEGMENTATION WITH PRIOR INFORMATION.....	19
2.1	Introduction.....	19
2.1.1	Definition of Segmentation.....	19
2.1.2	Importance of Segmentation in Medical Applications.....	19
2.1.3	Review of Segmentation Methods.....	21
2.1.4	Remaining Problems in Existing Methods.....	24
2.2	Method.....	24
2.2.1	Generation of Prior Information.....	24
2.2.1.1	Shape analysis.....	25
2.2.1.2	Intensity profile.....	28
2.2.2	Framework Description.....	31
2.2.2.1	Gradient term.....	32
2.2.2.2	Shape term.....	34
2.2.2.3	Key points term.....	36
2.2.2.4	Intensity profile term.....	38
2.2.2.5	Proposed model and Euler-Lagrange equations.....	40
2.2.3	Parameter Choosing.....	42
2.3	Experiments and Results.....	43
2.3.1	Shape Analysis.....	44
2.3.2	Intensity Profile.....	45
2.3.3	Segmentation with Prior Shape Information.....	47
2.3.3.1	Synthetic image.....	48
2.3.3.2	Cardiac ultrasound images.....	49
2.3.4	Segmentation with Prior Shape Information and Key Points.....	50
2.3.4.1	Synthetic image.....	50
2.3.4.2	Cardiac image.....	52
2.3.5	Segmentation with Prior Shape and Intensity Profiles.....	57
2.4	Conclusion.....	65
3	APPLICATION OF PDE BASED INPAINTING ON MR PARALLEL IMAGING.....	68
3.1	Introduction.....	69
3.1.1	Inpainting.....	69
3.1.2	Sensitivity Maps.....	69
3.1.3	Intensity Correction Map.....	70
3.2	Methods.....	71
3.2.1	Review of TV Inpainting Model.....	72
3.2.2	Modification of the Exponent of $ \nabla u $ in the TV Model.....	73
3.2.3	Modified TV Model for Sensitivity Maps.....	74
3.2.4	Numerical Implementation Method.....	75
3.2.5	Modified TV Model for Intensity Correction Map.....	78

3.3	Experiments and Results.....	78
3.3.1	Application on Sensitivity Map.....	78
3.3.1.1	Phantom with no intrinsic holes.....	80
3.3.1.2	Coronal phantom.....	81
3.3.1.3	Neurovascular images.....	84
3.3.1.4	Cardiac images.....	85
3.3.2	Application on Intensity Correction Map.....	88
3.3.2.1	Uniformity scheme.....	88
3.3.2.2	Phantom.....	90
3.3.2.3	Clinical images.....	91
3.4	Conclusion.....	93
4	MODIFIED MUMFORD-SHAH MODEL FOR MEDICAL TOMOGRAPHY.....	95
4.1	Background of Tomography.....	95
4.1.1	Existing Methods.....	96
4.1.2	Motivation of the Proposed Framework.....	100
4.2	Proposed Model.....	101
4.2.1	Description of the Proposed Model.....	101
4.2.2	Level Set Forms in Different Cases.....	102
4.2.2.1	Binary field model.....	102
4.2.2.2	Piecewise constant model.....	103
4.2.2.3	Piecewise texture model.....	106
4.2.2.4	General piecewise smooth model.....	106
4.2.2.5	Model for tomography with guiding image.....	108
4.3	Application on Noise Tomography.....	110
4.3.1	Introduction of Noise Tomography.....	110
4.3.2	Electronic Noise.....	110
4.3.3	Intercoil Noise Correlation.....	112
4.3.4	Relation with Tomography Models.....	113
4.3.5	Experiments and Results.....	113
4.3.5.1	Experiment in one dimension.....	113
4.3.5.2	Experiment in two dimensions.....	114
4.3.5.3	Experiment in two dimensions with guiding image.....	116
4.3.5.4	Experiment in two dimensions with guiding image by fast sweeping.....	117
4.4	Conclusion.....	118
5	FIBER TRACKING BY FRONT PROPAGATION.....	120
5.1	Introduction.....	120
5.1.1	Understanding the Basis of DTI.....	123
5.1.2	Existing Fiber Reconstruction Methods.....	125
5.1.2.1	Line propagation algorithms.....	126
5.1.2.2	Front evolution methods.....	129
5.1.3	Several Considerations in Fiber reconstruction.....	130
5.1.3.1	Termination criteria.....	130

5.1.3.2 Effect of noise	132
5.1.3.3 Branching	132
5.1.3.4 Algorithms to interpolate a tensor field.....	132
5.1.3.5 Display of experimental tracks.....	133
5.1.4 Limitations of Existing Methods	134
5.2 Methods	135
5.2.1 Motivations of the Proposed Method	135
5.2.2 Data Description.....	138
5.2.2 Front Evolution and Path Record	138
5.2.4. Tracking Back	140
5.3 Experiments and Results.....	141
5.4 Conclusion	143
LIST OF REFERENCES.....	145
BIOGRAPHICAL SKETCH	156

LIST OF TABLES

<u>Table</u>	<u>page</u>
2-1 Experiment results with different λ for Epi	59
2-2 Experiment results with different λ for Endo	63
3-1 The relative error of inpainted results	81
3-2 Ghost ratio of coronal phantom.....	84
3-3 Ghost ratio of neurovascular images.....	85
3-4 Ghost ratio of cardiac images by applying high-resolution sensitivity maps of first image.....	87
3-5 Ghost ratio of cardiac images by applying low-resolution sensitivity maps of each image.....	88

LIST OF FIGURES

<u>Figure</u>	<u>page</u>
1-1 Level set	9
2-1 Examples of segmentation for cardiac images.....	20
2-2 Cluster and average result.	45
2-3 Example of average shapes of abnormal clusters.....	45
2-4 Twenty training images with the segmented epicardiums	46
2-5 Average images of the above 20 images with the average contour superimposed. .	47
2-6 Segmentation with prior shape for synthetic image.....	49
2-7 Segmentation with prior shape for cardiac image.....	50
2-8 Segmentation with prior shape and key points for synthetic image.....	52
2-9 Segmentation with prior shape and key points for cardiac image 1.....	54
2-10 Segmentation with prior shape and key points for cardiac image 2.....	56
2-11 Segmentation with prior shape and intensity profile for epicardiums.	61
2-12 Intensity profile for endocardiums.....	62
2-13 Segmentation results for endocardiums.	64
3-1 Inpainting results for the artificial holes.....	81
3-2 Inpainting results for coronal phantom.	83
3-3 Inpainting results for neurovascular images.....	85
3-4 The flow chart of the intensity correction method.	89
3-5 Intensity correction for phantom.	92
3-6 Intensity correction results for clinical neurovascular images.....	93

4-1	Experiment result in 1 dimension.....	114
4-2	Experiment result in 2 dimensions.....	115
4-3	Experiment result in 2 dimensions with ideal guiding image.....	117
4-4	Experiment result in 2 dimensions with real MR guiding image.....	117
4-5	Reconstructed image by fast sweeping	118
5-1	White matter structure and its relationship with the information provided by DTI.....	122
5-2	Linear line-propagation approach... ..	127
5-3	White matter fiber trajectory as a space curve	128
5-4	Flow chart of fiber tracking by fast marching on grids.....	141
5-5	Fiber tracking results.....	143

LIST OF ABBREVIATIONS

AAM: active appearance models	GPR: ground penetrating radar
ART: algebraic reconstruction technique	HARD-MRI: high angular resolution diffusion magnetic resonance imaging
BV: bound variation	LV: left ventricular
CT: computed tomography	MAP: maximum a posteriori
DTI: diffusion tensor imaging	MIIG: mutual information of image geometry
DWI: diffusion weighted imaging	MMSLS: modified mumford-shad model by level set
ECT: emission computed tomography	MRA: magnetic resonance angiography
ED: end diastole	MRI: magnetic resonance imaging
EIT: electrical impedance tomography	MR-NT: magnetic resonance image guided noise tomography
Endo: endocardial	NEMA: national electrical manufacturers association
EPI: echo planar imaging	NT: noise tomography
Epi: epicardial	OSEM: ordered subsets expectation maximization
ES: end systole	PDE: partial differential equation
FBI: fresh blood imaging	PET: positron emission tomography
FBP: filtered back projection	RF: resonance frequency
FIESTA: fast imaging employing steady-state acquisition	SENSE: sensitivity encoding
fMRI: functional magnetic resonance imaging	
FOV: field of view	
GKS: Gaussian kernel smoothing	

SMASH: simultaneous acquisition of
spatial harmonics

SNR: signal to noise ratio

SOS: sum of squares

SPECT: single phantom emission
computed tomography

TE: echo time

TR: transmit time

TV: total variation

Abstract of Dissertation Presented to the Graduate School
of the University of Florida in Partial Fulfillment of the
Requirements for the Degree of Doctor of Philosophy

APPLICATIONS OF VARIATIONAL PARTIAL DIFFERENTIAL EQUATION
MODELS IN MEDICAL IMAGE PROCESSING

By

Feng Huang

December 2004

Chair: Yunmei Chen
Major Department: Mathematics

Images of various kinds are increasingly important to medical diagnostic processes. Difficult problems are encountered in selecting both the most appropriate image reconstruction methods and post-processing methods. Reconstruction methods involve producing optimal quality images from raw data. Post-processing methods involve acquiring the highest quality information from these images. Medical image processing (i.e., reconstruction and post processing) has created tremendous opportunities for mathematical modeling, analysis, and computation.

I examined various applications of the variational partial differential equation (PDE) method. This method is one of the most recent and successful approaches to medical image processing. I worked on the following important medical image processing problems: clustering, denoising, segmentation, registration, tomography, inpainting, and field tracking. Novel PDE based models and corresponding numerical methods are introduced for each of these problems.

We proposed an original framework for segmentation that may incorporate various forms of prior information. This information can include shape, key points, or intensity profiles. We also proposed the level set formulation and a numerical algorithm for the model. We proposed a novel inpainting model and applied it to magnetic resonance imaging (MRI). This novel inpainting model considers the automatic choice of diffusion type. A specific modification of this model for sensitivity maps was produced. We also introduced a new framework (the modified Mumford-Shad model by level set) for tomography problems with extremely noisy and limited data. This algorithm is flexible, it can be used for any geometry with or without prior information. This model is very easy to modify for various cases. Finally, we proposed a novel tracking algorithm. The proposed method solves multi-diffusion-direction and branch problems existing in fiber tracking.

We applied those models on segmentation of ultrasound cardiac images, MRI brain images, noise tomography, inpainting of sensitivity maps for MRI surface coils, and fiber tracking. Experimental results and computational costs were compared with conventional methods.

CHAPTER 1 INTRODUCTION

Variational and partial differential equation (PDE) methods have been widely used in image processing in the past few years. Examples include continuous mathematical morphology, shape from shading, invariant shape analysis, image segmentation, tracking, image restoration, stereo, contrast enhancement, and inpainting. The basic idea is to represent an image as an R^2 function. This function usually satisfies a time dependent PDE that characterizes the giving problem. The solution of the differential equation gives the processed image at the scale t . A PDE can be obtained through direct derivation of the evolution equations such as the classical snakes model by Kass, Witkin and Terzopolous [1]; the anisotropic diffusion model by Perona and Malik [2]; and the image inpainting by Bertalmio et al. [3]. A PDE can also be obtained from variational problems. This is more common in image processing. The basic idea is to minimize an energy functional.

Using variational and PDE methods in image analysis leads to modeling images in a continuous domain. This simplifies the formalism, which become grid independent and isotropic. Conversely, when the image is represented as a continuous signal, PDEs can be seen as the iteration of local filters with an infinitesimal neighborhood. This interpretation of PDEs allows one to unify and classify a number of the known iterated fillters, as well as to derive new ones. Another important advantage of the variational and PDE approach is the possibility of achieving accuracy, stability and high speed with the help of the extensive results of numerical PDE methods.

This dissertation shows some applications of variational PDE methods for medical imaging. Chapter 1 presents the motivating applications for our research, reviews medical imaging concepts, and shows numerical techniques used to PDE models. This chapter also proposes the various conclusions and contributions of our study.

1.1 Motivating Applications

Partial differential equation based medical image processing has been applied in many fields. Several specific applications motivated our research. Those applications are segmentation of ultrasound cardiac image, Noise Tomography and calculation of sensitivity map of probe coil and fiber tracking.

1.1.1 Segmentation of Ultrasound Cardiac Image

The task of determining the epicardial and endocardial borders of the left ventricular (LV) on echocardiography images is essential for quantification of cardifunction. For ultrasound images, it is very difficult because of poor contrast, low signal to noise ratio, information dropout at the borders, and the inhomogeneity of intensities inside and outside the regions between epicardial and endocardial borders.

The aim here is to segment the endocardium and epicardium in a two-chamber or four chamber image of the heart. The endocardium and epicardium are not distinguishable in the image. Consequently, our task was to find and complete the boundary.

1.1.2 Noise Tomography

Noise Tomography, which aims to determine the distribution of the conductivity in the sample, is a new noninvasive medical imaging technique invented by MRI Devices Cooperation. The NT technique is designed to use the correlations in the detected electronic thermal noise in an RF probe array, and to use the relationship between

conductivity and the noise power coupled between the sample and probe to measure the electrical conductivity distribution within the sample. Many applications in diagnostic imaging have been documented: gastrointestinal and oesophageal function [4, 5], hyper- or hypothermic treatment of malignant tumors [6, 7], imaging of the head [8, 9], pulmonary function [10], cancer detection [11, 12], measurements of cardiac output [13], locating the focus of epileptic seizures [14], and so on.

Noise Tomography generates a three-dimensional map of the conductivity of the sample. Since it is based entirely on detection of the thermal noise generated within the body, NT is a completely noninvasive technique; and introduces no external power, chemicals, or radionuclides into the body.

However, because of the limitations of collection time and coil design, the data collected for image reconstruction are extremely noisy and limited. This leads to an ill-posed, big size inversion problem. The aim here is to create an efficient algorithm for tomography with extremely noisy and limited data.

1.1.3 Calibration of Sensitivity Map

A sensitivity map deals with the sensitivity information of RF probe coils in an MRI system it does not refer to the state of the object under examination. Knowledge of spatial receiver sensitivity implies information about the origin of detected MR signals, which can be used for image generation. Therefore, samples of distinct information content can be obtained at one time by using distinct probe coils in parallel implying the possibility of reducing scan time in Fourier imaging without having to travel faster in k -space. Parallel imaging techniques, which are based on the fact, have been widely applied since the 1990s of last century. Simultaneous Acquisition of Spatial Harmonics (SMASH [15]) and Sensitivity Encoding (SENSE [16]) are among the most famous

techniques. All of those techniques require highly accurate knowledge of component coil sensitivity information, which is the sensitivity map. Besides this application, the sensitivity map is also crucial to correct the inhomogeneity of surface coil MRI.

The raw sensitivity maps are impaired by noise. Straightforward elimination of noise by low-pass filtering results in errors at object edges. Hence denoising is required for raw maps. Some data sets with large areas (such as pulmonary MRA using fresh blood imaging) contribute little or no signal. In this case, there will be some holes, where we have no information of sensitivity at those places, in the sensitivity maps and therefore interpolation techniques are required to fix those holes. Furthermore, to deal with slightly varying tissue configurations and motion, extrapolation over a limited range is also necessary. The aim here is to create a technique to do denoising, interpolation, and extrapolation at the same time for the sensitivity map.

1.1.4 Intensity Correction

In the areas of medical imaging, acquired images may be corrupted by poor signal to noise ratio (SNR) or nonuniformities in spatial intensity. Poor SNR can cause blurred or ambiguous feature edges and nonuniformities in spatial intensity. Consequently, structures, textures, contrasts, and other image features may be difficult to visualize and compare both within single images and between a set of images. As a result, attending physicians or radiologists presented with the images may experience difficulties in interpreting the relevant structures. Nonuniformities can hinder visualization of the entire image at a given time and can also hinder automated image analysis. In MR images, the acquired images generally contain intensity variations resulting from the inhomogeneous sensitivity profiles of the surface coil or coils. In general, tissue next to the surface coil appears much brighter than tissue far from the coil. Spatial intensity variations introduced

by surface coil nonuniformity hinder visualization because one cannot find a window/level adjustment to encompass the entire field of view. When such images are filmed, the operator tries to select a setting which covers most of the features of interest. Furthermore, uncorrected image inhomogeneity makes it difficult to perform image segmentation and other aspects of image analysis. Therefore, techniques to enhance SNR and correct nonuniformity are necessary for MR images.

1.1.5 Fiber Tracking

Diffusion-weighted MRI (DWI) adds to conventional MRI the capability of measuring the random motion of water molecules, referred to as diffusion. Water in tissues containing a large number of fibers (such as cardiac muscle and brain white matter). The diffusion is fastest along the direction that a fiber is pointing to, but slowest in the direction perpendicular to it. Water diffuses isotropically in tissues that contain few fibers. DWI renders noninvasively such complex in vivo information about how water diffuses into an intricate 3D representation of tissues.

Conventional MRI can be used to investigate spatial relationships among different anatomical regions, but it is unable to infer the connectivity of these regions. DWI provides profound histological and anatomical information about tissue structure, composition, architecture, and organization. Changes in these tissue properties can often be correlated with processes that occur in development, degeneration, disease, and aging, so this method has become more and more widely applied [17-20].

Because DWI provides directional information concerning microscopic tissue fiber orientation at the voxel scale, fiber tracking (or fiber reconstruction) provides connection information between voxels based on the information from DWI.

1.2 Review of Conception

1.2.1 Description of General Tomography Problem

The goal of tomography is to reconstruct object profiles and extract object features given a set of tomographic measurements. In general, the problem of tomography is the problem of recovering (at least approximately) the values of a function from (possibly approximate and/or possibly weighted) an integral of the function over some subset of its domain. I.e. given the integral $M_i = \int_{\Omega} R_i(x)f(x)dx, i = 1,2,\dots,n$, and try to recover function $f(x)$ on the area Ω . In medical tomography problems, M_i is the collected data, and R_i is some fixed function determined by the character of the machine. Integral domain Ω can be different dimensions in different applications.

1.2.2 Mumford-Shah Model

The Mumford-Shah model was formulated by Mumford and Shah in 1989 [21], originally for an image segmentation problem. The segmentation problem can be defined as follows: Let $\Omega \subset R^N$ be the domain of a given observed image u_0 , Γ be the edges of u_0 , find a decomposition Ω_i of Ω and an optimal piecewise smooth approximation u of u_0 , such that u varies smoothly with each Ω_i , and rapidly or discontinuously across the boundary of Ω_i . Mumford and Shah proposed the following energy functional to solve it

$$E[u, \Gamma] = \int_{\Omega} (u - u_0)^2 dx dy + \mu \int_{\Omega \setminus \Gamma} |\nabla u|^2 dx + \nu |\Gamma| \quad (1-1)$$

where $\mu, \nu > 0$ are fixed parameters, to weight the different terms in the energy. The first term is called the fidelity term. It penalizes the difference between the smooth image and the original image. In the second term, $|\nabla u|$ is the L_2 norm of the gradient of u . This term

protects the smoothness of u outside the boundary Γ . In the last term, $|\Gamma|$ refers to the length of the boundaries in the image. For (u, Γ) a minimizer of the above energy, u is an “optimal” piecewise smooth approximation of the initial, possibly noisy, image u_0 , u will be smooth only outside Γ . Theoretical results of the existence and regularity of minimizers of this functional can be found in [21]. Later, Rudin, Osher and Fatemi [22] solved this problem by letting the power of $|\nabla u|$ be 1, which makes sure that the smooth is along the level set and therefore preserve and enhance edges.

1.2.3 Total Variation Denoising

Total Variation (TV) denoising method is a PDE-based technique that remove noise from images. This method was first introduced by Rubin, Osher and Fatemi [22]. The basic idea is to minimize the following functional:

$$\min_u \int_{\Omega} |\nabla u| dx dy + \frac{\lambda}{2} \int_{\Omega} (u - u_0)^2 dx dy \quad (1-2)$$

The TV functional does not penalize discontinuities in u and thus allows us to recover the edges of the original image.

The associated Euler-Lagrange equation of Equation 1-2 is

$$-\nabla \cdot \left(\frac{\nabla u}{|\nabla u|} \right) + \lambda(u - u_0) = 0 \quad (1-3)$$

Since $|\nabla u|$ is in the denominator, in order to avoid the singularity, it is common to use a slightly perturbed norm $|\nabla u|_{\alpha} = \sqrt{|\nabla u|^2 + \alpha}$, where α is a small positive constant, to replace $|\nabla u|$. This is equivalent to minimize the functional

$$\int_{\Omega} |\nabla u|_{\alpha} dx dy + \frac{\lambda}{2} \int_{\Omega} (u - u_0)^2 dx dy \quad (1-4)$$

Acor and Voger [23] showed that the solutions of the perturbed problems Equation 1-4 converge to the solution of Equation 1-2 when $\alpha \rightarrow 0$.

As an important improvement of TV functional, Strong and Chan [24] introduced the weighted TV functional

$$TV_{\alpha} = \int_{\Omega} \alpha(x) |\nabla u(x)| dx \quad (1-5)$$

for spatially adaptive (selective) image restoration. The function α is chosen so that α is larger away from possible edges and smaller near a likely edge. Hence we allow for greater smoothing away from edges and less smoothing at the edges. Certain choices of $\alpha(x)$ were given in [24] and [25]. Numerical results are very promising. Chen and Wunderli [26] prove that there exists a unique solution for the weighted TV functional.

Later, Chen and Levine improves the model [27]. They change the power of $|\nabla u|$ to be a function $P(x)$ which depends on $|\nabla u|$. This modification makes that one to control the type of diffusion at each location in the image. This model works better for piecewise smooth images and those in which the noise and the edges are extremely difficult to distinguish.

1.2.4 Level Set

Level set methods, introduced in 1988 by Osher and Sethian [28] are numerical techniques designed to track the evolution of interfaces. Rather than follow the interface itself, the level set approach takes the original curve (the red one on the left below), and builds it into a surface. That cone-shaped surface, which is shown in blue-green on the right below, has a great property; it intersects the xy plane *exactly* where the curve sits. The blue-green surface on the right below is called the level set function, because it

accepts any point in the plane as input and hands back its height as output. The red front is called the zero level set, because it is the collection of all points that are at height zero.

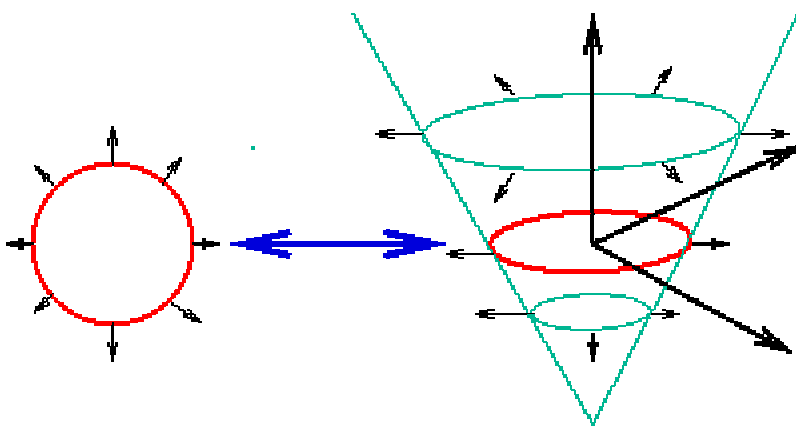


Figure 1-1. Level set

The idea of moving the front is that instead of moving the red front, which can do all sorts of weird things, one might try and instead move the surface on the right. In other words, the level set function expands, rises, falls, and does all the work. To find out where the front is, get out the saw and cut the surface at zero height.

The reason this is a good idea lies in taking a good look at the surface on the right. It will always be "nice"; the red front can get wildly contorted, but our blue level set function is well-behaved. All the complicated problems of breaking and merging are easily handled. Better yet, everything works for three dimensional surfaces with no change.

An equally important advantage is that it is easy to build accurate numerical schemes to approximate the equations of motion. That is because rather than track buoys around, which might end up colliding, one can instead stand on the xy plane and compute the answer. Using terminology from a completely different language, marker particle methods are man-to-man coverage, while level set methods are a zone defense. All

together, the trick of embedding the front in a higher dimensional function is well worth the added cost (in fact, with some work, that cost may be made the same as that of marker techniques).

A typical example of level set function is given by the signed distance function to the curve. In our case, level set is an effective implicit representation for Γ , because it allows for automatic change of topology, such as merging and breaking, and the calculations are made on a fixed rectangular grid. Hence, the level set method is applied here for numerical implementation.

1.2.5 Distance Function

Given a compact set K in space, the distance function for K at a point x is defined as the smallest Euclidean distance of x to the points in K . Fast and accurate computation of the distance function is an important step in many applications. For example, level set methods [28] rely heavily on the distance function to represent an interface, and in particular to keep the level set function well behaved during time evolution. In the surface interpolation model of Zhao et al. [29], a surface interpolating a given points set K is constructed by first computing the distance function to K . In the Island Dynamics model of Chen et al. [30] in materials science, one needs the distance function to help understand the aggregation of atoms into islands. Generally, applications in physics, chemistry, molecular biology, and even urban planning that use point pattern analysis require construction of the distance function. Furthermore, in applications such as ray tracing and surface rendering where one needs information about the normals or other geometric quantities of the surfaces of the given objects, the distance function is essential.

There are many different methods for finding distance function. The method chosen for our study is the closest point method [31]. To generate signed distance function, we need to know a point is inside or outside a curve. Tsai [31] introduces one method. One can also use the *Jordan curve theorem*: Run a semi-infinite ray vertically up from the test point, and count how many edges it crosses. At each crossing, the ray switches between inside and outside. This method is very fast and easy to implement.

1.2.6 Mutual Information

Mutual information [32-34], or simply information, was introduced by Shannon in his landmark 1948 paper "A Mathematical Theory of Communication." It is a measure of the statistical dependency between two random variables based on Shannon's entropy.

Let's first review some probability theorems. Given a sample space S , and events E and F in S , the probability of E is written $P(E)$ and the probability of F is written $P(F)$. The joint probability of E and F is the probability that both occur, $P(E \text{ and } F)$. The E and F are independent if and only if $P(E \text{ and } F) = P(E) \times P(F)$. The $P(E \text{ or } F) = P(E) + P(F) - P(E \text{ and } F)$. The conditional probability of E occurring, given that F has occurred, is $P(E | F) = P(E \text{ and } F) / P(F)$. Bayes Rule: If (E_1, \dots, E_n) are n mutually exclusive events whose union is the sample space S , and E is any arbitrary event of S with nonzero probability, then $P(E_k | E) = P(E_k)P(E | E_k) / P(E)$.

Given random N -vector X with density $p(x)$, the Shannon entropy is defined as $H(X) = -\int_{R^N} p(x) \log p(x) dx$. $H(X)$ is a measure of the uncertainty on the values X may assume. Let's now consider a second random variable Y with probability distribution

$p(y)$, then $H(X, Y) = -\int_{R^N} \int_{R^N} p(x, y) \log p(x, y) dx dy$ is the joint entropy of X and Y , and $p(x, y)$ is the joint density function. The $H(X, Y)$ is a measure of the uncertainty on the values X and Y may jointly assume. The $H(X, Y)$ is maximum if X and Y are statistically independent (completely uncoupled): in this case $H(X, Y) = H(X) + H(Y)$. The $H(X, Y)$ is minimum if X is a function of Y (deterministic coupling): in this case $H(X, Y) = H(X) = H(Y)$.

The definition of Mutual Information between X and Y naturally follows from the properties of $H(X, Y)$. Mutual Information MI is defined as

$MI(X, Y) = H(X) + H(Y) - H(X, Y)$. The MI is clearly a measure of the statistical coupling between X and Y . The lowest possible value of MI is 0, and this happens if and only if X and Y are independent (uncoupled). The highest possible value of MI is $MI(X, Y) = H(X) = H(Y)$, and this happens if and only if X is function of Y (deterministic coupling). An important property of MI is that it is invariant to any strictly monotonic transformation of X and Y .

1.2.7 Inpainting

The concept of digital inpainting was first introduced into the image processing community by Prof Sapiro's [3] group at the Department of electrical and computer engineering, University of Minnesota, as inspired by the manual inpainting process of real restoration artists and museum conservators. In nature, inpainting is an image interpolation and restoration problem. Based on the applications, there are numerical methods for inpainting, such as PDE base transportation inpainting [3], jointly continue/interpolate level-lines (geometry) and gray values (photometry) in a smooth

fashion [35], curvature driven diffusions (CDD), Bayesian framework for image restoration, total variation inpainting [36], elastica inpainting [37], Mumford-Shah-Euler inpainting [38], and so on.

1.3 Numerical Techniques

Some numerical techniques are introduced in this section. These numerical techniques are applied to all PDE models in chapters 2,3, and 4.

1.3.1 Choice of Heaviside Function

There are several ways to define the Heaviside function H_ε . According to Chan and Vese [39], the following definition is suggested

$$H_\varepsilon(z) = \frac{1}{2} \left(1 + \frac{2}{\pi} \arctan \left(\frac{z}{\varepsilon} \right) \right), \text{ and}$$

$$\delta_\varepsilon = H'_\varepsilon, \varepsilon \rightarrow 0 \text{ is defined as } \delta_\varepsilon(u) = \frac{1}{\pi} \bullet \frac{\varepsilon}{\varepsilon^2 + u^2}.$$

1.3.2 Computation of $\kappa = \text{div} \frac{\nabla u}{|\nabla u|}$

Since $|\nabla u|$ is in denominator, singularity may happen. To avoid singularity, several approaches can be applied. One way is to add a small positive constant in the denominator; however how to choose this constant is a problem. Another approach was introduced in Blomgren et al. [40]. The idea is to let

$$w = \frac{\nabla u}{|\nabla u|} \text{ and solve the system}$$

$$\begin{cases} w|\nabla u| = \nabla u \\ \kappa = \text{div}(w) \end{cases}$$

to avoid the singularity.

Chan and Vese [39] introduced the approach, which was used in our experiments.

The following “difference schemes” are applied

$$\begin{aligned} \operatorname{div}(\bar{u}) &= \frac{\Delta_-^x u_1 + \Delta_-^y u_2}{h}, \bar{u} = (u_1, u_2) \\ \nabla u_{ij}^n &= \frac{(\Delta_+^x u_{ij}^{n+1}, \Delta_+^y u_{ij}^{n+1})}{h} \\ \Delta_-^x u_{ij} &= u_{ij} - u_{i-1,j}, \Delta_+^x u_{ij} = u_{i+1,j} - u_{i,j}, \Delta_-^y u_{ij} = u_{ij} - u_{i,j-1}, \Delta_+^y u_{ij} = u_{i,j+1} - u_{i,j} \end{aligned}$$

then

$$\operatorname{div}\left(\frac{\nabla u}{|\nabla u|}\right) = \frac{1}{h^2} (C_1 u_{i+1,j} + C_2 u_{i-1,j} + C_3 u_{i,j+1} + C_4 u_{i,j-1} - (C_1 + C_2 + C_3 + C_4) u_{ij})$$

where h is the step length.

$$\begin{aligned} C_1 &= \frac{1}{a_{ij}}, \quad C_2 = \frac{1}{a_{i-1,j}}, \quad C_3 = \frac{1}{b_{ij}}, \quad C_4 = \frac{1}{b_{i,j-1}} \\ a_{ij} &= \left(\left(\frac{\Delta_+^x u_{ij}^n}{h} \right)^2 + \left(\frac{u_{i,j+1}^n - u_{i,j-1}^n}{2h} \right)^2 \right)^{\frac{1}{2}} \\ b_{ij} &= \left(\left(\frac{\Delta_+^y u_{ij}^n}{h} \right)^2 + \left(\frac{u_{i+1,j}^n - u_{i-1,j}^n}{2h} \right)^2 \right)^{\frac{1}{2}} \end{aligned}$$

1.3.3 Initial Signed Level Set and Reinitialization

Because the energy which is minimized is not convex and also there is no uniqueness for the minimizers, the algorithm may not converge to a global minimizer for a given initial condition. In general, for real images with complicated features, the initial conditions with small initial curves were suggested by Vese and Chan [41]. This is for the following two reasons: first it has the tendency to converge to a global minimizer; and second, the algorithm is much faster.

Closest point method by Tsai [31] was used to compute the initial signed level set ϕ . During the iteration, reinitialization for ϕ is necessary at each step, because we work

with the regularized function δ_ϵ . This procedure is standard [39, 42], and prevents the level set function from becoming too flat, or it can be seen as a rescaling.

1.3.4 Fast Sweep Method for Level Set Based Optimization

Recently, the fast algorithm for level set based optimization [43] was introduced by Bing Song. Applying this method to solve a class of optimization problems with level set representation can improve the computational speed dramatically. Because this method does not solve the Euler-Lagrange equation and only uses the sign of level set, the implementation is much simpler than the numerical method introduced above.

This algorithm is defined for $\min_{\phi} F(H(\phi))$ where H is the Heaviside function; F is any functional dependent on $H(\phi)$ and ϕ is the level set function. The outline of the algorithm is as follows:

Step 1: Initialize. Construct an initial partition (one part for $\phi > 0$, one part for $\phi < 0$) and compute the value of F according to ϕ .

Step 2: Advance. For each point x in image, if the energy F decreases when we change $\phi(x)$ to $-\phi(x)$, then update this point by $\phi(x) = -\phi(x)$; otherwise, $\phi(x)$ remains unchanged. We sweep the pixels in some prescribed order. For example, in image segmentation, we can sweep the pixels row by row. We can use either Gauss-Seidel or Jacobi iteration in each sweep.

Step 3: Repeat step 2 until the energy F remains unchanged.

Because there is no $\kappa = \text{div} \frac{\nabla u}{|\nabla u|}$ term and we do not need to reinitialize the level,

computation speed can be dramatically reduced.

1.4 Contributions of Our Study

1.4.1 Segmentation with Prior Information

Chapter 2 proposes a framework for segmentation that incorporates different prior information. The prior information could be shape, key points or, intensity profile. We also propose the level set formulation and a numerical algorithm for the model.

According to the available prior information, this model can easily be modified for the specific priors. Several examples for different prior information are given in the experiment section. The proposed model has five advantages. First, with the prior shape information, this model can reliably segment images in which the complete boundary was either missing, or was low resolution and low contrast. Second, besides segmentation, the algorithm also provides registration estimations of translation, rotation, and scale that maps the active contour to the prior shape. Third, with the help of key points, the problem (which is to determine local shape variations from the “average shape”) can be improved. Fourth, we used maximizing MIIG rather than MI to match intensity profiles of two images. We did this because that the MIIG takes neighborhood intensity distribution into account and hence gives better a description of the intensity profile than MI does. Fifth, the parameter in the model of active contour with shape can be selected by the model itself, and the segmentation with the optimized parameter arrives at higher image gradients, forms a shape similar to the prior, and captures the prior intensity profile. Experiments on synthetic and clinical images show those advantages.

1.4.2 Inpainting

A novel inpainting model was proposed and was applied to MRI. This work made the following contributions:

- Introduced the inpainting technique into the field of MRI

- Introduced a novel inpainting model that considers the automatic choice diffusion type
- Provided a fast and robust technique for calculation of a RF coil sensitivity map
- Provided a real-time and robust technique for simultaneous correction for nonuniformity and preservation for SNR.

All of the major issues involved in the correction of sensitivity maps were effectively and simultaneously dealt with: de-noising is accomplished, holes have been fixed, and the original map has been smoothly extended to the entire image. By the experiments with intensity correction maps, it can be concluded that, with the use of inpainted intensity correction maps, the inpainting method is capable of correcting nonuniformity while perfectly preserving SNRs.

1.4.3 Modified Mumford-Shah Model for Tomography

Chapter 4 introduces a novel framework MMSLS for the tomography problem with extremely noisy and limited data. This algorithm is flexible. It can be used for any geometry with or without prior information. It is very easy to change the model for different cases. Furthermore, this approach has no special requirements. Hence it may be easily applied to a variety of tomography problems.

The main contributions of this work include providing a solution for medical tomography problem with extremely noisy and limited data; introducing a model for tomography with guiding image; introducing a novel noninvasive technique for conductivity map, which can be used for cancer detection and much more.

The MMSLS algorithm has proven itself to provide accurate results. Because the MMSLS algorithm is object based, not pixel-based, this approach, for an equivalent output resolution, is much faster than conventional methods. Moreover, the reconstructed image, using MMSLS, is smooth, and the edge is perfectly preserved. The visualization

is therefore much better than when using other approaches. Another impressive advantage of this approach is that it can accomplish segmentation and reconstruction at the same time.

1.4.4 Fiber Tracking

A novel tracking algorithm is proposed. The proposed method solves multi-diffusion-direction, branches and tracking back problems existing in fiber tracking problems. There are three major differences between this work and other fast marching based methods. First, local polynomial fitting is used to define evolution speed. Second, the closest point method is applied to find the most reasonable path to connect two points. Third, the front propagation method is modified to deal with multi-diffusion-directions in some voxels. Hence this method is more efficient way to partially solve multi-fiber problem.

CHAPTER 2 SEGMENTATION WITH PRIOR INFORMATION

In this chapter, we propose a new variational framework for image segmentation that incorporates with prior information. Models are created for segmentation problems with several different kinds of prior information like the following: expected shape, expected shape and a few points on the boundary, expected shape and intensity profiles. This chapter is organized as follows. In the introduction section, the background of segmentation and review of existing segmentation methods are introduced. Then, in the method section, a PDE based segmentation model is proposed with numerical algorithms. In experiment and result section, we show experimental results of the application of the proposed method to synthetic images and cardiac ultrasound images and discussion of the proposed framework ends this chapter.

2.1 Introduction

2.1.1 Definition of Segmentation

Segmentation is the process of identifying regions of pixels in an image. The main goal is to divide an image into parts that have a strong correlation with objects or areas in the real world. We can use the gradient of the intensity (edges), or gray level similarities, or other features in the image to perform the segmentation.

2.1.2 Importance of Segmentation in Medical Applications

An example of the usefulness of this process is performing measurements of cardiac function (Figure. 2-1). The object for this image might be to determine the area of blood in the left ventricle.

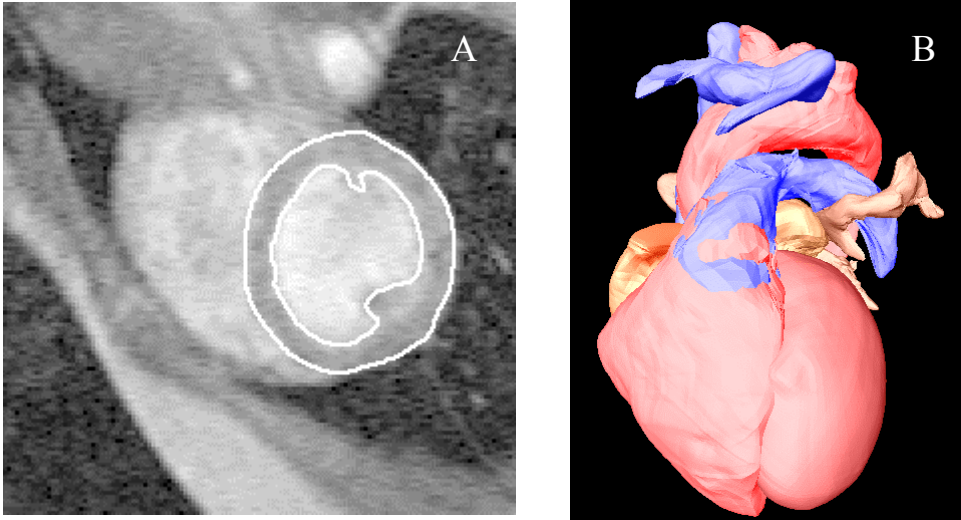


Figure 2-1. Examples of segmentation for cardiac images. A) a 2 dimensional example, B) a 3 dimensional example

The region is shown in the left of the above image. This region can be drawn by hand. If images are obtained throughout the cardiac cycle and over the entire left ventricle, then the amount of blood in the left ventricle can be determined at end systole (ES) and end diastole (ED) from which the percentage of blood that is ejected on one heart beat can be determined (ejection fraction). This is an important measurement to cardiologist but would require intensive interaction with a computer by an expert in order to determine the blood volume on a typical data set. These data sets usually contain over 200 images. You might expect that methods to automate this process are both desired and necessary. In addition to obtaining the stroke volume, if the outside wall of the myocardium, epicardium, can also be obtained, then the thickening of the left ventricular wall could also be obtained throughout the cardiac cycle. The differences in thickening over the left ventricular wall can show regions that are not functioning well due to decreased blood flow. Applications also include Multiple Sclerosis (MRI), MR Angiography, Brain Tumor (MRI) and Neuro Applications.

2.1.3 Review of Segmentation Methods

A large number of segmentation algorithms have been proposed. For the different applications and for the different image types, there are different types of method for segmentation.

According to the information used for segmentation, there are three classes of segmentation methods: global knowledge, edged-based and region-based. Global knowledge methods rely on knowing something about the image such as the expected pixel intensity. This is possible in CT where the intensity values are in Hounsfield units. Thus, one can look for all pixels of value near 808 for bone. Typically, threshold techniques are used for this process. Most of the methods based on global knowledge of the image are thresholding techniques. Thresholding techniques are effective when the intensity levels of the objects fall squarely outside the range of levels in the background. Because spatial information is ignored, however, blurred region boundaries can create havoc. Edge-based methods find the borders between regions. The edge-based methods [1, 44-48] rely on the information of the edges, such as high magnitude of image gradient. Edge-based methods center around contour detection and their weakness in connecting together broken contour lines make them, too, prone to failure in the presence of blurring. Region-based methods may be more applicable when edges are difficult to determine because of noise. The region-based methods [21, 39, 49-52] make use of homogeneity on the statistics of the regions being segmented. We can use many different properties of the image intensity to define regions such as gray level, color, texture and shape to name just a few. Hybrid techniques using a mix of the methods above are also popular.

In numerous medical imaging modalities, the boundaries of anatomical structures of interest may be very difficult to capture. The reasons for this difficulty includes low contrast, low resolution, or even that a portion of the object is not in the field of view. For example, in echocardiography the images are typically degraded by noise and signal drop out. In some cases, an image sequence may even have portions of the myocardium that lie outside of the sector scan so that some segments of an object boundary may not be visible at all. Thus, the segmentation problem for these images is very challenging and cannot be successfully segmented by above methods.

In an effort to overcome these difficulties, various techniques have been developed to incorporate prior information of an object's expected shape into the segmentation process. For example, Cootes, et al. [53] and Wang, et al. [54] constructed a statistical model of an object's shape from a set of corresponding points defined on a set of training images and then incorporated this information into a Bayesian formulation to find an object's boundary. Cootes, et al. [55] also used a Gaussian model to fit a training set of corresponding feature points. Later Cootes and Taylor used non-Gaussian mixture models to fit data for specific applications [56]. Staib and Duncan [57] specified the shape of the curve by creating statistical priors on the Fourier coefficients of the contour.

This prior was incorporated into a segmentation process by a posteriori technique. Yuille, Hallinan, and Cohen [58] and Tagare [59] used a deformable template approach to incorporate shape information into the segmentation process. Recently, statistical shape knowledge has been incorporated into edge based or region based active contours. Leventon, Grimson, and Faugaras [60] and Chen et al. [61] incorporated prior shape information into the geodesic active contour model. Chen et al. [62] used a principal

component analysis technique to build a statistical shape model from a training set of curves, where each curve is represented by a signed distance function. A force depending on the shape model was added at each iteration of the level-set surface evolution for the geodesic active contour to force the active contour towards high image gradients and a maximum posteriori estimate of shape and pose. In Tsai et al.[52] the shape model was obtained by averaging the aligned training samples. Their model finds the segmentation transformation which maps the evolving interface to the shape prior by minimizing an energy functional containing the energy of geometric active contour and a measure of the shape disparity between the active contour and the prior. The disparity is measured by using distance function. A number of research groups have incorporated a statistical shape model into a region-based segmentation scheme including Cremers, Schnorr, and Weickert [51], Tsai et al. [52], and Paragios and Rousson [63]. In the Cremers, Schnorr, and Weickert approach, an energy functional is minimized that includes both a “shape energy” term corresponding to the Gaussian probability as well as a Mumford-Shah [21] energy term. Tsai et al. build a parametric shape model similar to the one described by Leventon, Grimson, and Faugaras [60], where parameters are calculated to minimize a region based objective function which provides the segmentation. The shape model of Paragios and Rousson was formed using the level set representation and the variability of the shape. It was designed to maximize the log-likelihood function, which is represented by a Gaussian density function where the mean corresponds to the level set representation of the shape and the variance refers to the variation of the aligned samples. Then, the shape model was combined into a geodesic active region model [64] in a variation framework. Leventon, Faugaras, Grimson, and Weickert used a training set to extract

prior information of the intensity and curvature profiles of the features. This information was incorporated into the segmentation processing by using an approach similar to the one developed in Leventon et al. [60].

2.1.4 Remaining Problems in Existing Methods

While experimental results have shown the effectiveness of prior-based models in numerous medical applications, many problems remain including the complexity and variability of the images, the accuracy of the measurements obtained, and the rapid computation time required by the user. One practical problem is how to determine the parameter that balances the influences from image information and priors. If the evolution of an active contour is mainly governed by the force depending on the image gradient, it may be sensitive to the initial step or may leak through the boundary where the edge feature is not clearly defined. Conversely, if the force depending on the shape prior is the dominating term, the active contour may not arrive at the boundary of the object of interest even though it has a shape similar to the prior.

2.2 Method

In this section, a general variational framework for segmentation with prior information is proposed in 2.2.2. The method for generation of required prior information is explained in 2.2.1.

2.2.1 Generation of Prior Information

As we mentioned above, the segmentation problem could be very difficult. Therefore some prior information may be necessary. In this section, the methods for generation of prior information based on training set are discussed.

2.2.1.1 Shape analysis

To get the prior shape information, an average shape needs to be purified from a set of training shapes. A modified procrustes method is applied here to cluster shapes into groups, and each group generate an average shape.

The study of Procrustes shape analysis was provided a solid mathematical foundation in the seminal work of D. Kendall [65], where the contours are considered to be vectors in a high dimensional complex projective space. A comprehensive introduction to the topic can be found in the text by C. Small [66]. When the heart is imaged from the parasternal short-axis view, it has a simple geometric shape that can be reasonably modeled by a continuous contour written as the union of 4 elliptical arcs [67]. So Procrustes shape analysis can be used in echocardiographic images analysis.

The shape of an object is defined in a mathematical context as all the geometrical information that remains after location, scale and rotational effects are filtered out; i.e. an object's shape is invariant under the Euclidean similarity transformations of translation, scaling and rotation. For analysis purposes shape is described by a finite number of points on each object's surface, which are called landmarks.

Given two shapes A,B. The first step is to define landmarks of those two shapes. In order to apply procrustes, the center of the parameterized contours are the origin. And those two contours have same number of points, all the angles that between radials connecting origin and the point are same.

In standard procrustes, the distance between two contours A,B are defined as Frobenius norm of A-B, and when try to minimize the distance by processes of rotation , scaling and translation, each step is processed separately.

In this modified procrustes, the distance is defined as the area difference and rotation, scaling and translation are processed at the same time. The following definitions and theorems are for 2 dimensional case.

Definition 1 . Let A, B be two contours, then the area between those two contours are defined as

$$a(\mathbf{A}, \mathbf{B}) = \text{the area of } (\mathbf{A} \cup \mathbf{B} - \mathbf{A} \cap \mathbf{B}). \quad (2-1)$$

Definition 2. The shape distance between two contours A_1, A_2 is defined as the minimum Area between two contours after rotation, transfer and scaling.

$$AD(A_1, A_2) = \min_{\mu, R, T} (a(\mu R A_1 + T, A_2)) \quad (2-2)$$

Where μ is the scalar parameter, R is the rotation matrix, T is the transfer vector. μ and

R can be combined into one matrix $\begin{pmatrix} a & -b \\ b & a \end{pmatrix}$. Let $T = \begin{pmatrix} t_1 \\ t_2 \end{pmatrix}$, then there are 4 unknowns

to get the shape distance. Theorem 1 shows how to solve those 4 unknowns.

Theorem 1. Let $A = (a_{ij})_{n \times 2}$, $B = (b_{ij})_{n \times 2}$, $c_i = (b_{i+1,2} - b_{i,2})^2 + (b_{i+1,1} - b_{i,1})^2$ then

$\min_{R, T} (\text{area}(R * A + T, B))$ achieves at

$$R = \begin{pmatrix} a & -b \\ b & a \end{pmatrix}, T = \begin{pmatrix} t_1 \\ t_2 \end{pmatrix}, \text{ When}$$

$$\begin{pmatrix} \sum_{i=1}^n c_i (a_{i1}^2 + a_{i2}^2) & 0 & \sum_{i=1}^n c_i a_{i1} & \sum_{i=1}^n c_i a_{i2} \\ 0 & \sum_{i=1}^n c_i (a_{i1}^2 + a_{i2}^2) & -\sum_{i=1}^n c_i a_{i2} & \sum_{i=1}^n c_i a_{i1} \\ \sum_{i=1}^n c_i a_{i1} & -\sum_{i=1}^n c_i a_{i2} & \sum_{i=1}^n c_i & 0 \\ \sum_{i=1}^n c_i a_{i2} & \sum_{i=1}^n c_i a_{i1} & 0 & \sum_{i=1}^n c_i \end{pmatrix} * \begin{pmatrix} a \\ b \\ t_1 \\ t_2 \end{pmatrix} = \begin{pmatrix} \sum_{i=1}^n c_i (b_{i1} a_{i1} + b_{i2} a_{i2}) \\ \sum_{i=1}^n c_i (b_{i2} a_{i1} - b_{i1} a_{i2}) \\ \sum_{i=1}^n c_i b_{i1} \\ \sum_{i=1}^n c_i b_{i2} \end{pmatrix} \quad (2-3)$$

In the proof of this theorem, $area(R * A + T, B)$ was approximated by

$$\sum_{i=1}^n c_i ((aq_1 - bq_2 + t_1 - b_{i1})^2 + (bq_1 + aq_2 + t_2 - b_{i2})^2)$$

Given a set of parameterized shapes, a basis is randomly chosen from those shapes. Applying Equation 2-3 to minimize the distances between the basis and all other shapes by rotation, translation and scaling. Then the average shape is the equally weighted summation of those calibrated shapes. This definition of average curve is simple but not accurate. A better way is to apply distance function here to find the curve, which minimize the summation of distances between the curve and all other curves.

The clustering method is named as “*near basis method*”. Given a set of shapes, randomly choose one as the basis of first group, minimize the shape distance between this basis and all other shapes by applying Equation 2-3. All the shapes that have distance less than a certain threshold will be set in the same group as the basis. The threshold hold can be set as a value ε (<1) multiply the mean of all distances. Then randomly choose one shape from the given shapes that are not in the first group as the basis for the second group. Repeat until all shapes are in some group.

Now there are several groups. Compute the average of all of those groups. Then we try to reset the groups according to the averages. Minimize the distance between each contour and each average. A matrix, which has size number of contours multiply by number of groups, is generated. Each curve is reset in the group that has nearest average to it. Repeat group resetting until convergence is approached. Here is no proof for this convergence, but experimentally it converges very quickly.

An alternative method we used to create the prior shapes was “*the self-organizing maps*” algorithm. If we want to group the n training contours $C_i, i = 1, \dots, n$ into k

clusters (say $k = 3$), we first take three arbitrary contours as the initial contours, denoted by $m_j(0)$ ($j = 1, 2, 3$). At $t + 1$ iteration, randomly select a contour denoted by $X(t + 1)$ from the training set, and compare the disparity in shape between $X(t + 1)$ and each of $m_j(t)$ ($j = 1, 2, 3$). To do this comparison we first align $X(t + 1)$ to each $m_j(t)$ and denote the aligned $X(t + 1)$ by $\tilde{X}_j(t + 1) = \mu_j R_j X(t + 1) + T_j$. Then we compute

$A_j \equiv a(\tilde{X}_j(t + 1), m_j)$ defined in (2.1). Suppose A_1 is the smallest number in A_j , $j = 1, 2, 3$.

We keep $m_2(t)$ and $m_3(t)$ unchanged, and update $m_1(t)$ by

$m_1(t + 1) = m_1(t) + \alpha(t)[\tilde{X}_1(t + 1) - m_1(t)]$, where $\alpha(t)$ is a smooth function of t , and

decreases to zero as $t \rightarrow \infty$. After a large number, say N , of iterations, three *average*

shapes $m_j(N)$ ($j = 1, 2, 3$) are generated. Then three clusters are formed by the curves that are closest to the *average* shapes. The closeness is again measured by the measurement in (2.1).

2.2.1.2 Intensity profile

In this section we introduce our method for generating an intensity model (average intensity profile across the average shape) from a set of training images.

Let $C_i(p)$, $i = 1, \dots, m$ be a set of training segmentations in one cluster, and

I_i , $i = 1, \dots, m$ be the set of images associated with $C_i(p)$. Let also $C^*(p)$, $p \in [0, 1]$ be the *average* shape in the cluster. Our task is to generate an average intensity profile I^* across C^* from the training images I_i . If I^* is created just by averaging all the sample images

I_i , $i = 1, \dots, m$, I^* can be blurred, due to the large intensity variations in the training

images. To reduce the influence from the outliers we select a subgroup from

$I_i, i = 1, \dots, m$, in which the disparity in intensity profiles are relatively small. To do this, we first align each contour $C_i(p), i = 1, \dots, m$ to C^* by a similarity transformation (μ_i, R_i, T_i) that minimizes $a(C^*, C_i)$ defined in section (2.1).

Next, we examine the disparity in the training intensity profiles across the training segmentation as follows. Let

$$V_{\varepsilon_0} = \{x \in \Omega \mid d(C^*, x) < \varepsilon_0\} \quad (2-4)$$

be a ε_0 neighborhood of C^* . If two images I_i and I_j are related approximated by

$$I_i(\mu_i^{-1} R_i^{-1}(x - T_i)) \approx a I_j(\mu_j^{-1} R_j^{-1}(x - T_j)) + b \quad (2-5)$$

for some constants a and b , we may define the closeness/disparity measurement in the intensity profiles near the segmentation C_i and C_j by

$$\int_{V_{\varepsilon_0}} |I_i(\mu_i^{-1} R_i^{-1}(x - T_i)) - a I_j(\mu_j^{-1} R_j^{-1}(x - T_j)) - b|^2 dx.$$

The integral is over V_{ε_0} rather than the entire image domain, since the intensity profiles near the segmentations are more meaningful. If the relation (2-5) is not valid, maximizing mutual information has been proven to be effective in solving matching problems, in particular in matching multi-modality images [33, 34, 68, 69]. One of the advantages of using mutual information is that it does not require an explicit function that relates two images, but only assumes that aligned images explain each other better than when they are not aligned.

The mutual information between two random vectors X and Y is defined as

$$MI(X, Y) = H(X) + H(Y) - H(X, Y) \quad (2-6)$$

where

$$H(Z) = -\int_{R^N} p(z) \log p(z) dz \quad (2-7)$$

is the Shannon entropy of a random N-vector Z with density $p(z)$, and

$$H(X, Y) = -\int_{R^N} \int_{R^N} p(x, y) \log p(x, y) dx dy \quad (2-8)$$

is the joint entropy of X and Y , and $p(x, y)$ is the joint density function. Consider intensity at each voxel as the realization of a random variable, and all the random variables in an image have the same distribution. By using (2-6)-(2-8), the common mutual information (MI) of two images I_i and I_j on a region V_{ε_0} can be computed by

$$MI_{V_{\varepsilon_0}}(I_i, I_j) = -\int_{R^2} p(f, g)(i_1, i_2) \log \frac{p(f, g)(i_1, i_2)}{p(f)(i_1)p(g)(i_2)} di_1 di_2 \quad (2-9)$$

where

$$f(x) = I_i(\mu_i^{-1} R_i^{-1}(x - T_i)), \quad g(x) = I_j(\mu_j^{-1} R_j^{-1}(x - T_j)) \quad (2-10)$$

$p(f, g)$, $p(f)$ and $p(g)$ are computed over V_{ε_0} .

Note that if the locations of two points in an image are switched, then the intensity profile is changed, but the density function remains the same. In order to match intensity profiles of two images, we propose to maximize the mutual information of image geometry (MIIG) rather than mutual information (MI).

By MIIG of I_i and I_j on V_{ε_0} , we mean that

$$MIIG_{V_{\varepsilon_0}}(I_i, I_j) = \int_{R^{10}} p(F(x), G(x))(m, n) \log \frac{p(F(x), G(x))(m, n)}{p(F(x))(m)p(G(x))(n)} dmdn \quad (2.11)$$

where

$$F(x) = \langle f(x-2h), f(x-h), f(x), f(x+h), f(x+2h) \rangle,$$

$$G(x) = \langle g(x-2h), g(x-h), g(x), g(x+h), g(x+2h) \rangle,$$

with f and g are defined in (2.10), $m = \langle i_1, i_2, i_3, i_4, i_5 \rangle$, $n = \langle i_6, i_7, i_8, i_9, i_{10} \rangle$,

$dm = di_1 di_2 di_3 di_4 di_5$, and $dn = di_6 di_7 di_8 di_9 di_{10}$. Since MIIG uses neighborhood

information, MIIG of two images gives better description of the closeness of the intensity profiles of these two images than MI.

We now describe the construction of the *average* intensity profile I^* across C^* .

Ideally, we would like to generate I^* by

$$\max_{I^*} \sum_{j=1}^{11} MIIG_{V_{e_0}}(I^*, I_j) \quad (2-12)$$

where $MIIG_{V_{e_0}}(I^*, I_j)$ is defined as in (2.11) with $f = I^*(x)$ and $g = I_j(\mu_j^{-1} R_j^{-1}(x - T_j))$.

Since this formulation is computationally intensive, we restricted ourselves to the cases

where

$$I^* = \sum_{j=1}^{11} a_j I_j(\mu_j^{-1} R_j^{-1}(x - T_j)) \quad (2-13)$$

The weights a_j were determined by using Equation 2-12.

2.2.2 Framework Description

To get a desirable segmentation in these cases, prior information of shape, intensity and key points besides the image itself can be applied in this framework. There are 4 terms in the proposed variational framework. Gradient term, shape term, key points term and intensity term. Several notations are defined for the following sections.

I : The image which is to be segmented

I^* : The average image generated according to Equation 2-13

Ω : The image domain of I

C : The segmentation in I , which is the unknown.

C^* : The average curve generated according to section (2.2.1.1)

u : A Lipschitz function level set such that C is the zero level set and $\{x|u(x) > 0\}$ is the set inside C .

$H(z)$: the Heaviside function, that is $H(z) = 1$ if $z \geq 0$, and $H(z) = 0$ if $z < 0$, and $\delta = H'(z)$ (in the sense of distribution) be the Dirac measure.

2.2.2.1 Gradient term

Gradient term is general in geometric active contours methods that are widely used for segmentation, that is, for finding object boundaries in images. Geometric active contours are using initialized curves, which dynamically evolve in the image to minimize their energy (or length in some conformal metric). Their energy is designed in such a way that its minimum occurs when the trace of the curve is over points of high gradient in the image. Because such points often define object boundaries, the active contour becomes stationary at the boundary.

Let $C(p)(p \in [0,1])$ be a parameterized curve with a regular parameter p . To regard the curve C as an active contour, we associate energy $E(C)$ with it:

$$E(C) = \int_0^1 g(|\nabla I|)(C(p))|C'(p)|dp \quad (2-14)$$

where $g(|\nabla I|)$ can be chosen as

$$g(|\nabla I|) = \frac{1}{1 + \beta|\nabla G_\sigma * I|^2} \quad (2-15)$$

where β is a parameter, and $G_\sigma(x) = \frac{1}{\sigma} e^{-\frac{|x|}{4\sigma^2}}$, so that $g(|\nabla I|)$ is strictly positive in

homogeneous regions and near zero on the edges [1, 46, 47]. Level set methods are

extensively used in active contour evolution because they allow the curve to develop cusps, corners, and topological changes. Notice that the length of the zero level set of u in the conformal metric $ds = g|C'(p)|dp$ can be computed by $\int_{\Omega} g|\nabla H(u)| = \int_{\Omega} \delta(u)g|\nabla u|$.

Hence the Gradient term in level set form is

$$E(u) = \int_{\Omega} \delta(u)g(|\nabla I|)|\nabla u| \quad (2-16)$$

The geometric active contour evolves to minimize this energy and stops when its trace is over points of high gradient. In many images, object boundaries cannot be detected by seeking pixels of high image gradient. Region-based methods that make use of homogeneity of the statistics of the local features and properties have been developed for such images. Mumford and Shah [21] proposed a variational framework for segmenting an image into homogeneous regions. Zhu and Yuille [49] proposed the region competition algorithm. Their algorithm combines the attractive geometrical features of snake/balloon models and statistical technique of region growing, and was derived by minimizing a generalized Bayes/MDL criterion using the variational principle. The region-based methods proposed in [39, 50, 51, 70] are an active contour based on minimizing the Mumford-Shah functional [21]. Recently, the Geodesic Active Region models [64, 71, 72] were proposed. These models combine boundary and region-based segmentation models. The evolution of the active contour is influenced by a region force that optimizes the segmentation according to the expected intensity of different regions, and a boundary force that contains information regarding the boundaries between the different regions.

2.2.2.2 Shape term

There is a serious practical problem with active contours – they do not become stationary at a boundary if the boundary has segments, which have low gradient. A geometric active contour will often “leak” through such “gaps” in the boundary. The problem is that the standard geometric active contours do not have any information about how the gaps are to be bridged. One solution to the problem is to incorporate into the active contour with some prior information about the expected overall shape of the boundary. Then the active contour can compare its shape with the expected shape and bridge the gaps in a meaningful way.

A statistical model of shape variation was constructed from a set of corresponding points across the training images [53] [54]. This information was used in a Bayesian formulation to find the object boundary. In [73] a Gaussian model was fit to a training set of corresponding feature points. In [56] mixed models were used to fit to the data for specific applications where the distributions are non-Gaussian. In an alternate approach in [57], Staib and Duncan specified the shape of the curve by creating statistical priors on the Fourier coefficients of the contour. This prior was incorporated into segmentation processing by a posteriori technique.

In this work, we propose a shape term for incorporating prior shape knowledge in the active contour. We modify the energy function of the contour so that the propagation velocity of the active contour depends on the image gradient as well as the prior shape. The velocity is designed such that the propagation stops when the active contour arrives at high gradients and forms a shape similar to the shape prior. The shape prior is obtained by a modified procrustes method (Section 3.2.2). The modified energy function gives a satisfactory segmentation in the presence of gaps, even when the gaps are a substantial

fraction of the overall boundary. We specify the entire prior shape, because a priori, we do not know where the low contrast gaps will occur in the boundary.

Our model differs from the model in [60] because we use a variational approach instead of a probability approach. That makes it possible to discuss the existence of the model solution in BV (bounded variation) space.

To begin the mathematical description, we first specify when two curves have the same shape. Two curves C_1 and C_2 have the same shape, if there exist a scale μ , a rotation matrix R (rotation by an angle θ), and a translation vector T such that C_1 coincides with $C_2^{new} = \mu RC_2 + T$. Let C^* be a curve, called the *shape prior*, representing the shape we expect of the boundary, and let $g(|\nabla I|)$ be the function defined in Equation 2-15. To capture the shape prior C^* , we would like to find a curve C and the transformation μ, R, T , such that the curve $C^{new} = \mu RC + T$ and C^* are closely aligned.

Therefore, to measure the closeness of C to C^* we introduce the shape energy term

$$E(C, \mu, R, T) = \int_0^1 d^2(\mu RC(p) + T) |C'(p)| dp \quad (2-17)$$

where $d(x, y) = d(C^*, (x, y))$ is the distance of the point (x, y) from C^* . In the numerical computation, this distance function is obtained by the fast marching method proposed by Sethian[74]. In level set form, we need measure the similarity of the shapes between the zero level set of u and C^* , which can be evaluated by $\int_{\Omega} \delta(u) d^2(\mu Rx + T) dx$. Since $d^2 |C'(p)| dp$ can be computed by $\int_{\Omega} d^2 |\nabla H(u)| = \int_{\Omega} \delta(u) d^2 |\nabla u|$, we have the shape term in level set form

$$E(u, \mu, R, T) = \int_{\Omega} \delta(u) d^2(\mu Rx + T) |\nabla u| \quad (2-18)$$

2.2.2.3 Key points term

The experimental results have shown that gradient term with shape term provide very promising results in various applications. However, due to the accuracy and efficiency requirement of medical image analysis problems, and the complexity of the medical image, as well as the variability of the anatomic shapes of interest in medical images, how to use shape prior in getting a better segmentation is still a challenging problem. One of the most difficult problems is to determine local shape variations from the “average shape.” One solution may be using non-rigid registration to assist segmentation [75, 76], but this requires better region or edge information in the image to find the velocity field, and also computationally costs. The aim of key points term is to find a better way to locate boundaries of interest, that has significant signal loss and relatively larger shape variation from the shape prior.

In particular, Cardiac ultrasound images exhibit signal drop out so that some segments of the boundary of the myocardium may not be visible in the image. Also ultrasound images often have a limited imaging range and the boundaries are not completely imaged. Moreover, the shapes of the boundaries vary from “average shape,” that can be constructed from a set of training shape. In particular, in abnormal heart image, the shape distortion of the myocardium from the “average shape” can’t be ignored. However, several points the boundary pass through can easily be given by experts.

Therefore we extend the segmentation algorithm developed in Chen et al. [62] by incorporating a few “key” points on the boundary of interest in addition to shape prior into geometric active contours. We will use the idea of matching nonequivalent shapes by the combination of a rigid transformation and a point-wise local deformation [63, 77] in

our modeling. Soatto and Yezzi [77] view a general deformation as the composition of a finite dimensional group action (e.g. rigid or affine transformation) and a local deformation, and introduced a notion of “shape average” as the entity that separates a group action from deformation. Paragios, Rousson and Ramesh [63] proposed a variational framework for global as well as local shape registration. Their optimization criterion accounts for global (rigid, affine) transformation and local pixel-wise deformation. Similar idea was also used in Leventon et al. [78] in defining shape prior models in the level set representations. These ideas can be used to simultaneous approximation and registration of nonequivalent shapes, and tracking moving and deforming objects through time. However, the question of how to determine the local deformation has not been involved in these works.

We will employ these ideas in our algorithm by viewing the evolution of active contour as a deformation of the interface, This deformation consists of a rigid transformation and a local deformation. We will use the “average shape” to determine the rigid transformation that better maps the interface to the prior shape, and use the image gradient and a few “key” points to determining the local deformation that provides more accurate segmentation.

Based on these thought, the proposed variational framework includes a key points term that is able to incorporate a priori knowledge on expected shape and a few points that boundary should pass through into active contours. We modify the energy function of geodesic active contour so that it depends on the image gradient and prior shape, as well as a few prior points. We only need a few points since we have information on expected shape. The modified energy function gives a satisfactory segmentation in the

presence of relatively large shape distortion, and gaps that are a substantial fraction of the overall boundary. To combine both prior shape (a global constrain) and prior points (a local constrain) into a single variational framework, we use level set formulation.

Suppose, x_1, \dots, x_m are prior points (given by experts) the boundary passing through. Then the level set $u(x_i) = 0$, for $i = 1, \dots, m$. Now let $f_\gamma(x)$ be a smooth function defined on the image domain Ω , such that $0 \leq f_\gamma(x) \leq 1$, $f_\gamma(x) = 1$ for $x = x_i, i = 1, \dots, m$. The function $f_\gamma(x)$ can be obtained by convolution of f and η_γ , where f is a function taking value one on the points x_1, \dots, x_m and zero elsewhere, and η_γ is the standard mollifier.

Now we can define key points term to be

$$E(u) = \frac{1}{2} \int_{\Omega} f_\gamma(x) u^2(x) dx \quad (2-19)$$

This term forces the interface passing through the given points since minimizing it with sufficiently small γ results that u must be close to zero at those points. Note that $f_\gamma(x)$ is non-zero only on the γ neighborhood of the given points, so the Key Points term doesn't affect much the shape of the contour outside the γ neighborhood of the given points.

2.2.2.4 Intensity profile term

Besides using shape prior, Leventon et al. [78] incorporated intensity and curvature priors to segmentation process by an approach similar to the one developed in Leventon et al. [60]. There are two reasons to have intensity profile terms. First, the model with intensity profile terms indeed performs segmentation and registration simultaneously. The registration in the model combines both a rigid transformation and a local

deformation. The rigid motion is determined explicitly by shape matching, while the local deformation is determined implicitly by the image gradient and prior intensity profile.

Another reason to use prior intensity profiles to assist segmentation is that in some cases information of only the expected shape may not be sufficient to guide the active contour to the boundary of the object of interest. For instance, in some 2-chamber cardiac ultrasound images, the image intensities of the myocardium are non-uniform, a significant portion of the border appears at low contrast, and their shapes are not similar to the prior. For this class of images a model incorporating only prior shape in the active contours may not be able to give an accurate segmentation.

In this section, we present an alternative method for generating average intensity profiles from a set of training images. To generate an intensity model in a Gaussian model was used to compute the joint distribution of the intensity values and signed distances to the boundary from a set of segmented training images. In ultrasound images signal is partially in the form of speckle. Since the statistics of speckle are non-Gaussian modeling the randomness of ultrasound images using a Gaussian model is not appropriate. Our method of generating an intensity model is model free and based on maximizing mutual information of image geometry between the intensity model and aligned training images in section (2.2.1.2).

By the reasons discussed in the previous section (2.2.1.2), we propose to use the MIIG of the prior image I^* and aligned novel image I in a neighborhood of C^* as the measurement of the disparity in intensity profiles across the interface and prior shape. Hence we define the intensity profile term to be

$$E_{\mu,R,T} = -MIIG_{V_{\varepsilon_0}}(I^*(x), I(\mu^{-1}R^{-1}(x-T))) \quad (2-20)$$

V_{ε_0} is defined in section (2.4). Notice that MIIG is always positive; we use negative sign to minimize the energy.

2.2.2.5 Proposed model and Euler-Lagrange equations

Consider gradient (Equation 2-16), prior shape (Equation 2-18), key points (Equation 2-19) and intensity profile (Equation 2-20) terms together, we have the following model for segmentation with prior information in level set form.

$$\begin{aligned} \min_{\lambda_1, \lambda_2, \lambda_3, \mu, R, T, u} \int_{\Omega} \delta(u) g(|\nabla I|) |\nabla u| + \frac{\lambda_1}{2} \int_{\Omega} \delta(u) d^2(C^*, \mu R x + T) |\nabla u| + \\ \frac{\lambda_2}{2} \int_{\Omega} f_{\gamma}(x) u^2(x) dx - \lambda_3 MIIG_{V_{\varepsilon_0}}(I^*(x), I(\mu^{-1} R^{-1}(x - T))) \end{aligned} \quad (2-21)$$

$\lambda_i > 0 (i = 1, 2, 3)$ are parameters balancing the influences from the image gradient, prior shape, key points and intensity profile. The active contour governed by Equation 2-21 is forced to arrive at high gradient, form a shape similar to the prior, across the key points and capture the prior intensity profile near the feature.

Let

$$\begin{aligned} f(x) &= G_{\sigma} * I^*(x) \\ g(x) &= (G_{\sigma} * I)(\mu^{-1} R^{-1}(x - T)) \\ p(f, g)(i_1, i_2) &= \frac{1}{|\Omega|} \int_{\Omega} G_{\beta}(f - i_1, g - i_2) dx \end{aligned}$$

where $G_{\beta}(x, y) = \frac{1}{\sqrt{2\pi}\sigma} e^{-\frac{x^2+y^2}{2\sigma^2}}$ (According to [69]), then

$$\begin{aligned} p(f)(i_1) &= \int_R p(f, g)(i_1, i_2) di_2 \\ p(f)(i_2) &= \int_R p(f, g)(i_1, i_2) di_1 \\ \frac{\partial p(f, g)(i_1, i_2)}{\partial u} &= \frac{1}{|\Omega|} \int_{\Omega} \partial_2 G_{\beta}(f - i_1, g - i_2) \nabla g(x) \cdot R^{-1}(x - T) \mu^{-2} dx \end{aligned} \quad (2.22)$$

$$\frac{\partial p(f, g)(i_1, i_2)}{\partial \theta} = \frac{1}{|\Omega|} \int_{\Omega} \partial_2 G_{\beta}(f - i_1, g - i_2) \nabla g(x) \cdot \frac{\partial R^{-1}}{\partial \theta}(x - T) \mu^{-1} dx \quad (2.23)$$

$$\frac{\partial p(f, g)(i_1, i_2)}{\partial T} = -\frac{1}{|\Omega|} \int_{\Omega} \partial_2 G_{\beta}(f - i_1, g - i_2) \nabla g(x) \cdot \mu^{-1} R^{-1} dx \quad (2.24)$$

Let $\Omega = V_{\varepsilon_0}$, and notice

$$MI(f, g) = -\int_{R^2} p(f, g)(i_1, i_2) \log \frac{p(f, g)(i_1, i_2)}{p(f)(i_1)p(g)(i_2)} di_1 di_2$$

then

$$\begin{aligned} \frac{\partial MI(f, g)}{\partial \mu} &= -\int_{R^2} \frac{\partial p(f, g)(i_1, i_2)}{\partial \mu} \log \frac{p(f, g)(i_1, i_2)}{p(f)(i_1)p(g)(i_2)} di_1 di_2 - \\ &\int_{R^2} p(f, g) \frac{p(f)p(g)}{p(f, g)} \cdot \frac{p_{\mu}(f, g)p(f)p(g) - p(f, g)p(f) \frac{\partial p(g)}{\partial \mu}}{p(f)^2 p(g)^2} di_1 di_2 \end{aligned}$$

Notice $\int_{R^2} p(f, g) di_1 di_2 \equiv 1$, we have

$$\begin{aligned} &\int_{R^2} p(f, g) \frac{p(f)p(g)}{p(f, g)} \cdot \frac{p_{\mu}(f, g)p(f)p(g) - p(f, g)p(f) \frac{\partial p(g)}{\partial \mu}}{p(f)^2 p(g)^2} di_1 di_2 \\ &= \int_{R^2} \left(\frac{\partial p(f, g)}{\partial \mu} - \frac{p(f, g)}{p(g)} \cdot \frac{\partial p(g)}{\partial \mu} \right) di_1 di_2 = 0 \end{aligned}$$

then by Equation 2.22

$$\begin{aligned} \frac{\partial MI(f, g)}{\partial \mu} &= -\int_{R^2} \frac{\partial p(f, g)(i_1, i_2)}{\partial \mu} \log \frac{p(f, g)(i_1, i_2)}{p(f)(i_1)p(g)(i_2)} di_1 di_2 \\ &= -\frac{1}{|\Omega|} \int_{\Omega} \int_{R^2} \partial_2 G_{\beta}(f - i_1, g - i_2) \nabla g \cdot R^{-1}(x - T) \mu^{-2} \log \frac{p(f, g)(i_1, i_2)}{p(f)(i_1)p(g)(i_2)} di_1 di_2 dx \end{aligned}$$

Similarly

$$\frac{\partial MI(f, g)}{\partial \theta} = -\frac{1}{|\Omega|} \int_{\Omega} \int_{R^2} \partial_2 G_{\beta}(f - i_1, g - i_2) \nabla g \cdot \frac{dR^{-1}}{d\theta}(x - T) \mu^{-1} \log \frac{p(f, g)(i_1, i_2)}{p(f)(i_1)p(g)(i_2)} di_1 di_2 dx$$

and

$$\frac{\partial MI(f, g)}{\partial T} = -\frac{1}{|\Omega|} \int_{\Omega} \int_{R^2} \partial_2 G_{\beta}(f - i_1, g - i_2) \nabla g \cdot R^{-1} \mu^{-1} \log \frac{p(f, g)(i_1, i_2)}{p(f)(i_1)p(g)(i_2)} di_1 di_2 dx$$

With the definitions and deduction above, the evolution equations associated with the

Euler-Lagrange equation of Equation 2-21 are

$$\frac{\partial u}{\partial t} = \delta(u) \operatorname{div} \left(\left(g + \frac{\lambda_1}{2} d^2 \right) \frac{\nabla u}{|\nabla u|} \right) - \lambda_2 u \quad (2.25)$$

$$\frac{\partial u}{\partial n} = 0, x \in \partial\Omega, t > 0; u(x, 0) = u_0(x), x \in \Omega \quad (2.26)$$

$$\frac{\partial \mu}{\partial t} = -\lambda_1 \int_{\Omega} \delta(u) d \nabla d \cdot (Rx) |\nabla u| dx - \lambda_3 \frac{\partial MI(f, g)}{\partial \mu}, t > 0, \mu(0) = \mu_0 \quad (2.27)$$

$$\frac{\partial \theta}{\partial t} = -\lambda_1 \int_{\Omega} \delta(u) \mu d \nabla d \cdot \left(\frac{dR}{d\theta} x \right) |\nabla u| dx - \lambda_3 \frac{\partial MI(f, g)}{\partial \theta}, t > 0, \theta(0) = \theta_0 \quad (2.28)$$

$$\frac{\partial T}{\partial t} = -\lambda_1 \int_{\Omega} \delta(u) d \nabla d |\nabla u| dx - \lambda_3 \frac{\partial MI(f, g)}{\partial T}, t > 0, T(0) = T_0 \quad (2.29)$$

where R is the rotation matrix in terms of the angle θ , d is evaluated at $\mu Rx + T$

2.2.3 Parameter Choosing

Generally speaking, the problem of determining the parameters $\lambda_i > 0 (i = 1, 2, 3)$ is not trivial. It depends on the specific problem. For a new type of image, it is a time consuming work to find the appropriate parameters. In this section, we present an alternative approach, that is not only able to incorporate both shape and segmentation, but also be able to provide the better estimate for the parameter used in the model. Our model is a coupled optimization problem, which consists of a minimization and a maximization problems. The minimization problem is

$$\min_{u, \mu, R, T} E_{\lambda}(u, \mu, R, T)$$

with

$$E_{\lambda}(u, \mu, R, T) = \min_{\lambda_1, \lambda_2, \lambda_3, \mu, R, T, u} \int_{\Omega} \delta(u) g(|\nabla I|) |\nabla u| + \frac{\lambda_1}{2} \int_{\Omega} \delta(u) d^2 (C^*, \mu Rx + T) |\nabla u| + \frac{\lambda_2}{2} \int_{\Omega} f_{\gamma}(x) u^2(x) dx \quad (2-30)$$

The maximization problem is

$$\min_{\mu_\lambda, R_\lambda, T_\lambda} F(\mu_\lambda, R_\lambda, T_\lambda)$$

with

$$F(\mu_\lambda, R_\lambda, T_\lambda) = MIIG_{V_{e0}} \left(I^*(x), I(\mu_\lambda^{-1} R_\lambda^{-1} (x - T_\lambda)) \right) \quad (2-31)$$

where MIIG is the mutual information of image geometry defined in section (2.2.1.2), and $\mu_\lambda, R_\lambda,$ and T_λ together with u_λ are solutions of Equation 2-30 corresponding to a fixed λ . The energy functional in Equation 2-30 is increasing in λ . Without the joint problem (Equation 2-31), E_λ in Equation 2-30 takes the smallest value when $\lambda = (0,0)$, that reduces to the energy functional for geometric active contour. It will leak through the boundaries with weak gradients. By maximizing the energy functional in Equation 2-31 over all the possible solutions $\mu_\lambda, R_\lambda,$ and T_λ of Equation 2-30 corresponding to λ , we can get an optimal estimate for λ , and hence a better segmentation corresponding to this λ .

2.3 Experiments and Results

In this section, the proposed methods are applied on different applications. In real applications, it is possible that there are no all 3 kinds of prior information (shape, key points and intensity profile), any available prior of those 3 can be used for model (2-21).

In the following experiments, we will show the results of shape analysis, generation of intensity profile, segmentation with gradient and prior shape information, segmentation with gradient, prior shape and key points information, segmentation with gradient, prior shape and intensity profile information.

Most of the experiments are for ultrasound cardiac images. Because the task of determining the epicardial and endocardial borders of the left ventricular (LV) on

echocardiography images is essential for quantification of cardifunction. It is very difficult due to poor contrast and information dropout at the borders, the inhomogeneity of intensities inside and outside the regions between epicardial and endocardial borders, and the low signal to noise ratio.

2.3.1 Shape Analysis

In this experiment, the shape analysis method introduced in section 2.2.1.1 is applied. Epicardial and endocardial borders segmentations of 167 patients on 4 chamber ultrasound cardiac images, which are given by experts, are used as training set in this experiment. The task of this experiment is to cluster those shapes and find the average shape for each cluster. Among those patients, there are 112 normal and 55 abnormal. For each patient, there are 4 shapes given by expert, namely: ED (end diastole) Endo (endocardial), ED Epi (epicardial), ES (end systole) Endo, ES Epi.

Applying Equation 2-1, 2-3 and the “*near basis cluster method*”. 167 sets of shapes were divided into 17 clusters with the cluster coefficient 0.1. 112 normal sets were in 3 clusters, 55 abnormal sets were in 14 clusters. Figure 2-2 shows the clustering results and the average shapes of normal patients. Figure 2-2A is the biggest cluster of normal patients, there are 79 patients in this cluster. The yellow curves are all 79 ED Epi and 79 ES Epi. The red curves are all 79 ED Endo and 79 ES Endo. Those “*”s show the *average* contour of ED Epi and ES Epi. Those “+”s show the *average* contour of ED Endo and ES Endo. From A, we can see that those contours in the same cluster are very tight, which means that shapes in the same cluster are similar. Figure 2-2B to C show the *average* contours of the 3 normal clusters without showing all contours. The green “*” with yellow curve is ES Epi. The green “*” with red curve is ED Epi. The blue “+” with yellow curve is ES Endo. blue “+” with red curve is ED Endo. B) is the average of 79

patients, C) is the average of 24 patients, D) is the average of 1 patient. We can see the shape in D) is very different than B) and C).

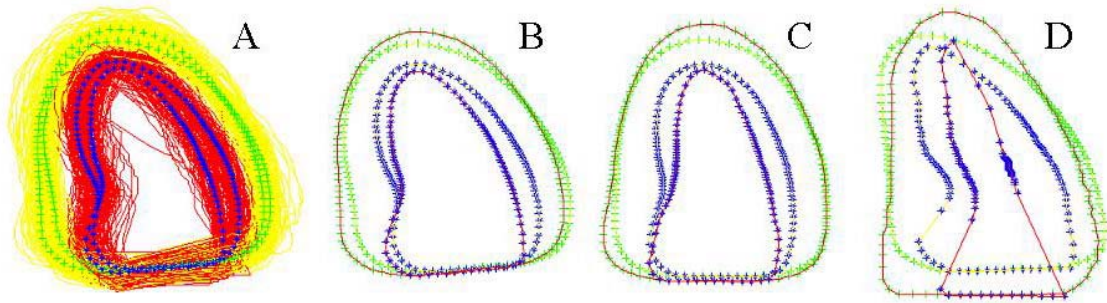


Figure 2-2. Cluster and average result. A) The biggest cluster of normal patients with all 79 sets of curves, B) The *average* shapes of the first normal cluster, C) The *average* shapes of the second normal cluster, D) The *average* shapes of the third normal cluster

Figure 2-3 shows some examples of the *average* shapes of abnormal clusters. For 55 abnormal patients, 14 clusters were generated with the cluster coefficient 0.1. Again, The green '*' with red curve is ED Epi. The blue '+' with yellow curve is ES Endo. blue '+' with red curve is ED Endo.

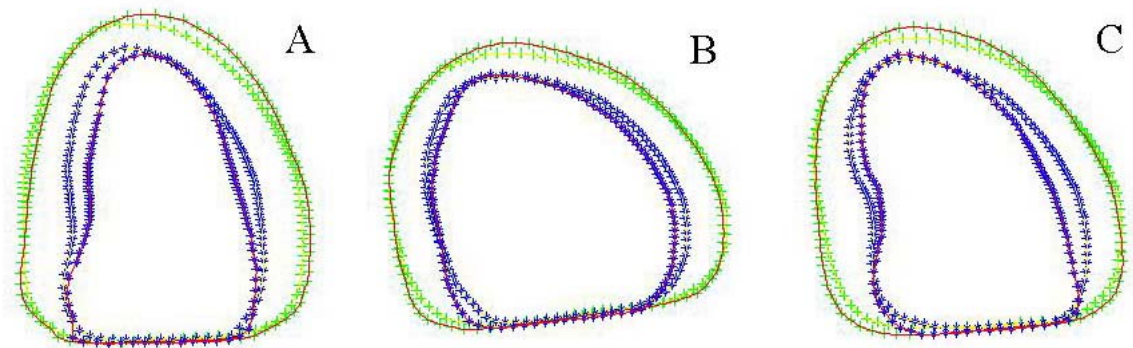


Figure 2-3. Example of average shapes of abnormal clusters. A) the *average* shape of the biggest cluster with 10 patients, B) the *average* shape of the biggest cluster with 9 patients, C) the *average* shape of the biggest cluster with 8 patients

2.3.2 Intensity Profile

We applied the algorithm in section 2.2.1.2 on 2-chamber cardiac ultrasound images. The method was tested against one cluster of a database of 85 apical 2 chamber

end diastolic (ED) echo cardiographs. Images acquired retrospectively from 61 normal patients. The images were grouped into three clusters. The 20 images from one of the clusters with expert traced epicardial borders superimposed are displayed in Figure 2-4.

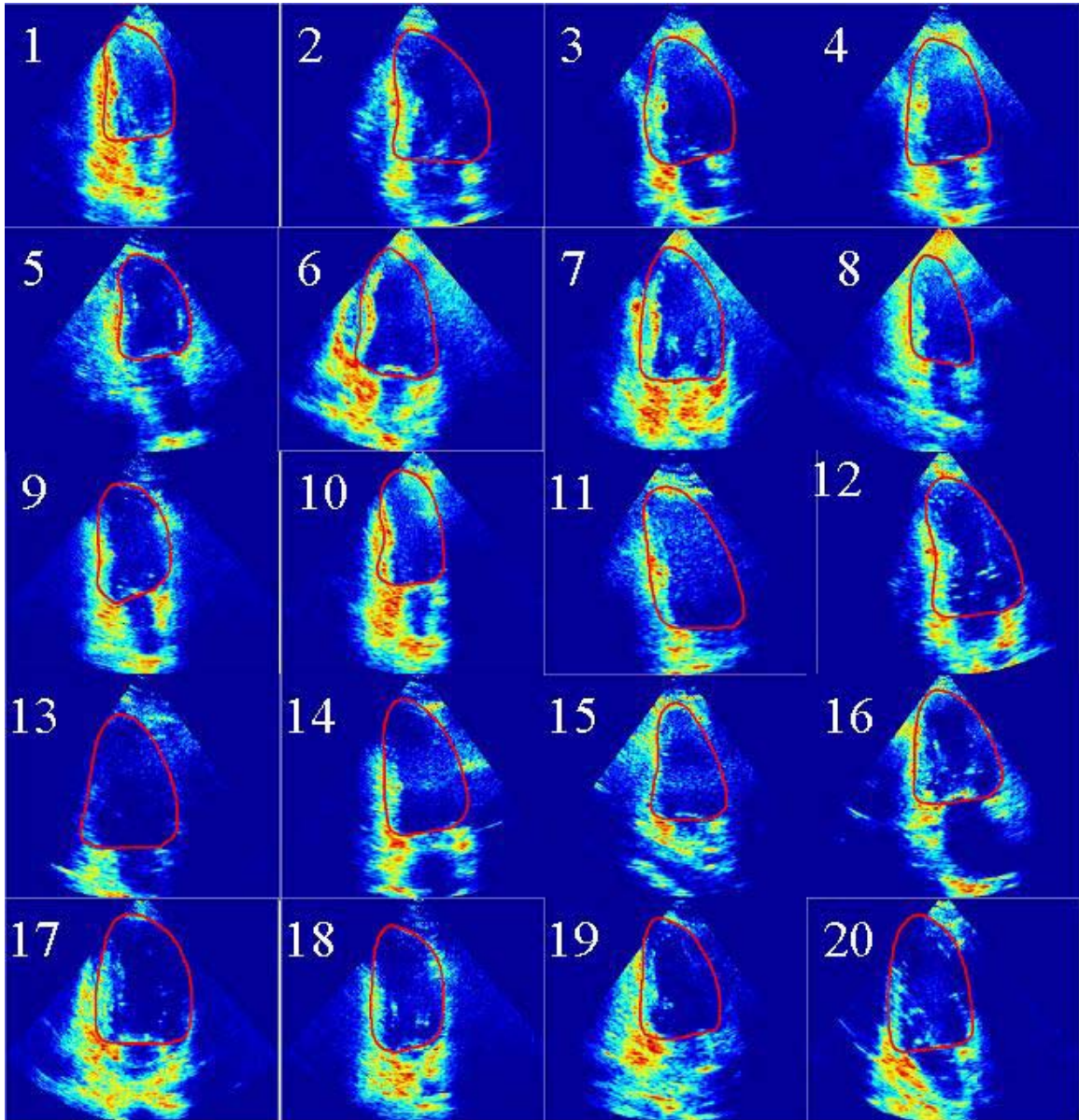


Figure 2-4. Twenty training images with the segmented epicardiums used as training images and shapes

Using Equation 2-12 described in section 2.2.1.2, the intensity profile for each average shape was computed. The average shape C^* and the associated average intensity

profile I^* for this cluster with 20 images is displayed in Figure 2-5. Figure 2-5A shows the direct *average* of those images, i.e. simply set a_j in Equation 2-13 be $1/20$. Figure 2-5B shows the *average* of those images with a_j determined by using Equation 2-12. From Figure 2-5, we can see that A is more blurred than B. Moreover, we computed the sum in Equation 2-12 for the a_j determined by using Equation 2-12 and $a_j = 1/20$. The results were 196.73 and 184.08 respectively, confirming our suspicion that the weighted average is better.

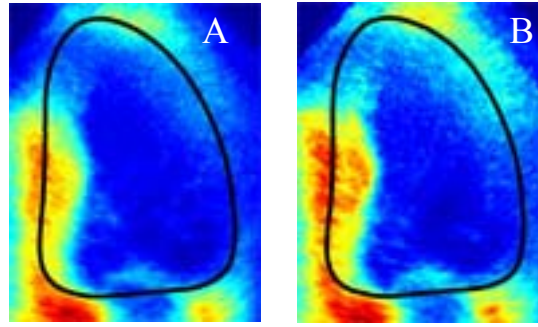


Figure 2-5. Average images of the above 20 images with the average contour superimposed. A) by equally weighted these aligned images, B) by the proposed method

2.3.3 Segmentation with Prior Shape Information

In this section, we assume that only the shape prior information is available.

Hence Equation 2-21 changes to be

$$\min_{\lambda_1, \lambda_2, \lambda_3, \mu, R, T, u} \int_{\Omega} \delta(u) g(|\nabla I|) |\nabla u| + \frac{\lambda_1}{2} \int_{\Omega} \delta(u) d^2(C^*, \mu R x + T) |\nabla u| \quad (2-32)$$

And according to Equation 2-25 to 2-29 the evolution equations are

$$\frac{\partial u}{\partial t} = \delta(u) \operatorname{div} \left(\left(g + \frac{\lambda_1}{2} d^2 \right) \frac{\nabla u}{|\nabla u|} \right) \quad (2-33)$$

$$\frac{\partial u}{\partial n} = 0, x \in \partial\Omega, t > 0; u(x, 0) = u_0(x), x \in \Omega \quad (2-34)$$

$$\frac{\partial \mu}{\partial t} = -\lambda_1 \int_{\Omega} \delta(u) d \nabla d \cdot (Rx) \|\nabla u\| dx, t > 0, \mu(0) = \mu_0, \quad (2-35)$$

$$\frac{\partial \theta}{\partial t} = -\lambda_1 \int_{\Omega} \delta(u) \mu d \nabla d \cdot \left(\frac{dR}{d\theta} x \right) \|\nabla u\| dx, t > 0, \theta(0) = \theta_0 \quad (2-36)$$

$$\frac{\partial T}{\partial t} = -\lambda_1 \int_{\Omega} \delta(u) d \nabla d \|\nabla u\| dx, t > 0, T(0) = T_0 \quad (2-37)$$

We have tested our model on synthetic images and ultrasound images.

2.3.3.1 Synthetic image

The aim of the first experiment was to verify that the active contour with the prior shape could fill in the “gaps” in a boundary. We used the first two terms in Equation 2-21 for this experiment.

Figure 2-6A shows a curve that we used as the prior shape for this experiment. Figure 2-6B shows an image of a white semicircular disc on a black background. The boundary of the semicircular disc should be thought of as the boundary of the prior shape after some partial occlusion. The task is to see whether the active contour with prior shape information can utilize this partial boundary while filling in the rest. The active contour was initialized as the ellipse as shown in Figure 2-6B. Evolving the active contour according to the level set formulation of Equations 2-34 to 2-37 with the parameters $\beta = 1$, $\sigma = 0.5$ (in $g(x)$), $\lambda_1 = 1$, $dt = 0.02$, $\mu_0 = 1.4$, $\theta_0 = 0$, $T_0 = (0,0)$ we get the stationary contour C in Figure 2-6C. The transformation parameters are $\mu = 1.25$, $\theta_0 = 0.50$, and $T_0 = (-2.14, -2.13)$ (pixels). In Figure 2-6D, the prior shape C^* , and the contour $\mu RC + T$ are shown as the white and the dotted curves. From Figures C and D we can see that the contour C captures the high gradient in the image I and the prior shape C^* even though complete gradient information is not available.

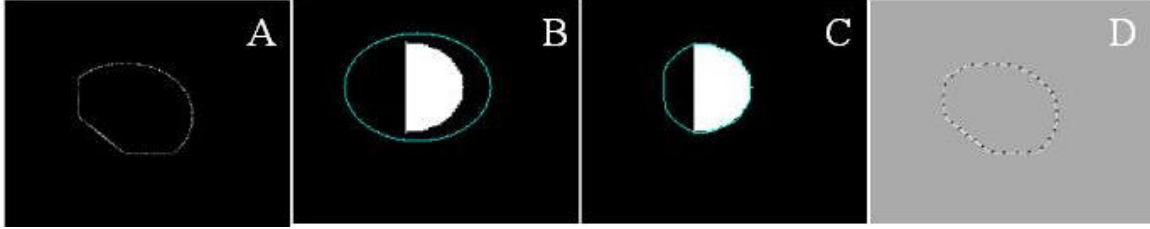


Figure 2-6. Segmentation with prior shape for synthetic image. A) The prior shape C^* , B) The image with the initialized active contour (the ellipse), C) The final stationary contour, D) The contour C^* (solid curve), and the contour $\mu RC^* + T$ (dotted curve)

2.3.3.2 Cardiac ultrasound images

The aim of the second experiment was to segment the epicardium (the outer boundary of the myocardium surrounding the left ventricle) in a 4-chamber image of the heart (Figure 2-7B). The epicardium is not completely imaged in the image, and our task is to find and complete the boundary using a prior shape.

The prior shape (Figure 2-7A) is the average epicardial boundary generated in section 2.3.1 of the biggest normal group with 79 patients, The contour shown in Figure 2-7B was used as an initial contour. This contour was evolved according to the Equations 2-34 to 2-37, and it finally stopped at the location of the solid contour in Figure 2-7C. To validate this result we had the expert manually segment the epicardium. The dotted contour in Figure 2-6C is the expert's epicardium. Our segmentation is close to the expert's. The parameters used in this experiment are $\beta = 1$, $\sigma = 0.5$ (in $g(x)$), $\lambda_1 = 2$, $dt = 0.05$, $\mu_0 = 1$, $\theta_0 = 0$, $T_0 = (0,0)$. The solutions we obtained are the contour C in Figure 2-6C, and the transformation parameters $\mu = 0.66$, $\theta_0 = 0.10$, and $T_0 = (-0.88, -0.10)$ (pixels). In Figure 2-6D we present the contour $\mu RC + T$ for inspection. It is similar to the average shape C^* in Figure 2-7A.

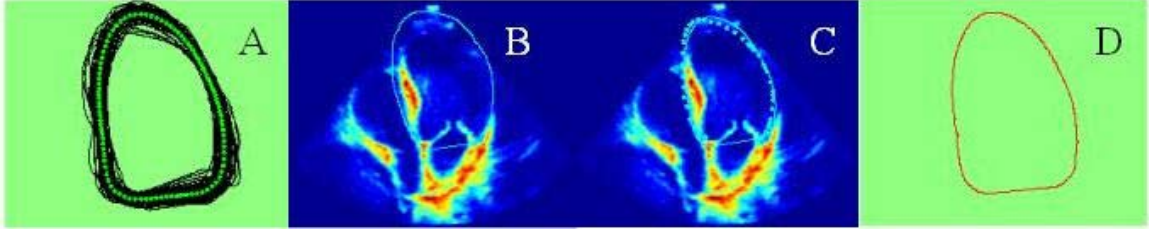


Figure 2-7. Segmentation with prior shape for cardiac image. A) A cluster of 79 epicardiums and the *average* shape C^* , B) The initial contour in the ultrasound image, C) The final stationary contour (solid curve) and the expert's epicardium (dotted curve), D) The contour $\mu RC^* + T$.

2.3.4 Segmentation with Prior Shape Information and Key Points

In this section, we assume that both prior shape and key points are available.

Hence the energy functional changes to be

$$\min_{\lambda_1, \lambda_2, \lambda_3, \mu, R, T, u} \int_{\Omega} \delta(u) g(|\nabla I|) |\nabla u| + \frac{\lambda_1}{2} \int_{\Omega} \delta(u) d^2(C^*, \mu R x + T) |\nabla u| + \frac{\lambda_2}{2} \int_{\Omega} f_{\gamma}(x) u^2(x) dx \quad (2-38)$$

And according to Equation 2.25 to 2.29 the evolution equations are

$$\frac{\partial u}{\partial t} = \delta(u) \operatorname{div} \left(\left(g + \frac{\lambda_1}{2} d^2 \right) \frac{\nabla u}{|\nabla u|} \right) - \lambda_2 u \quad (2-39)$$

$$\frac{\partial u}{\partial n} = 0, x \in \partial \Omega, t > 0; u(x, 0) = u_0(x), x \in \Omega \quad (2-40)$$

$$\frac{\partial \mu}{\partial t} = -\lambda_1 \int_{\Omega} \delta(u) d \nabla d \cdot (R x) |\nabla u| dx, t > 0, \mu(0) = \mu_0, \quad (2-41)$$

$$\frac{\partial \theta}{\partial t} = -\lambda_1 \int_{\Omega} \delta(u) \mu d \nabla d \cdot \left(\frac{dR}{d\theta} x \right) |\nabla u| dx, t > 0, \theta(0) = \theta_0 \quad (2-42)$$

$$\frac{\partial T}{\partial t} = -\lambda_1 \int_{\Omega} \delta(u) d \nabla d |\nabla u| dx, t > 0, T(0) = T_0 \quad (2-43)$$

2.3.4.1 Synthetic image

The aim of the first experiment is to verify that the active contour with the prior shape and points can fill in the “gaps” in a boundary in a meaningful way in the sense of passing through the prior points.

Figure 2-8A shows a typical binary image with three points and an ellipse superimposed on it. The ellipse and points are used as the prior shape and points in this experiment, respectively. The object to be segmented is partially occluded, and the shape of its boundary is nonequivalent to the prior shape. We want to see whether the active contour with the prior shape and points can utilize the partial boundary while filling in the rest.

The active contour was initialized as a solid contour shown in Figure 2-8C. Evolving the active contour according to Equation 2-39 to 2-43 with the parameters $\lambda_1 = 0.12$, $\lambda_2 = 0.08$, $\sigma = 0.5$ (in $g(x)$), $dt = 0.05$, $\mu_0 = 1$, $\theta_0 = 0$, $T_0 = (0,0)$, we get the stationary contour C (the dotted one) in Figure 2-8C, and the transformation parameters $\mu = 0.91$, $\theta_0 = -0.14$, and $T_0 = (-0.5, 0.3)$ (pixels). We can see that even though complete gradient information is not available, the contour C captures the high gradient in the image I , passes through three prior points, and forms a shape similar but not the same as the prior C^* . To show the advantage of using prior points we compare the segmentation results obtained by using model (2-38) with (2-32). Figure 2-8B shows the segmentation result by using model (2-32). In Figure 2-8B the solid contour represents the shape prior and initial contour, while the dotted contour is the segmentation result. Since the prior points are not incorporated in the model (2-32) the segmented contour only captures the prior shape and high gradient. It can't accurately capture local shape variation.

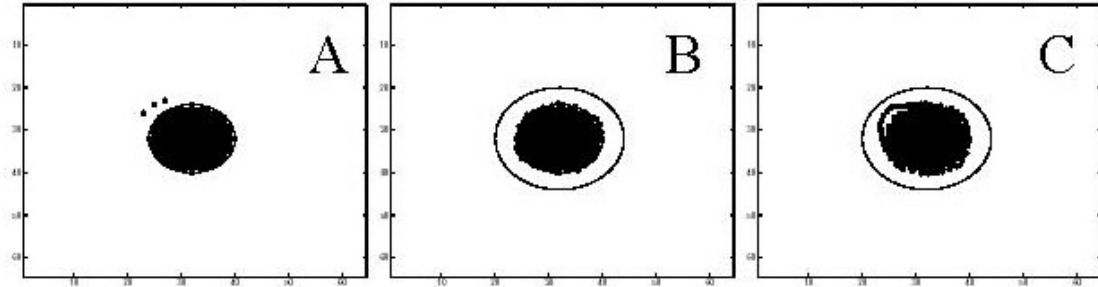


Figure 2-8. Segmentation with prior shape and key points for synthetic image. A) An image with the prior shape and three points superimposed, B) The segmentation result using Equation 2-32 (dotted) and the initial contour (solid), C) The segmentation result using Equation 2-38 (dotted) and the initial contour (solid).

2.3.4.2 Cardiac image

The aim of the second experiment is to segment the endocardium (the inner boundary of the myocardium surrounding the left ventricle) in a two-chamber image of the heart (Figure 2-9A for a typical image). The endocardium is not completely imaged in the image, and its shape is not the same as the “average shape” (the shape prior). Our task is to determine the endocardium using “average shape” and five points given by an expert.

The prior shape is created by the same way as that in section 2.2.1.1. For this particular problem to create the prior shape, endocardial boundaries were outlined in patients by an expert echo-cardiographer. The boundaries were grouped as explained in section 2.2.1.1. Figure 2-9B shows the “average contour” for one of the clusters (the dotted contour), the endocardium outlined by an expert (the solid contour), and five points on the expert’s contour, That are in the location where the image gradients are low, and the local shape distortions are larger. Figure 2-9C presents the image $|\nabla G_\sigma * I|$. From this

image we can see the dropout of image information at several parts of the endocardium. are $\beta = 1$, $\sigma = 0.5$ (in $g(x)$), $\lambda_1 = 2$, $dt = 0.05$, $\mu_0 = 1$, $\theta_0 = 0$, $T_0 = (0,0)$.

To segment the endocardium in the image shown in Figure 2-9A, the active contour was initialized as the contour shown in Figure 2-9A. This contour was evolved according to the Equations 2-39 to 2-43 and it finally stopped at the location of the dotted contour in Figure 2-9D. We also obtained the transformation parameters $\mu_0 = 1.0024$, $\theta_0 = -0.1710$, and $T_0 = (-24.6, 32.3)$. The solid contour in Figure 2-9D is the expert's endocardium.

We can see that our segmentation is close to the expert's. To see the shape variation between the solution of Equation 2-38 and "average shape" we aligned the solution of Equation 2-38 onto the "average shape" using the solutions μ, R, T of Equation 2-38. Figure 2-9E shows the disparity in shape between these two contours. The dotted contour is the transformed solution of Equation 2-38, and the solid one is the "average shape". We can see that our active contour formed a shape different from the prior one in order to capture the high gradients and given points. Figure 2-9F provides the segmentation result obtained by using model (2-32) against the expert's endocardium. In this figure the dotted contour is the solution of Equation 2-32, and the solid contour is the expert's endocardium. Comparing Figure 2-9D with Figure 2-9F, we can see that the solution of Equation 2-38 is closer to the expert's contour than that of Equation 2-32. Figure 2-9G presents the shape comparison between the solution of Equation 2-32 and the prior. We can see that they are very similar. Since Equation 2-32 is not able to incorporate prior points, its solution can only capture the high image gradients and the "average shape", but it can't provide a desirable segmentation as the expert's endocardium.

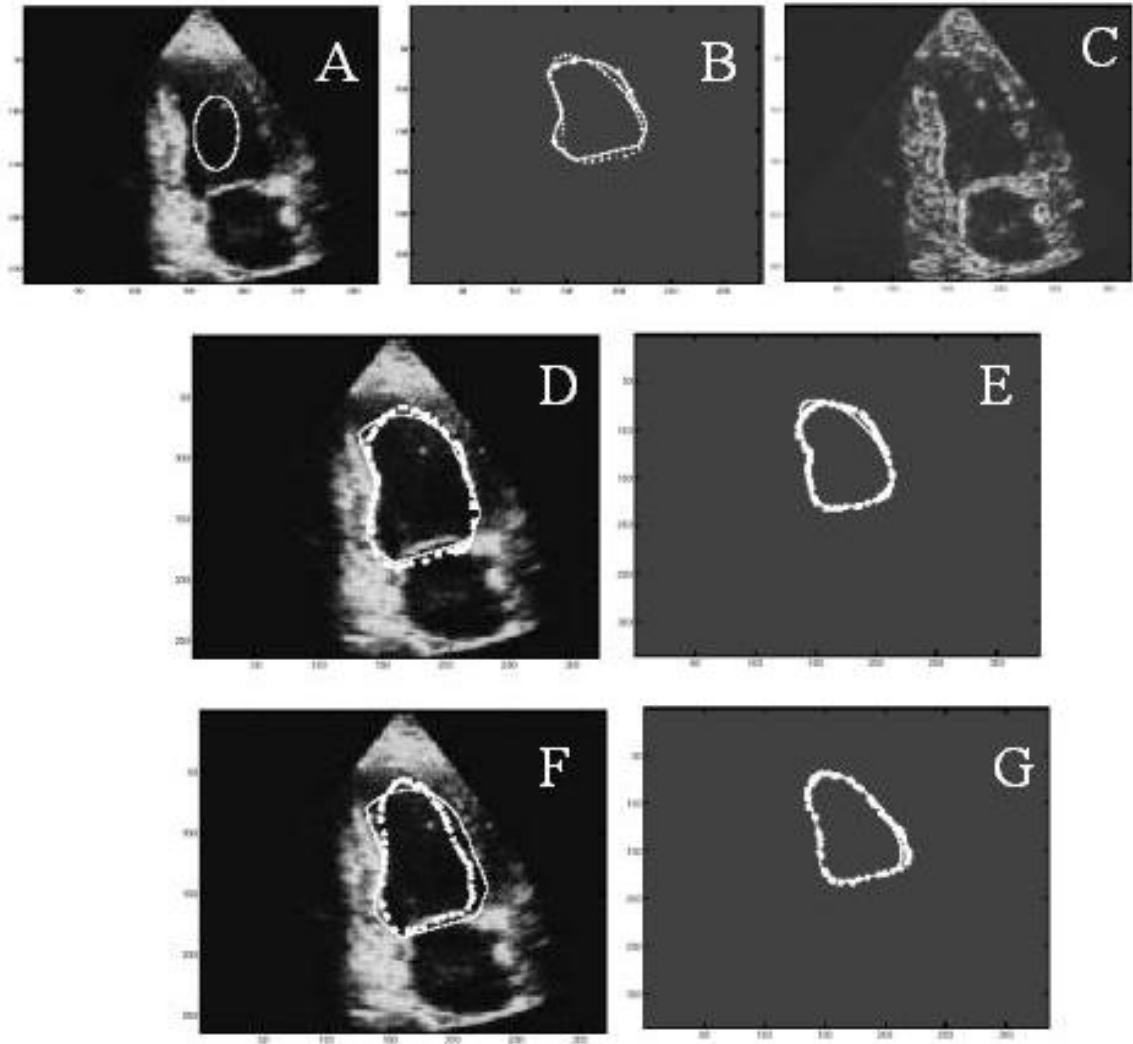


Figure 2-9. Segmentation with prior shape and key points for cardiac image 1. A) a typical 2-chamber ultrasound image with an initial contour; B) Expert's endocardium (solid contour), "average shape" (dotted contour), and five points on the expert's contour, C) The image $|\nabla G_\sigma * I|$; (D). The endocardium segmented by using Model 2-38 (dotted) and the expert's contour (solid), (E) The transformed solution of Equation 2-38 (dotted), and the "average shape", F). The endocardium segmented by using Model 2-32 (dotted) and the expert's contour (solid), G) The transformed solution of Equation 2-32 (dotted), and the "average shape".

The last experiment is repeating the second experiment in another 2-chamber ultrasound image. The aim and the procedure of this experiment are the same as the second one. We list the figures below for the results of this experiment in the same order

as above. The segmentation is given in Figure 2-10D represented by the dotted contour, the transformation parameters are $\mu_0 = 0.9883$, $\theta_0 = -0.1981$, and $T_0 = (-28.7, 49.1)$.

From these results and figures we can have the same conclusions as that found in the second experiment.

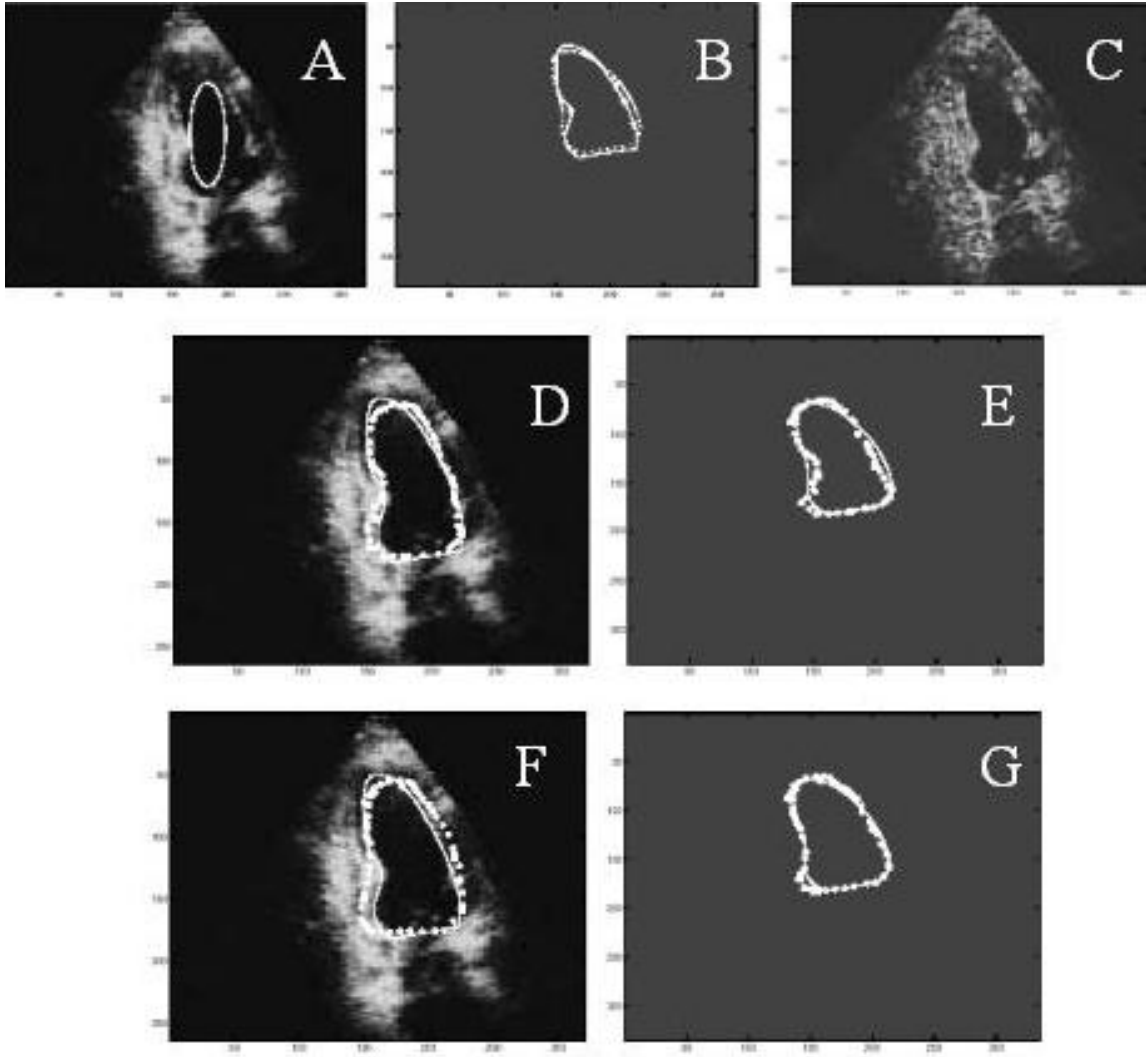


Figure 2-10. Segmentation with prior shape and key points for cardiac image 2. A) a typical 2-chamber ultrasound image with an initial contour, B) Expert's endocardium (solid contour), "average shape" (dotted contour), and five points on the expert's contour, C). The image $|\nabla G_\sigma * I|$ (D). The endocardium segmented by using Model 2-38 (dotted) and the expert's contour (solid), E) The transformed solution of Equation 2-38 (dotted), and the "average shape", F). The endocardium segmented by using Model 2-32 (dotted) and the expert's contour (solid), G) The transformed solution of Equation 2-32 (dotted), and the "average shape."

2.3.5 Segmentation with Prior Shape and Intensity Profiles

In this algorithm, we assume prior shape and intensity profile is available. Hence the energy functional (2-24) changes to be

$$\min_{\lambda_1, \lambda_2, \lambda_3, \mu, R, T, u} \int_{\Omega} \delta(u) g(|\nabla I|) |\nabla u| + \frac{\lambda_1}{2} \int_{\Omega} \delta(u) d^2(C^*, \mu R x + T) |\nabla u| - \lambda_3 \text{MIIG}_{V_{\epsilon_0}}(I^*(x), I(\mu^{-1} R^{-1}(x - T)))$$

Because the heavy computation duty of MIIG in the evolution and the parameter choice complexity, we used the method introduced in 2.2.3. Then according to Equations 2-30 and 2-31 the coupled energy functional pair is

$$E_{\lambda}(u, \mu, R, T) = \min_{\lambda, \mu, R, T, u} \int_{\Omega} \delta(u) g(|\nabla I|) |\nabla u| + \frac{\lambda}{2} \int_{\Omega} \delta(u) d^2(C^*, \mu R x + T) |\nabla u| \quad (2.44)$$

$$F(\mu_{\lambda}, R_{\lambda}, T_{\lambda}) = \text{MIIG}_{V_{\epsilon_0}}(I^*(x), I(\mu_{\lambda}^{-1} R_{\lambda}^{-1}(x - T_{\lambda}))) \quad (2.45)$$

Notice Equation 2-44 is same as Equation 2-32. Hence the associated Euler-Lagrange equations of Equation 2-44 are Equations 2-33 to 2-37.

However, how to solve Equation 2-45 efficiently still remains an open question. In our experiments we first solved Equation 2-44 to get a sequence of solutions

$(C_{\lambda_i}, \mu_{\lambda_i}, R_{\lambda_i}, T_{\lambda_i})$ corresponding to a sequence of $\lambda_i, i = 1, \dots, k$. Then we computed

$F(\mu_{\lambda_i}, R_{\lambda_i}, T_{\lambda_i})$ in Equation 2-45 for each $1 \leq i \leq k$. In this computation we partitioned

the intensities into 16 bins, and used the discrete form of Shannon entropy to calculate the

MIIG. If $F(\mu_{\lambda_j}, R_{\lambda_j}, T_{\lambda_j})$ is the smallest one among them, we took $(C_{\lambda_j}, \mu_{\lambda_j}, R_{\lambda_j}, T_{\lambda_j})$ as

our model solutions. In this way we could get a better estimate for λ , and hence, a better

segmentation, that captures high gradients, shape prior, and intensity profile. However, it

may not be the best, since the comparison of the energy values in Equation 2-45 was only

for finitely many λ 's.

We applied this algorithm on 2-chamber cardiac ultrasound images. The epicardiums and the endocardiums in these images were not completely imaged, and our task was to find and complete the epicardial and endocardial boundaries using prior shape and intensity profile.

To create the prior shape, epicardial boundaries were outlined by an expert echocardiographer on 85 images acquired at ED from 62 patients. Using the method described in section 2.2.1.1, the boundaries were grouped into three clusters and the *average* shape of each cluster was computed. Using the method described in section 2.2.1.2, the intensity profile for each *average* shape was computed. The *average* shape C^* and the associated *average* intensity profile I^* for one cluster is displayed in Figure 2-5B. To segment the epicardial border in a novel image displayed in Figure 2-11B, we used the *average* contour and intensity profile near the contour in Figure 2-5B as the priors.

The active contour was initialized with the ellipse displayed in Figure 2-11A. Evolving the active contour using Equations 2-33 to 2-37 with a fixed λ , we obtained segmentation C_λ together with a similarity transformation $(\mu_\lambda, R_\lambda, T_\lambda)$, that are the solutions of Equation 2-44. By varying λ we generated a sequence of solutions of Equation 2-44. We chose the optimal value of λ to be the one maximizing Equation 2-45. Finally, the solutions for the Model 2-44 coupled with Equation 2-45 were chosen as the solutions of Equation 2-44 corresponding to this optimal λ

The first column of the Table 2-1 displays 8 different values of λ . By the procedure described above we obtained $C_{\lambda_i}, \mu_{\lambda_i}, R_{\lambda_i}, T_{\lambda_i} (i = 1, \dots, 8)$. The third and the fourth columns present the $MI_{V_{e_0}} (I^*(x), I(\mu_{\lambda_i}^{-1} R_{\lambda_i}^{-1} (x - T_{\lambda_i})))$ and

$MIIG_{V_{\epsilon_0}}(I^*(x), I(\mu_{\lambda}^{-1}R_{\lambda}^{-1}(x - T_{\lambda})))$ respectively. Since the 4th column of this table is largest when $\lambda = 0.04$, we selected the solutions of Equation 2-13 to correspond to this choice of $\lambda = 0.04$. The segmentation (solid) corresponding to this λ is shown in Figure 2-11B together with the expert traced border (dotted). The distance between the expert and algorithm generated borders are tabulated in column 2 of the table. It is defined as

$$\sum_{i=1}^N d_{C^*}(C(p_i)) / N, \text{ where } d_{C^*} \text{ is the distance function of } C^*, \text{ and}$$

$C(p)(0 \leq p \leq N, p_1 = 0, p_N = 1)$ is our segmentation. The units of the distance are the numbers of the pixels, and the pixel size is 0.62mm×0.62mm. From this table we see that the segmentation corresponding to $\lambda = 0.04$ is the one having smallest distance from expert's contour and largest value of MIIG. This statement is not true for MI.

Table 2-1. Experiment results with different λ for Epi

λ	dist	MI	MIIG
0.04	3.1142	1.8894	7.9971
0.20	3.2903	1.9192	7.9794
0.40	3.3552	1.9207	7.9698
2	3.3962	1.9579	7.9623
20	4.7160	1.9207	7.8914
40	6.6697	2.0133	7.7524
0.02	25.4498	0	0
0.004	26.2190	0	0

The second row in Figure 2-11 displays this experimental result. The segmentations (solid) in Figure 2-11B and C are the solutions of Equation 2-44 with $\lambda = 0.04$ and $\lambda = 20$, respectively. Comparing the segmentation results with the expert's borders (dotted) this figure provides visual confirmation of the result presented in the table.

To further test the method, we also used the same initial contour and the 'optimal' value $\lambda = 0.04$ determined in the previous test in two additional images. The

segmentation results (solid) together with expert's border's (dotted) are presented in Figures 2-11D to G. The segmentations in the left and right columns are the solutions of Equation 2-44 corresponding to $\lambda = 0.04$ and $\lambda = 20$ respectively. Comparing the results in the left column of Figure 2-11 with those in the right column, we observe that $\lambda = 0.04$ also provides good segmentations in these two new images indicating that the 'optimal' estimate of λ from one image can possibly be used for other members of the cluster. Of course, the shapes of the object boundaries and their intensity profiles must be similar.

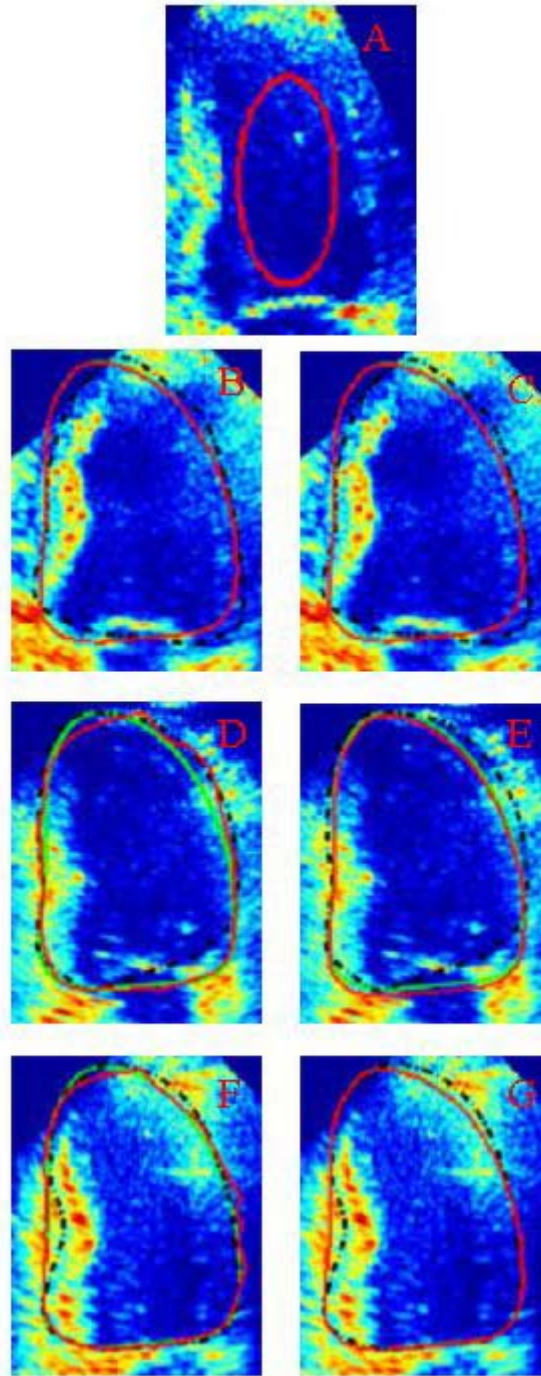


Figure 2-11. Segmentation with prior shape and intensity profile for epicardiums. A) An ellipse used as the initial contour in our experiments for three images in the following three rows, (B)-(G). Each row presents the segmentations (solid, red), expert's borders (dotted, black), and average shape (green) in an image. The segmentations in the left column and right column are the solutions of Equation 2-44 corresponding to $\lambda = 0.04$ and $\lambda = 20$ respectively.

Moreover, the proposed model is less sensitive to the initial step than the edge-based active contours, since the propagation of the contour is influenced by intensity profiles in addition to image gradients.

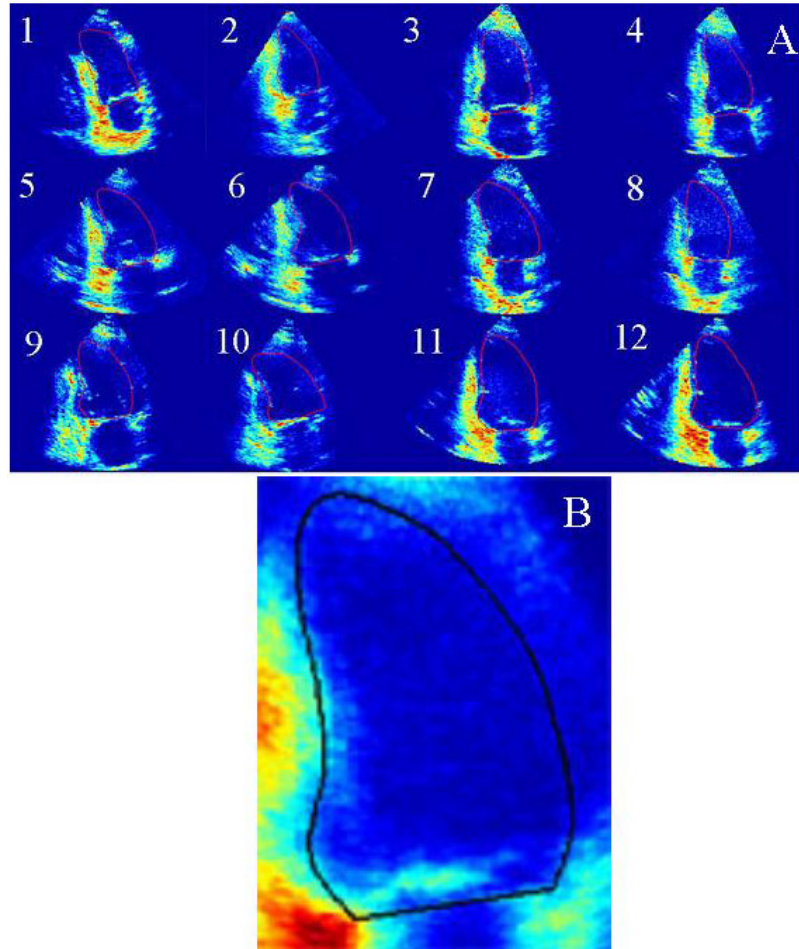


Figure 2-12. Intensity profile for endocardiums. A) 12 training images with the segmented endocardiums used as training images and shapes, B) *Average* endocardiums with associated intensity profiles generated from the training shapes and images in A) by the proposed algorithms.

We also applied our algorithm to segment the endocardiums in ultrasound images. The shape model of endocardium and the prior intensity profiles across the shape model shown in Figure 2-12B were generated from a set of 12 training shapes and their associated images shown in Figure 2-12A by using our proposed method explained above.

To segment the endocardial border in a novel image displayed in Figure 2-13B, we used the *average* contour and intensity profile near the contour in Figure 2-12B as the priors.

Table 2-2. Experiment results with different λ for Endo

λ	dist	MI	MIIG
0.1	1.97	1.3711	6.8060
0.2	2.14	1.4390	6.7197
0.01	2.36	1.1653	6.6282
0.001	2.78	1.0783	6.4244
1.0	8.18	1.1719	6.4050

Table 2-2 shows the choice of λ . We observed the same phenomena as that in the previous table that the larger the MIIG is, the smaller the distance of the segmentation from the expert's contour is. This statement is again not true for MI. From this table we see that the segmentation corresponding to $\lambda = 0.1$ is the optimal value of λ , and the solution corresponding to this λ is the model solution of Equation 2-44. Figure 2-13 has the same organization as Figure 2-11. Again, by comparing the left column with the right column, it is evident that the model solutions are closer to the expert's contour than the solution of Equation 2-44 with other value of λ .

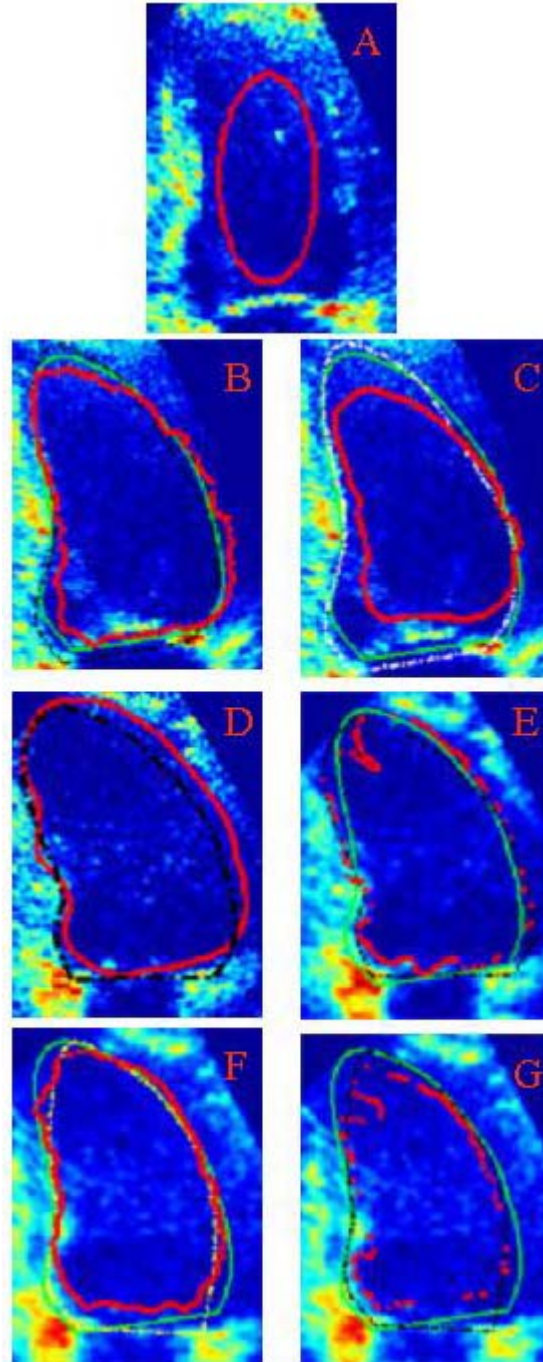


Figure 2-13. Segmentation results for endocardiums. A) An ellipse used as the initial contour in our experiments for three images in the following three rows, (B)-(G). Each row presents the segmentations (solid, red), expert's borders (dotted, black), and average shape (green) in an image. The segmentations in the left column and right column are the solutions of Equation 2-44 corresponding to $\lambda = 0.1$ and $\lambda = 1$ respectively.

2.4 Conclusion

We proposed a framework for segmentation that incorporates different prior information. The prior information could be shape, key points or intensity profile. We also proposed a level set formulation and a numerical algorithm for the active contour. In applications, the framework can be modified to be different model for the priors available. Several examples for different prior information were given in the experiment section.

According to experiments for segmentation with prior shape information, the active contour could reliably segment images in which the complete boundary was either missing (the ultrasound images) or was low resolution and low contrast (fMRI). Besides the segmentation, the algorithm also provides estimates of translation, rotation, scale that map the active contour to the prior shape. These estimates are useful in aligning images.

In the experiments for segmentation prior shape and key points, we add the prior information on a few points to a variational framework in level set formulation to make up the drawback of those models that use only the gradient and shape information. These prior points are got from expert and are known to be passed by the contour we are looking for. Since the distance of a point on a curve from that curve is zero, by using level set formulation we can incorporate the prior points into active contours with shape by creating an energy term. This energy is designed such that when it is minimized, the surface, where the interface is embedded, takes value close to zero at the prior points. The experiment results showed that the proposed model using both prior shape and points greatly improves the segmentation result comparing with the active contours with shape but without prior points.

In the experiment for segmentation that incorporates the shape and intensity priors in active contours, we solve a coupled optimization problem. The energy function in one part of the model is a weighted sum of the energy of the geometric active contour and a shape related energy. The minimizer of this energy function presents the segmentation and the transformation that aligns the segmentation to the prior shape. The second part of the model provides an optimal estimate of the weight used in the first one by maximizing the MIIG of the intensity prior and the aligned novel image near the feature over all the alignments that are the solutions of the first part corresponding to different weights.

The improvements of this model over existing active contour algorithms are in two aspects. First, we used maximizing MIIG rather than MI to match intensity profiles of two images. The reason for doing this is that the MIIG takes neighborhood intensity distribution into account, and hence, gives better description of intensity profile than MI. Secondly, the parameter in the model of active contour with shape can be selected by model itself, and the segmentation with the optimized parameter arrives at higher image gradients, forms a shape similar to the prior, and captures the prior intensity profile. Moreover, the coupling idea can be used for any models where the solution is impacted by three forces.

We applied our model to the problem of cardiac boundary determination in ultrasound images, for which the methods using edge or region information only can not give a good result. Even the active contours with shape prior struggle with such data. The proposed model was tested against a database of epicardial borders traced by an expert on echocardiographic images acquired from the apical 2-chamber view. The preliminary results were encouraging.

There are still some drawbacks of this framework. First, because of the shape term this model does not allow big shape difference. However, a significant local shape difference may occur in application. Therefore, we are now working on more non-rigid model. The other drawback is that the initial curve cannot be far from the desired segmentation. The reason is that there may be some regions have high gradient between initial curve and the desired segmentation. In that case, initial curve will be stopped by that high gradient. At last, the computation for MIIG is expensive. Hence, an alternative way for computation of MIIG is necessary.

CHAPTER 3

APPLICATION OF PDE BASED INPAINTING ON MR PARALLEL IMAGING

Inpainting is an image interpolation method. PDE based digital inpainting techniques are finding broad applications. This chapter shows the first work in which PDE based inpainting techniques are applied into the field of MR parallel imaging. First, a novel model and its corresponding numerical method are initially introduced. Then two applications of this model on MR Parallel Imaging are introduced.

The first application of this model is for sensitivity maps. Coil sensitivity maps are important in parallel imaging and they often need extrapolation and hole filling (holes being dark regions of low signal in MR images). All of these problems can be solved simultaneously by applying inpainting techniques. Experiments for determining coil sensitivity maps for phantoms, Neurovascular and cardiac MR images demonstrate the speed and accuracy of the proposed model. Images generated using SENSE utilizing inpainted sensitivity maps, raw sensitivity maps and over-smoothed sensitivity maps are compared.

The second application is for intensity correction map. The goal of this study is to find a technique which can generate uniform image with optimized Signal to Noise Ratio (SNR) for Multi-channel RF array coils. Experiments for images from different popular systems show that the inpainted intensity correction map can generate uniform image without losing SNR.

3.1 Introduction

3.1.1 Inpainting

Image inpainting was originally an artistic phrase referring to an artist's restoration of a picture's missing pieces. Computer techniques could significantly reduce the time and effort required for fixing digital images, not only to fill in blank regions but also to correct for noise. Digital inpainting techniques [36, 79-82] are finding broad applications such as, image restoration, dis-occlusion, perceptual image coding, zooming and image super-resolution, error concealment in wireless image transmission, etc. Due to its broad range of applications, various methods for inpainting have been developed, ranging from nonlinear filtering methods, wavelets and spectral methods, statistical methods (especially for textures), etc. The most recent approach to non-texture inpainting is based on the PDE method and the Calculus of Variations. According to Chan and Shen [80] PDE based TV models and the Mumford-Shah model work very well for inpainting problems with a more local nature such as hole filling (holes being regions of low signal in MR images). Hole filling is the most important issue in the correction of MR sensitivity maps (which are generally derived from MR images).

3.1.2 Sensitivity Maps

Sensitivity maps are meant to contain the sensitivity information of RF probe coils in MRI systems. Highly accurate knowledge of the spatial receiver sensitivity is required by both SMASH (SiMultaneous Acquisition of Spatial Harmonics [83]) and SENSE (Sensitivity Encoding [16, 84]). Sensitivity maps are also crucial to correcting the inhomogeneities of MRI surface coils. It must be noted that accurate sensitivity information can only be obtained where signal is present. Some data sets with large areas contributing little or no signal. Such dark regions (i.e. holes) are common, for example, in

pulmonary MRI using Fresh Blood Imaging (FBI). In this case sensitivity map interpolation techniques are required to fix the holes. To deal with slightly varying tissue configurations and motion, extrapolation over a limited range is also necessary. We therefore need a technique, which is capable of simultaneously interpolating and extrapolating. There are some existing techniques for this purpose, such as the polynomial fit procedure [16], thin-plate splines [85], wavelets [86], and Gaussian kernel smoothing [87]. Those methods are based on the assumption that the sensitivity map is sufficiently smooth (i.e., containing no sharp variations). By our experiments, this assumption is not always true. If the sensitivity map is piecewise smooth, which is usually true for non-uniform loading, the existing methods are not sufficient. The inpainting model proposed here is a technique to handle interpolation and extrapolation for piecewise smooth maps simultaneously.

3.1.3 Intensity Correction Map

In the areas of medical imaging, acquired images may be corrupted by poor signal to noise ratio (SNR) or non-uniformity in spatial intensity. Multi-channel RF array coils produce a multitude of individual images. These images may be combined to produce a single composite image with high SNR. The standard technique for this process is the so-called sum-of-squares (SOS) algorithm, however, consideration of the correlation of noise between channels also permits a somewhat better algorithm, commonly referred to as the optimal reconstruction [88]. This algorithm produces nearly the highest SNR attainable, at each pixel, given the individual channel images. The limitation of these algorithms is that for coil array elements with very high sensitivities, non-uniformity in the resultant image is likely to occur. To correct non-uniformities, a correction map is usually used to multiply the non-uniform image and generate a uniform one. The

correction map could be the inverse of the convolution of non-uniform image with Gaussian filter [87], or the inverse of the surface coil's sensitivity map [89, 90]. Our experiments show the correction map generated by with Gaussian filter could be over smoothed and substantial noise amplification can occur, which hinders the visualization of salient features. Accurate sensitivity map is an appropriate tool for intensity correction. If the sensitivity map is not accurate, then noise may be amplified. However, to generate accurate sensitivity map for intensity correction requires external reference and may take long time. On the other hand, those methods and some other methods provide a low SNR uniform image. Given a low SNR uniform reference and the high SNR “sum of squares” inpainting technique can be applied to generate a correction map, which can correct the non-uniformity and keep high SNR of “sum of squares.”

3.2 Methods

In this section we first review the conventional Total Variational (TV) inpainting model. Then modified models are proposed for the applications in parallel imaging. The corresponding numerical method is given for implementation. Methods for correction of sensitivity map and intensity correction map are also introduced.

It will be helpful to first explain the following terms. The process by which holes are fixed using inpainting is referred to as diffusion. There are two basic types of diffusion, isotropic and anisotropic. In isotropic diffusion, pixels in hole regions are fixed by assigning them a value equal to the isotropically weighted average value of their surrounding neighbors. Isotropically here meaning the weights will be independent of direction from the pixel, but decreasing with distance. Anisotropic diffusion involves assigning these pixels values obtained by extending the intensity contours from non-hole regions into hole regions along the intensity level set. The “intensity level set” being

simply the contour lines of equal intensity in an image, i.e., the set of equi-intensity curves. Intensity here refers only to the magnitude of the complex pixel values.

3.2.1 Review of TV Inpainting Model

If the inpainting problem is treated as an input-output system, then the input is the image u^0 which needs inpainting along with the specification of the hole regions (dark regions), D , in the image. The output is a de-noised image u without any holes.

The hole-free part of the image, where inpainting is not needed, is not supposed to be changed much. Mathematically we wish to keep u and u^0 as close as possible on the parts of the image not contained in D . For this purpose we define,

Ω : the image domain

$\Omega \setminus D$: the area where the image information is contained, which is referred to as “known locations.”

Let us define,

$$\lambda_D(x) = \begin{cases} 0, & x \in D \\ 1, & x \in \Omega \setminus D \end{cases} \quad (3-1)$$

Then the desired similarity of u and u^0 at “known locations” can be achieved through minimizing the term, $\int_{\Omega} \lambda_D(x) (u - u^0)^2 dx$. This term is called the fidelity term.

To reconstruct the missing parts without losing local image texture (i.e., near the holes), it is necessary that the image model smoothly extends the image into the holes and preserves the edges of objects contained in the image. This can be achieved through minimizing [22, 36]

$$\int_{\Omega} |\nabla u| dx \quad (3-2)$$

This term is used to smooth and extend the image along the intensity level set, hence this term is called the smoothing term.

The conventional TV model combines these two terms and is given as,

$$E[u | u^0, D] = \frac{1}{2} \int_{\Omega} \lambda_D(x) (u - u^0)^2 dx + \alpha \int_{\Omega} |\nabla u| dx \quad (3-3)$$

where α is a parameter used to balance the smoothing and fidelity terms. Given u^0 and D , the u which minimizes the energy functional will be the inpainting result.

3.2.2 Modification of the Exponent of $|\nabla u|$ in the TV Model

The main feature of the conventional TV model is its ability to preserve edges given the fact that the anisotropic diffusion is always perpendicular to ∇u [91].

Minimizing $\int_{\Omega} |\nabla u| dx$ makes sure that the smoothing is along the level set and therefore preserves and enhances edges. However, there are limitations that arise when reconstructing piecewise smooth images or those, in which the noise and the edges are extremely difficult to distinguish, which is often true for sensitivity maps. In smooth regions, isotropic diffusion is appropriate to remove noises. If traditional TV model is applied on to a region where noise and edges are difficult to distinguish, then anisotropic diffusion is applied and those noises are kept. Because the exponent of $|\nabla u|$ determines the type of diffusion (isotropic or anisotropic), this naturally leads to models in which the exponent of $|\nabla u|$ is a function $P(X)$ [27]. More specifically, one might want to consider

$P = P(|\nabla u|)$ where, $\lim_{y \rightarrow 0} p(y) = 2$ and $\lim_{y \rightarrow \infty} p(y) = 1$.

Therefore we may wish to minimize

$$\int_{\Omega} |\nabla u|^{P(x, |\nabla u|)} dx \quad (3-4)$$

where P can either be a constant, $P \equiv 1$ or $P \equiv 2$, or where P can be a function,

$$P(x, |\nabla u|) = \begin{cases} 1 + g(x) = 1 + \frac{1}{1 + \beta |\nabla G_\sigma * u_0|^2} & , |\nabla \lambda_D| = 0 \\ 2 & , |\nabla \lambda_D| > 0 \end{cases} \quad (3-5)$$

where β, σ are parameters.

β is used to accentuate the edges between regions of different intensities, larger β will better preserve edges. σ is for the Gaussian function, $G_\sigma = \exp(-|x|^2 / (4\sigma^2)) / \sigma$, which is used to smooth the image by the standard method of weighted averages. At areas of fairly uniform intensity, $|\nabla u|$ is small, causing $P(x)$ to be large. Hence the diffusion is more isotropic. At edges between regions with very different intensities, $|\nabla u|$ is large so that $P(x)$ will be close to 1; anisotropic diffusion is then applied so that the edges will be preserved. For the edges between D and $\Omega \setminus D$, $|\nabla \lambda_D|$ is larger than 0, hence $P(x)$ will be set to 2 and image will be isotropically extended. Therefore the goal of choosing $P(x)$ is to control the type of diffusion at specific locations in the image, so that isotropic and anisotropic diffusion are effectively combined (with little threshold sensitivity). Specifically, total variation diffusion is used to preserve edges and create varying combinations of isotropic and anisotropic diffusion in regions that may or may not contain significant features.

3.2.3 Modified TV Model for Sensitivity Maps

In order to apply the model to sensitivity maps, the conventional model may be modified based on the particular application. There will be a sensitivity map u_j for each coil j . Let I_j be the image generated by coil j , and let I be the homogeneous image, then

u_j^0 is defined as I_j / I . In order to avoid singularities and to consider every coil,

$\int_{\Omega} \lambda_{D_j}(x)(u - u^0)^2 dx$ should be replaced by

$$\sum_j \int_{\Omega} \lambda_{D_j}(x)(u_j I - I_j)^2 dx \quad (3-6)$$

If the square root of the sum of squares of the I_j s is used as the homogeneous image I (i.e., sum-of-squares image), then the sum of squares of every coil's sensitivity map will be unity at each pixel. Therefore

$$\int_{\Omega} \left(\sqrt{\sum_j u_j^2} - 1 \right)^2 dx \quad (3-7)$$

is to be minimized, where u_j is the inpainted sensitivity map for the j th probe coil. Then the modified TV model for the sensitivity map is,

$$E[u_j | u_j^0, D] = \frac{1}{2} \sum_j \int_{\Omega} \lambda_{D_j}(x)(u_j I - I_j)^2 dx + \gamma \sum_j \int_{\Omega} |\nabla u_j|^{p(x, |\nabla u_j|)} dx + \frac{\mu}{2} \int_{\Omega} \left(\sqrt{\sum_j u_j^2} - 1 \right)^2 dx \quad (3-8)$$

where γ, μ are used to balance the terms in energy functional. Increasing γ in Eq. 8 will result in a smoother image. Larger μ makes the square root of the sum-of-squares of the sensitivity maps closer to unity.

3.2.4 Numerical Implementation Method

The Euler-Lagrange equation for Equation 3-8 is

$$\lambda_{D_j}(x)(u_j I - I_j)I - \gamma \nabla \cdot (|\nabla u_j|^{p-2} P \nabla u_j) + \mu \left(1 - \frac{1}{\sqrt{\sum_j u_j^2}} \right) u_j = 0 \quad (3-9)$$

with boundary condition $\partial u_j / \partial \bar{n} = 0$, for the j th coil. where \bar{n} is the outward unit normal to the image boundary,

To derive the evolution equations corresponding to the Euler-Lagrange equation, the following difference scheme [92] can be applied in order to discretize Equation 3-9.

Let u be an image, then define

$$\begin{aligned}\Delta_-^x u_{kl} &= u_{kl} - u_{k-1,l}, \Delta_+^x u_{kl} = u_{k+1,l} - u_{k,l} \\ \Delta_-^y u_{kl} &= u_{kl} - u_{k,l-1}, \Delta_+^y u_{kl} = u_{k,l+1} - u_{k,l}\end{aligned}$$

and then

$$\nabla u_{kl} = (\Delta_+^x u_{kl}, \Delta_+^y u_{kl})$$

where k, l correspond to rows and columns of the image respectively.

Let $\bar{v} = (v_1, v_2)$ be a vector field and let h be the step space for this field (generally equal to unity), then according to [92]

$$\text{div}(\bar{v}) = \frac{\Delta_-^x v_1 + \Delta_-^y v_2}{h},$$

Applying the difference scheme above, the iteration formula for Equation 3-9 is

found to be,

$$u_j^{n+1} = \frac{\gamma [C_1 u_{k+1,l}^{n,j} + C_2 u_{k-1,l}^{n,j} + C_3 u_{k,l+1}^{n,j} + C_4 u_{k,l-1}^{n,j}] + \lambda_{D_j} I_j I}{\lambda_{D_j} I^2 + \gamma (C_1 + C_2 + C_3 + C_4) + \mu \left(1 - \frac{1}{\sqrt{\sum_j u_j^2}} \right)} \quad (3-10)$$

where

$$C_1 = \frac{p_{kl}}{a_{kl}}, \quad C_2 = \frac{p_{k-1,l}}{a_{k-1,l}}, \quad C_3 = \frac{p_{kl}}{b_{kl}}, \quad C_4 = \frac{p_{k,l-1}}{b_{k,l-1}}$$

$$a_{kl} = \left((\Delta_+^x u_{kl}^n)^2 + \left(\frac{u_{k,l+1}^n - u_{k,l-1}^n}{2} \right)^2 \right)^{\frac{2-p_{kl}}{2}}$$

$$b_{kl} = \left((\Delta_+^x u_{kl}^n)^2 + \left(\frac{u_{k+1,l}^n - u_{k-1,l}^n}{2} \right)^2 \right)^{\frac{2-p_{kl}}{2}}$$

with j corresponding to the j th coil, k, l corresponding to rows and columns of the image respectively, and n corresponding to the n th iteration.

Pixels in I (the sum-of-squares image) with intensity below some particular threshold will be treated as holes, i.e., belonging to D . This threshold can be automatically determined in several ways. One simple approach is finding the maximum pixel intensity in the entire image and setting the threshold to be 0.05 times this value [i.e., $0.05 \times (\text{maximum intensity})$].

A good initial guess for u_j can reduce the number of iterations involved in applying Equation 3-10. Raw sensitivity maps for each coil, defined as

$$u_{j_raw}(x) = \begin{cases} I_j(x) & x \notin D \\ I(x) & x \in D \\ guess & x \in D \end{cases}$$

are used as the initial guess for u_j . In our experiments, the magnitude of *guess* above is the average intensity of I_j , the phase of *guess* is taken to equal the phase of I_j . Another issue associated with sensitivity maps is the fact that they contain complex data.

Therefore we can either inpaint the vector map directly or inpaint the magnitude and phase part separately. Our experiments showed no explicit improvement through the use of inpainted phase maps. Hence to save inpainting time we only apply inpainting to the magnitude of the sensitivity map, and the phase of I_j is used for u_j .

3.2.5 Modified TV Model for Intensity Correction Map

To protect the signal to noise ratio, the intensity correction map needs to be isotropically smooth. Hence the inpainting model for intensity correction map is

$$E[u | u^0, D] = \frac{1}{2} \int_{\Omega} \lambda_D(x) (u - u^0)^2 dx + \alpha \int_{\Omega} |\nabla u|^2 dx \quad (3-11)$$

where α is a parameter to balance smooth term and fidelity term. There are many numerical ways to minimize this energy functional. One general way is to solve its Euler

- Lagrange equation: $\lambda_D(x)(u - u^0)I - \alpha \nabla(\nabla u) = 0$ with boundary condition $\frac{\partial u}{\partial \vec{n}} = 0$. By

the same difference scheme, it follows the Iteration Scheme

$$u_{k,l}^{n+1} = \frac{\alpha [u_{k+1,l}^n + u_{k-1,l}^n + u_{k,l+1}^n + u_{k,l-1}^n] + \lambda_D}{\lambda_D + 4\alpha} \quad (3-12)$$

3.3 Experiments and Results

In this section, the proposed inpainting techniques are applied to two applications. One is probe coil sensitivity map, the other one is intensity correction map. Notice that those two kinds of maps are all the division of two images. To avoid singularity, there are some region without values (holes). To fix those holes without losing texture is the main target. And inpainting is good tool to fix holes. Therefore, inpainting technique can be applied to any map, which is division of two images. In all of those experiments, Matlab codes are run on a COMPAQ PC with 1G Hz CPU and 1G RAM.

3.3.1 Application on Sensitivity Map

The proposed inpainting model Equation 3-8 was applied as sensitivity map correction. The corrected sensitivity maps were then used by SENSE in the reconstruction of MR images. The accuracy and efficiency of conventional inpainting technique can be seen in [36, 80, 82]. To show the accuracy of the modified model for

sensitivity map, we first apply the proposed the method to a phantom without holes. Some holes were randomly chosen and inpainted. The results were then compared with the original sensitivity map that has no holes. Since the actual sensitivity map is not known in real applications, we were unable to determine directly if an inpainted sensitivity map was good or not. Therefore we applied the inpainted sensitivity maps to reconstruct an MR image and then compare the reconstructed image with the reference image (which is generated by using all of k -space as opposed to SENSE which only utilizes part of the k -space data). Let the phrase “intensity difference” refers to the difference in magnitudes between the reconstructed and reference-images at each pixel. We define the “ghost ratio” as the magnitude of the “intensity difference” (at each pixel) summed over every pixel in the image divided by the sum of the absolute values of each pixel in the reference image. The “ghost ratio” is actually the relative error. Notice that the intensity of reconstructed image by SENSE will be lower than reference image because of the lower energy in K -space. According to Parseval’s equation, the intensity of all reconstructed image were calibrated by multiplying reduce factor when calculate the “intensity difference” in all experiments.

An alternative way to fix holes is to apply Gaussian kernel smoothing (12). For the sake of comparison with our method (i.e., the modified TV model), sensitivity maps corrected by Gaussian kernel smoothing (GKS) and raw sensitivity maps are also applied to SENSE.

In many real applications, a low-resolution image is used to produce a sensitivity map. According to [93], it is possible to extract the sensitivity map directly from a fully sampled central band of k -space. (The center of the band being the center of k -space, with

the band extending along the complete width in the frequency encode direction, but leaving out the top and bottom sections of the k -space.) Since the acquisition of the sensitivity map data and the data to be reconstructed occurs simultaneously, errors due to sensitivity mis-calibration are eliminated. An alternative method for acquiring the sensitivity map for dynamic MR (such as a cardiac series) is to apply one high-resolution sensitivity map (i.e., utilizing the entire k -space) for a complete time sequence. Both methods are tested in our experiments to show the flexibility of the inpainting technique.

The choice of parameters may depend on the system and loading. According to experiments, the model is not very sensitive to the choice of parameters. In our experiments, we set $\beta = 1, \sigma = 0.25, \gamma = 10$ and $\mu = 1$.

3.3.1.1 Phantom with no intrinsic holes

The phantom was constructed from a 197mm (7.75") ID by a 180mm long acrylic tube that was filled with a solution of Cu_2SO_4 (2.0 grams/Liter) and NaCl (4.5 grams/Liter). Fig 1-a is a photo of this phantom. Data was then collected by a 1.5 T SIEMENS system (FOV 300 mm, matrix 128×128 , TR 300 ms, TE 15 ms, flip angle 90° , Slice thickness 5 mm, number of averages 1) with an 8-channel tuned loop array of coils. The time required for the calculation of 8 sensitivity maps was 4.35 seconds.

If we ignore the container there are no holes at all in the original sensitivity map. Figure 3-1B shows the magnitude of the original sensitivity map of coil 1. 5 holes were then randomly made in the original sensitivity map. Figure 3-1C shows those holes. Figure 3-1D shows the inpainted result for coil 1. The local patterns are perfectly preserved in the inpainted result.

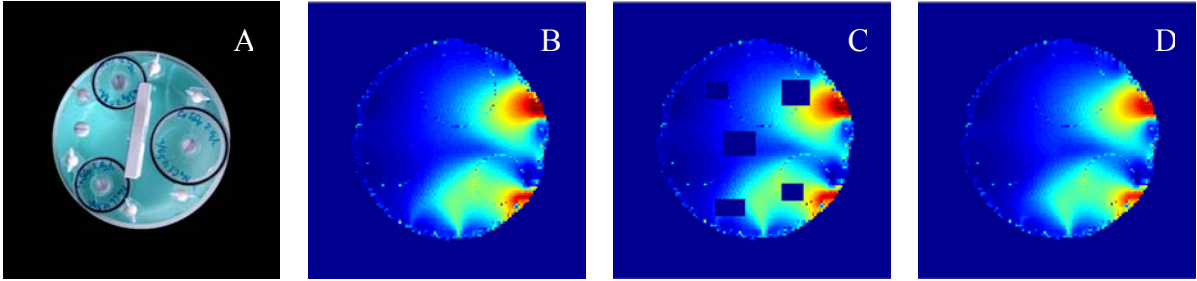


Figure 3-1. Inpainting results for the artificial holes. The maps shown in B-D are for coil 1. A) Photo of the phantom, B) magnitude of the reference sensitivity map, C) magnitude of the sensitivity map with 5 randomly chosen holes B) magnitude of the inpainted sensitivity map by the proposed method

We define the “relative error” as the sum over the absolute value of the difference between the inpainted result, and the original sensitivity, for each pixel in the map over the sum of the magnitudes of the original sensitivity map. Table 3-1 shows the relative error of each channel. The average relative error of all 8 channels using the modified TV method is 0.71%. The average relative error using GKS is 4.45%.

Table 3-1. The relative error of inpainted results

coil	Relative error by inpainting	Relative error by GKS
1	0.49%	3.52%
2	0.40%	4.45%
3	1.84%	7.57%
4	0.70%	4.87%
5	0.46%	3.44%
6	0.29%	2.61%
7	1.08%	4.12%
8	0.44%	4.97%
average	0.71%	4.45%

3.3.1.2 Coronal phantom

Figure 3-2 and Table 2 show results for a Coronal Phantom collected by a 1.5 T GE system (FOV 480 mm, matrix 256×256, TR 500 ms, TE 13.64 ms, flip angle 90°, Slice thickness 3 mm, number of averages 1) with an 8-channel Neurovascular Array coil. The time required for the calculation of 8 sensitivity maps was 16.11 seconds.

In this experiment, high-resolution sensitivity maps are generated by using images reconstructed utilizing the full K-space for each coil. Low-resolution sensitivity maps are generated by using images reconstructed with the 31 central rows of fully sampled data. Low-resolution sensitivity maps are more likely to be used in real applications.

Figure 3-2A is the Reference Image, which is reconstructed utilizing the full K-space. Figures 3-2B to 3-2D show the magnitude of the sensitivity map of coil 6. Figure 3-2B is the magnitude of the raw sensitivity map. Figure 3-2C shows the result of inpainting applied to 3-2B, while Figures 3-2D is the result of applying GKS to 3-2B. From Figures 3-2C, it can be seen that inpainted sensitivity maps have no holes and thus extend the map to the entire image. Furthermore, in Figures 3-2C, the local patterns are perfectly preserved. Figures 3-2E to H show the intensity difference between images reconstructed by SENSE with a K-space reduction factor of 4 (i.e., using 25% of the full K-space data) and the reference image, those images use the same gray scale map. Figure 3-2E shows this intensity difference when the reconstruction is done using high-resolution inpainted sensitivity maps. Figure 3-2F shows this intensity difference when the reconstruction is done using high-resolution raw sensitivity maps while 3-2G shows this intensity difference for GKS corrected sensitivity maps. From Figure 3-2E to G, it is seen that the result obtained by using inpainted sensitivity maps is much better than that obtained by using either the raw sensitivity maps or the GKS sensitivity maps. Figure 3-2H shows the intensity difference obtained using low-resolution inpainted sensitivity maps. Figures 3-2H also shows that even in this case result is still better than that obtained by the use of high-resolution GKS sensitivity maps.

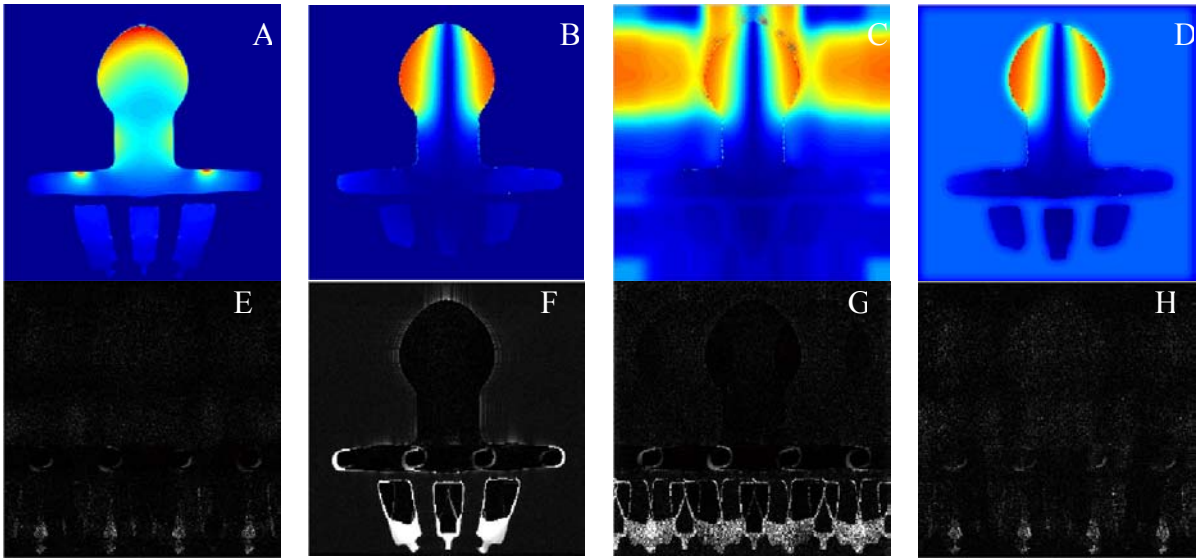


Figure 3-2. Inpainting results for coronal phantom. A) Reference Image, B) magnitude of the raw sensitivity, C) magnitude of the inpainted sensitivity map, D) magnitude of the sensitivity map by Gaussian kernel smooth, E) The intensity difference by using high resolution inpainted sensitivity map, F) The intensity difference by using raw high resolution inpainted sensitivity map, G) The intensity difference by using high resolution Gaussian Kernel smoothed sensitivity map, H) The intensity difference by using low resolution inpainted sensitivity map, E) to H) use the same gray scale map

Table 3-2 gives the ghost ratios obtained through the use of difference sensitivity maps. The term, R_factor , refers to the reduction factor of K-space. It can be seen that the results obtained by using the inpainted sensitivity maps have much lower ghost ratios for each reduction factor than the results obtained by using raw sensitivity maps. Notice that the results obtained from the high-resolution GKS sensitivity maps are very similar to those obtained from the low-resolution GKS sensitivity maps. The reason for this is that the GKS correction involves an isotropically smooth blurring of the image, which is very similar to the isotropic blurring which results due to an image being low resolution. An image reconstructed through the use of a fully sampled central region of K-space also results in an isotropically smoothed version of the reference image, since this is also a low-resolution image. (This is true since any point in K-space is a superposition of signals from each point in the slice.) For a uniform phantom, these two maps(a low-

resolution GKS map and a high-resolution GKS map) may generate similar results. For the same reason that low resolution results in an isotropic smoothing, the images from inpainted low-resolution sensitivity maps are similar to those resulting from GKS sensitivity maps.

Table 3-2. Ghost ratio of coronal phantom

	R_factor = 2	R_factor = 3	R_factor = 4
Inpainted high resolution	1.06%	3.12%	2.24%
Raw high resolution	6.07%	7.41%	6.41%
GKS high resolution	2.18%	4.48%	4.76%
Inpainted low resolution	2.03%	4%	4.6%
Raw low resolution	6.7%	7.96%	7.26%
GKS low resolution	2.20%	4.48%	4.72%

3.3.1.3 Neurovascular images

Both Figure 3-3 and Table 3-3 show the results for Neurovascular Images collected by a 1.5 T GE system (FOV 440 mm, matrix 256×192, TR 1000 ms, TE 13.504 ms, flip angle 90°, Slice thickness 2 mm, number of averages 2) through the use of a fast spin echo pulse sequence with an 8-channel Neurovascular Array coil. The time required for the calculation of 8 sensitivity maps was 15.01 seconds

The contents of Figure 3-3 and Table 3-3 are similar to that of Figure 3-2 and Table 3-2. The reduce-factor for Figure 3-3 E to Figure 3-3 H is also 4. Table 3-3 again shows that the results obtained by using inpainted sensitivity maps have much lower ghost ratios for each reduction factor.

For Figure 3-3H, the low-resolution sensitivity maps are generated by using images reconstructed with the 31 central rows of fully sampled k -space data.

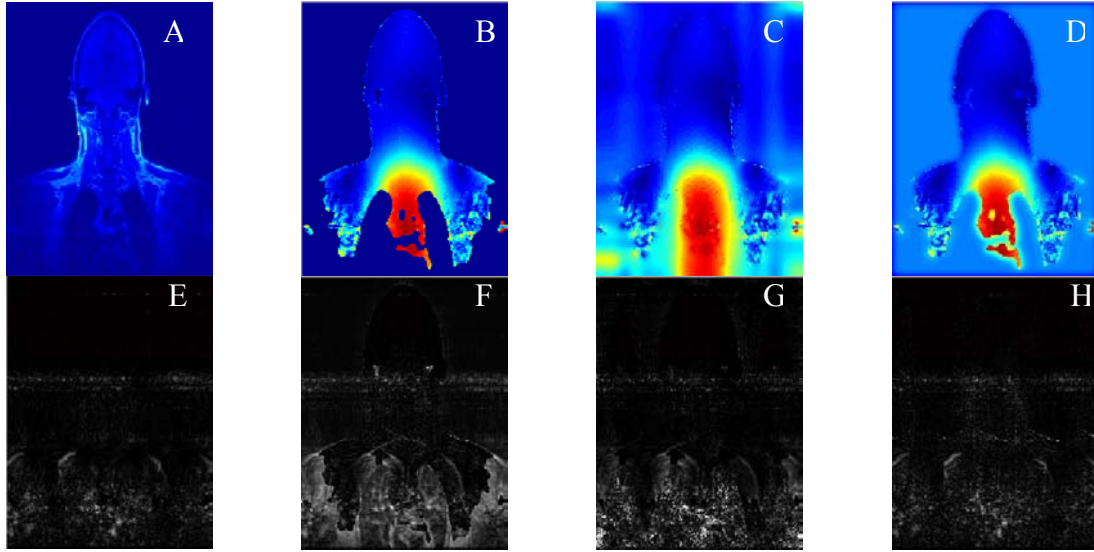


Figure 3-3. Inpainting results for neurovascular images. A) Reference Image, B) magnitude of the raw sensitivity, C) magnitude of the inpainted sensitivity map, D) magnitude of the sensitivity map by Gaussian kernel smooth, E) The intensity difference by using high resolution inpainted sensitivity map, F) The intensity difference by using raw high resolution inpainted sensitivity map, G) The intensity difference by using high resolution Gaussian Kernel smoothed sensitivity map, H) The intensity difference by using low resolution inpainted sensitivity map E) to H) use the same gray scale map

Table 3-3. Ghost ratio of neurovascular images

	R_factor = 2	R_factor = 3	R_factor = 4
Inpainted high resolution	4.21%	5.14%	6.82%
Raw high resolution	13.75%	14.40%	15.62%
GKS high resolution	5.91%	7.74%	11.28%
Inpainted low resolution	6.61%	8.36%	10.57%
Raw low resolution	15.07%	15.49%	17.10%
GKS low resolution	8.81%	9.7%	12.76%

3.3.1.4 Cardiac images

Table 4 and Table 5 show the results for Cardiac Images collected by a 1.5 T GE system (FOV 240 mm, matrix 224×192, TR 4.530 ms, TE 1.704 ms, flip angle 45°, Slice thickness 5 mm, number of averages 2) through Fast Imaging Employing Steady-State Acquisition (FIESTA) with a GE 4-channel cardiac coil. Breath-holds ranged from 10 - 20 seconds. There are 20 images per heartbeat. High-resolution sensitivity maps (for each coil) are obtained from the first image in this sequence through the use of the full K-

space. SENSE is then applied to each image in the sequence including the first by using the same sensitivity maps.

Table 3-4 shows the ghost ratios obtained by applying the high resolution sensitivity maps from the first image reconstruction to all 20 images in the same heartbeat. The R_{factor} of K-space here is 2. Note the ratios for image 1 are much lower than the others since strictly speaking the sensitivity maps are only correct for this image due to the motion of the heart during the heartbeat. Table 5 shows the results of applying low-resolution sensitivity maps obtained from each image in the series. These are generated from the 51 central rows of fully sampled k -space data [93]. The reduction factor of K-space is in this case is only 1.6232. The non-integer value is due to rows being skipped only outside the 51 row central band. Table 3-4 and 3-5 show that inpainted sensitivity maps are more accurate than both the raw sensitivity maps and GKS sensitivity maps for dynamic image.

Table 3-4. Ghost ratio of cardiac images by applying high-resolution sensitivity maps of first image

Image	Inpainted	raw	GKS
1	2.19%	9.18%	2.98%
2	11.69%	16.50%	12.04%
3	15.32%	19.43%	16.42%
4	16.10%	20.22%	17.10%
5	15.92%	19.98%	16.68%
6	15.70%	19.53%	16.76%
7	15.59%	19.40%	16.58%
8	15.39%	19.36%	16.20%
9	15.38%	19.26%	16.35%
10	15.57%	19.43%	16.60%
11	15.53%	19.42%	16.28%
12	15.33%	19.23%	16.34%
13	15.23%	19.14%	16.14%
14	15.04%	18.98%	15.80%
15	15.07%	18.92%	16.06%
16	15.08%	18.95%	15.95%
17	15.19%	19.17%	15.98%
18	15.45%	19.46%	16.47%
19	14.93%	19.06%	15.65%
20	11.83%	16.48%	12.47%
average	14.38%	18.55%	15.24%

Table 3-5. Ghost ratio of cardiac images by applying low-resolution sensitivity maps of each image

Image	Inpainted	raw	GKS
1	10.64%	17.85%	11.96%
2	11.29%	18.57%	12.25%
3	11.08%	18.34%	12.64%
4	11.16%	18.27%	12.58%
5	11.04%	17.99%	11.93%
6	10.62%	17.59%	12.00%
7	10.45%	17.23%	11.66%
8	10.56%	17.18%	11.31%
9	10.28%	17.00%	11.23%
10	10.42%	17.26%	11.62%
11	10.45%	17.25%	11.17%
12	10.37%	17.17%	11.53%
13	10.26%	17.09%	11.37%
14	10.26%	17.13%	10.97%
15	10.19%	17.26%	11.42%
16	10.11%	17.18%	11.00%
17	10.24%	17.34%	11.19%
18	10.63%	17.74%	12.06%
19	10.81%	17.85%	11.59%
20	10.69%	17.92%	11.67%
average	10.58%	17.56%	11.66%

3.3.2 Application on Intensity Correction Map

3.3.2.1 Uniformity scheme

Figure 3-4 shows the steps in the correction process described in Heels-Bergen et al. [94]. First, the multi-channel MRI raw data is duplicated to produce two data files. One data file is used to generate an image with optimized signal to noise ratio but suffering from the resultant non-uniformity. The other data file is used to generate a uniform image but with low SNR. Then each pixel of the uniform image is divided by the corresponding pixel from the high SNR image to generate a raw correction map. Inpainting is then applied to the raw correction map to generate a smooth noiseless and hole free correction map. Lastly, multiply the optimized SNR image with the correction map to generate the final image. Here the calibration of the correction map is done

through inpainting which is capable of denoising, interpolation and extrapolation all at the same time.

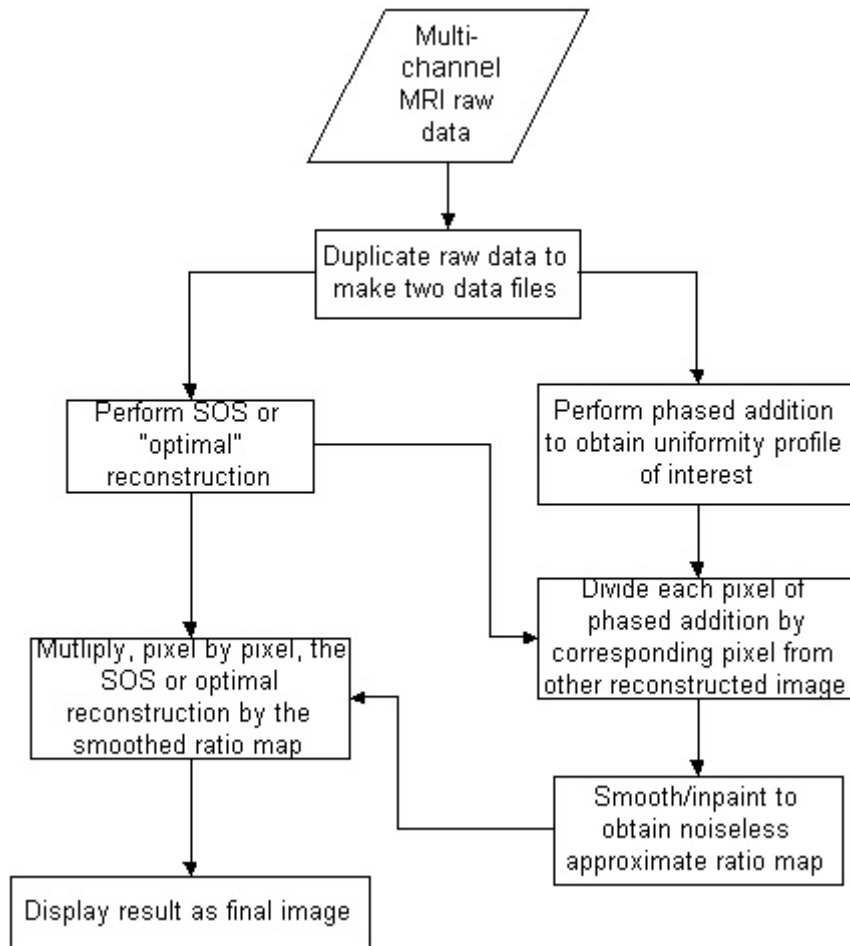


Figure 3-4. The flow chart of the intensity correction method.

In the following experiments, the “sum-of-squares” is used as the high SNR image with non-uniform intensity. The uniform references were generated by different methods to test the robustness of the proposed method (Equation 3-6). Dividing each pixel of the uniform image by corresponding pixel from the optimized SNR image can generate the raw correction map. To avoid exaggerated noise, structural and non-structural regions may be separated based upon the gradient magnitude before the division. A gradient threshold value is set at a desired gradient magnitude level. Pixels having gradient

magnitudes at or above the threshold value are considered to meet a first criterion for defining structure in the image, while pixels having gradient magnitudes lower than the threshold value are initially considered non-structure. The threshold can either be decided by gradient histogram or by operator intervention. Because the raw correction map will be smoothed and inpainted, the structural and non-structural regions do not to be separated accurately. The result will not be significantly influenced if part of structural regions is wrongly clustered. Because of the separation, some holes could be generated. The proposed model is applied to inpaint the raw correction map. The final image is generated by multiplication of the high SNR image and the correction map. The correction ratio map balances intensity across the image to produce a more uniform result. And the experiments show multiplication with a smooth ratio does not appreciably decrease signal to noise, the result image has also high SNR.

In all of those experiments, the whole intensity correction process, which includes every step described above, cost 0.5 to 0.7 seconds in together.

3.3.2.2 Phantom

Figure 3-5 shows the results for an Axis Phantom collected by a 1.5 T GE system (FOV 480 mm, matrix 256×256, TR 500 ms, TE 13.64 ms, flip angle 90°, Slice thickness 3 mm) with an 8-channel Neurovascular Array coil.. In this experiment, matlab 6.5 was used running on a PC with a 1GHz CPU and with 1G RAM. The whole intensity correction process involving each step described above, cost 0.7 seconds in CPU time. Two sets of data were collected for the same slice to calculate the signal to noise ratio in accord with the National Electrical Manufacturers Association (NEMA) standard.

Figure 3-5A shows the magnitude of the uniform image and Figure 3-5B shows the corresponding signal to noise ratio. To generate optimized signal to noise ratio image, weighted sum of squared algorithm was used with consideration of the correlation of noise between channels. Figure 3-5C shows the sum of squared image and Figure 3-5D shows the corresponding signal to noise ratio. Figure 3-5E shows the raw correction map and Figure 3-5F shows the inpainted correction map. Linear interpolation was used to get the initial guess for holes in raw correction map. Figure 3-5G is the final result image and Figure 3-5H shows the corresponding SNR. The final result is clearly uniform. And by comparison of Figure 3-5D and Figure 3-5H, it can be seen that the signal to noise ratio of the final result has no big difference with the optimized SNR. Hence the uniformity is dramatically improved and the signal to noise ratio is well protected through the proposed technique.

3.3.2.3 Clinical images

Figure 3-6 shows some intensity correction results for clinical Neurovascular Images. Those data collected by a 1.5 T GE system (FOV 440 mm, matrix 256×192, TR 1000 ms, TE 13.504 ms, flip angle 90°, Slice thickness 2 mm, number of averages 2) through the use of a fast spin echo pulse sequence with an 8-channel Neurovascular Array coil. Figure 3-6A, D and G are the sum-of-squares that are not uniform but with high SNR. Figure 3-6B, E and H are the uniform reference images that are uniform but with low SNR. Figure 3-6C, F and I are the corrected images by the proposed method. The SNRs of the uniform reference at head, neck, chest are 25.8, 23.5 and 13.5. The SNRs of the corrected image at head, neck, chest are 44.2, 39.6 and 14.5.

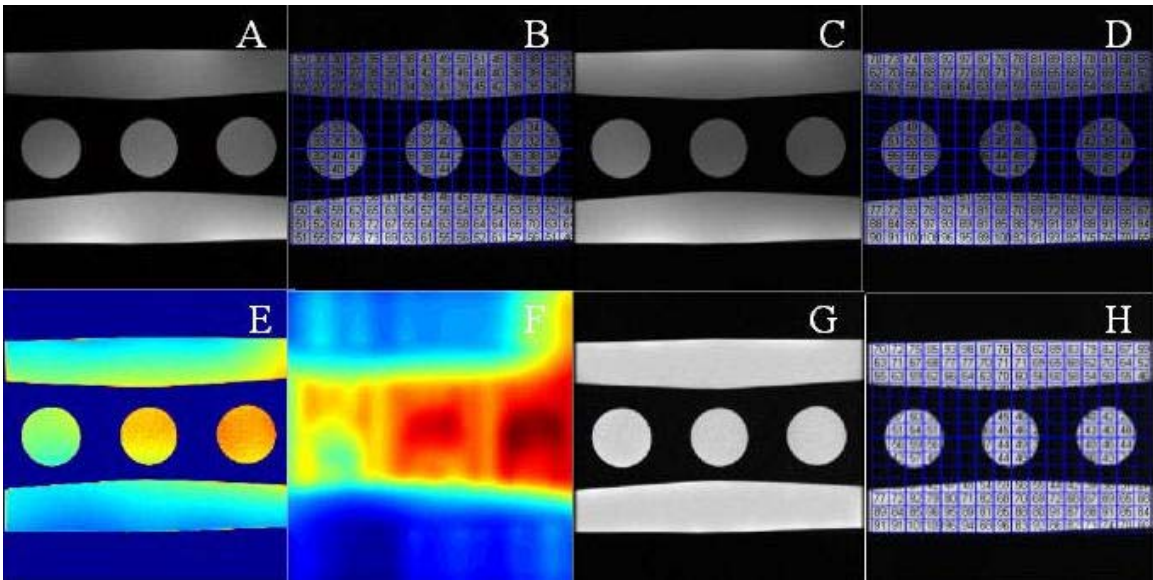


Figure 3-5. Intensity correction for phantom. A) the magnitude of the uniform reference image, B) the corresponding SNR of the reference image, C) the sum of squared image, D) the corresponding SNR of the sum-of-squares, E) the raw correction map, F) the inpainted correction map, G) the final intensity corrected image, H) SNR of the intensity corrected image

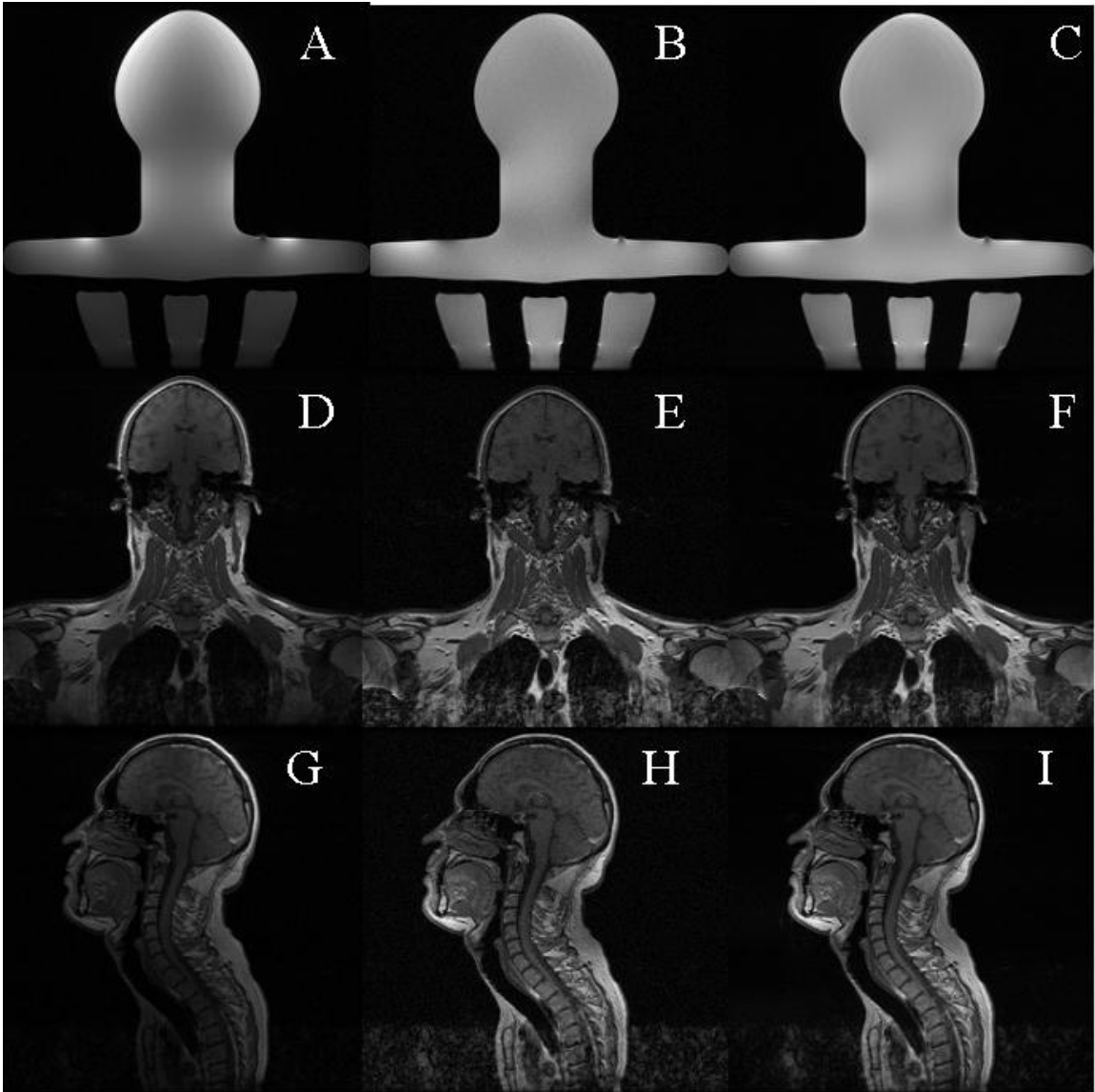


Figure 3-6. Intensity correction results for clinical Neurovascular images. A,D,G) sum of squares, B,E,H) uniform references, D,F,I) intensity corrected images by the proposed method

3.4 Conclusion

A novel inpainting model was proposed and was applied to sensitivity maps. From Figs 1 to 3, it can be concluded that all of the major issues involved in the correction of sensitivity maps are effectively and simultaneously dealt with, de-noising is accomplished, holes have been fixed and the original map has been smoothly extended to the entire image. From Tables 1 to 5 it is further concluded that inpainted sensitivity

maps produce better results than both raw sensitivity maps and GKS sensitivity maps.

The ghost ratios of the results obtained by using inpainted sensitivity maps are only 23% to 61% of the ghost ratios obtained by the use of raw sensitivity maps, and 48% to 94% of the ghost ratios obtained from using GKS sensitivity maps. The authors of [16] suggested that the “sum-of-squares” is applicable only if the object phase is sufficiently smooth so as to ensure that the corrected maps will be largely unaltered. With the application of the proposed model, this restriction becomes unnecessary since isotropic and anisotropic diffusion are effectively combined. The inpainting technique is fast. The average process time for a 256×256 image is less than 2 seconds. The proposed model functioned well for each type of image tested, phantom, neurovascular, and cardiac, and for both the high-resolution and low-resolution methods of generating sensitivity maps.

The proposed method does not need extra data for uniformity as some other methods do. By the experiments for intensity correction maps, it can be concluded that, with the use of inpainted intensity correction maps, this method is capable of correcting non-uniformity while perfectly preserving SNRs.

CHAPTER 4 MODIFIED MUMFORD-SHAH MODEL FOR MEDICAL TOMOGRAPHY

In this chapter a novel object-based variation framework for Medical Tomography problems with extremely noisy and limited data is proposed. Mumford-Shah Model by using Level Set, one of the most recent and very successful approaches in medical image processing, is introduced into the tomography field. In the method section, simultaneous tomography-segmentation Models for different cases are given. A tomography with guiding image model is also introduced. The application of a Fast Algorithm for Level Set Based Optimization onto the proposed models ends the method section. In the application section, a new non-invasive medical imaging technique-- Noise Tomography is presented. The application of the proposed method onto Noise Tomography is discussed. Experimental results and comparison with conventional methods are also reported in this section. A conclusion of the proposed framework ends this chapter.

4.1 Background of Tomography

This study is for medical tomography problem with very limited and noisy data. The problem of reconstructing physically inaccessible objects from tomographic data arises in many medical imaging applications, such as X-ray Computed Tomography (x-ray CT), Positron Emission Tomography (PET), Single Photon Emission Computed Tomography (SPECT), Electrical Impedance Tomography (EIT) and so on. The image reconstruction problem arising in those applications is commonly referred to as tomography, which is an inversion problem from a mathematical point of view. The

inverse problems that arise in these applications are typically ill-posed and require solving large dimensional estimation problem.

4.1.1 Existing Methods

To solve an ill-posed problem, a typical approach is to parameterize the region under investigation in terms of pixel values and employ regularization techniques in the reconstruction procedure to combat the ill-posedness and possible modeling errors. Tikhonov Regularization and Total Variation Method are well-known examples using this approach, which were applied in medical tomography [95, 96]. Based on the assumption that the image should be smooth, Tikhonov Regularization method adds the smooth term as the Regularization. To preserve the edges better, Total Variation Method changes the power of gradient in the smooth term from 2 to 1. Those methods work well and it can solve the noisy data problem. However, regularization methods often contain a larger number of pixels to reconstruct and result in a large dimensional estimation problem, which is time consuming. Moreover, in the cases when only extremely limited number of data are available, this type of pixel-based approaches often produces poor reconstruction.

To solve the large dimensional estimation problem in medical imaging, many successful numerical algorithms were created. Algebraic reconstruction technique (ART [97]) was the original reconstruction method used in medical imaging. The basic idea of this method is that makes an initial guess at the solution, compute projections based on the guess and then refine the guess based on the weighted difference between the actual projections and the desired projections. The method works, but is slow and susceptible to noise. With higher level of noise, the convergence is very slow, and is not guaranteed. When a full set of high signal to noise ratio (SNR) data are available, filtered back

projection (FBP) [98-100] is the most important algorithm in 2D tomography. This algorithm is essentially a numerical implementation of the Radon inversion formula. And, some simple approaches avoiding singular integrals may be used. The discrete implementation depends on the scanning geometry, i.e. the way the data is sampled. This method is widely used in 2D tomography applications. For CT, FBP is the standard reconstruction algorithm. For PET [101, 102], the reconstruction method most commonly used is also the FBP algorithm. However, this method does not work well for low SNR data.

The other class of tomography methods is statistical methods. Ordered subsets expectation maximization (OS-EM) [103, 104] and maximum a posteriori (MAP) [101, 105] are the most famous ones. Statistical methods are very successful in PET and SPECT. However, the EM-algorithm has a limitation that is sensitive to data noise. And those algorithms require that the distribution of measured data is known. Besides those methods, Layer Stripping Method is also an interesting method. This method was first described by Cheney et al. [106]. This technique is unusual in that it reconstructs images from the periphery inward. It is claimed that for EIT, this method achieves a more accurate conductivity contrast than other methods. However, no available layer-stripping algorithm works well on complete-model data. [107, 108]

Data in tomography problems can sometimes be extremely noisy and limited. In these cases the algorithms above cannot accurately solve those tomography problems. Object-based reconstruction methods provide an alternative approach. The basic idea of object-based reconstruction method is to significantly reduce the number of unknowns in a reconstruction problem by representing the object field with a low order parametric

model and then recast the original reconstruction problem into a parameter estimation problem. These parameters typically contain internal intensity values and important geometric features of target objects, such as boundaries, which are commonly used for object classification and recognition. Miller et al. [109] have proposed a reconstruction approach which uses object boundaries to describe the object shape, and a set of basis functions to represent the texture of the object as well as the background. However, Miller's method can only handle single simply-connected objects, while in practice, the ability to handle multiple objects is often required. Moreover, the position and shape of the initial curve have significant impact on the convergence speed of the solution. Later, Feng [110] used Curve Evolution Approach to overcome those drawbacks and some successful applications on CT and ground penetrating radar (GPR) were achieved. But this algorithm requires the number of different objects, which are not available in many medical imaging applications. Also, the texture of each of object is required, it is not necessary to know the basis of the texture for piecewise smooth image. Yu et al. [111] proposed an nonlocal boundary information into the regularization method for edge-preserving tomographic reconstruction. Yu et al assume the image is smooth except at the boundary of each object, and function h , which is 0 near the boundary curves and 1 otherwise, is used to control the smoothness. This model is actually same as Mumford-Shah model. The function h works in the same way as the derivative of heaviside function by Chan et al. [39]. Chan et al. [112] proposed level set and total variation regularization for inverse problems with discontinuous coefficients. Authors regularized the recovered image by the total variation norm, which indirectly controls both the jumps in the coefficient and the length of the level sets. Authors noted that in the standard level

set methodology, only the length part is regularized, which is insufficient for our purpose because we need to control the jumps as well, due to the ill-posedness of the underlying inverse problem. Another advantage of controlling the TV-norm instead of just the length of the level sets is that triple junctions are allowed to have arbitrary angles. Through the use of a novel variational multiple level set function approach borrowed from image processing, Chan et al. recover coefficients with multiple constant values associated with the discontinuous regions. If the identified image has n constant values, then we just need \log_2^n level set functions. Moreover, the exact number of constant values need not be known a priori – an upper bound suffices. If we use more level set functions than are actually needed, the redundant regions will disappear or merge with the other regions during the iterative process.

Object-based reconstruction methods provide a direction for tomography problems with noisy and limited data. And fortunately, the reconstructed images are piecewise statistical homogeneous in many applications. This property is true for most of the natural images. And sometimes, there is a reference image which can be used as guidance to generate a new image. Those statistical properties and guiding image can be used to dramatically reduce the number of unknowns. Hero et al. [113] proposed a B-spline Model to interpolate the MRI boundary and applied this boundary information to reconstruct emission computed tomography (ECT). This method solves resolution mismatch problem, which can produce severe bias due to blurring of an organ's tracer intensity across the organ boundary. This method works only for single organ case. However, we can learn from this paper that to avoid the bias caused by resolution

mismatch it is better to incorporate the MRI side information as an integral part of the image reconstruction process.

4.1.2 Motivation of the Proposed Framework

Based on the ideas above, we propose a Mumford-Shah model based framework for tomography problems with noisy and limited data. Mumford-Shah model is region based and can detect the edges that separate homogeneous regions [111]. Therefore, we propose models based on Mumford-Shah model and using statistical properties to solve tomography problems with noisy and limited data. To overcome the complicated topology, multi-phase level set method is applied here [112]. Hence this framework is named as MMSLS (Modified Mumford-Shah by Level Set). In framework, we assume there are some prior information we know about the reconstructed image, for example, smoothness of the boundary, piecewise constant/smooth/texture of the image, a guiding high-resolution image. When one or more of those prior information are available, the framework can be applied.

This work is based on the combination of [110-113]. And we extends previous approaches in a number of ways. First, this framework works for piecewise smooth image through Mumford-Shah model. The Feng et al. [110] model need prior information of the texture basis which is not required in this model. The Chan et al. [112] model is based on total variation and the diffusion is anisotropic. We prefer the Mumford-Shad model because of the computation efficiency. One may argue that the computation for curve length term in Mumford-Shad model is time consuming, but some new techniques [43, 114, 115] for segmentation can be applied here to dramatically reduce the computation complexity. One may also argue that the anisotropic diffusion may be better than the isotopic diffusion in Mumford-Shad model. But for most of the medical images,

in the segmentation boundary, the image is isotropically smooth. In case the image is piecewise constant, the proposed framework is same as the models in Chan et al. [112] and Feng et al. [110]. The application of new numerical techniques in Chan [114] for segmentation is the second extension of this work. Because of application of the multi-phase level set, which is originally used for segmentation in Chan and Vese [50], the proposed framework requires \log_2^n level set when there are n different objects, which is much less than n level sets required in [110]. The application of fast sweeping method in [114] for Mumford-Shah image segmentation dramatically reduces the computation complexity. Third, not like in Hero et al. [113], when we incorporate the MRI side information as an integral part of reconstruction, there could be more than one object in the MR guiding image. The reason is the level set can take care of complex topology.

4.2 Proposed Model

4.2.1 Description of the Proposed Model

In the object-based tomography problem of our interest, we want to determine the position and shape of the object according to measured data. A region based level set approach is adopted here and energy functional is developed to attract the zero level set to the object boundary:

$$E(f, \Gamma) = \sum_i \left\| \int_{\Omega} R_i(x) f(x) dx - M_i \right\|_2^2 + \lambda_1 \int_{\Omega \setminus \Gamma} |\nabla f|^2 dx + \lambda_2 H^1(\Gamma) \quad (4-1)$$

Where λ_1 and λ_2 are parameters to balance those 3 terms, i is for different measurement. The first term is the fidelity term. As a tomography problem, the reconstructed function $f(x)$ should satisfy $M_i = \int_{\Omega} R_i(x) f(x) dx, i = 1, 2, \dots, n$. Because most of the natural images are smooth in each object, the second term is to make sure the

reconstructed image $f(x)$ is piecewise smooth. The last term is to smooth object edges, since most of the natural objects have smooth edges. H^1 is the one dimensional Hausdorff measure, which generalizes the length notion for regular curves. This term penalize the length of the boundary and hence smooth the boundary. This model is actually a Mumford-shad model based implementation of formula (4)-(6) in Yu and Fessler [111]. Equation 4-1 gives a simpler numerical method than the Yu and Fessler model [111]

4.2.2 Level Set Forms in Different Cases

In this part, several cases of the image are considered. Specific models and corresponding Euler-Lagrange Equations are given. Several numerical issues are also discussed.

4.2.2.1 Binary field model

Assume that there are only two intensities in an image, i.e. several homogeneous objects with same unknown constant intensity x are scattered in a homogeneous background with intensity y . Prior knowledge of number of objects is not required, and the background does not have to be continuous.

Since now the function f is a two-value function, the smooth term is no longer needed. Level set function ϕ is applied here to implement the Hausdorff measure H^1 [41].

Let

$$\begin{cases} \phi(x) > 0, & x \in w \\ \phi(x) < 0, & x \in I \setminus w \\ \phi(x) = 0, & x \in \partial w \end{cases}$$

where w is the set of regions with value x . Then the energy functional is

$$E(x, y, \phi) = \sum_i \left\| x^* \int_{\Omega} R_i H(\phi) dp + y^* \int_{\Omega} R_i (1 - H(\phi)) dp - M_i \right\|_2^2 + \lambda \int_{\Omega} |\nabla H(\phi)| dp \quad (4-2)$$

where H is the Heaviside function $H = \begin{cases} 1, & z \geq 0 \\ 0, & z < 0 \end{cases}$

and the solution of f is $f(z) = \begin{cases} x, & \phi \geq 0 \\ y, & \phi < 0 \end{cases}$.

Let $F_i = \sum_i \int_{\Omega} R_i H(\phi) dp$ and $G_i = \sum_i \int_{\Omega} R_i (1 - H(\phi)) dp$, notice

$\int_{\Omega} |\nabla H(\phi)| = \int_{\Omega} \delta(\phi) |\nabla \phi|$, where $\delta(z) = \frac{d}{dz} H(z)$ in the sense of distributions then the Euler-

Lagrange Equations are

$$\frac{d\phi}{dt} = -\sum_i \left((xF_i + yG_i - M_i) * R_i - \lambda \operatorname{div} \frac{\nabla \phi}{|\nabla \phi|} \right) \delta_{\varepsilon}(\phi)$$

$$\frac{dx}{dt} = -\sum_i F_i (xF_i + yG_i - M_i)$$

$$\frac{dy}{dt} = \sum_i G_i (xF_i + yG_i - M_i)$$

where $\delta_{\varepsilon} = H'_{\varepsilon}, \varepsilon \rightarrow 0$

4.2.2.2 Piecewise constant model

This model is for the case that there are several homogeneous regions (phases) with different constant value of X_i in the image and the maximum possible number \mathbf{n} of phases is given.

Since now the function f is piecewise constant, the smooth term is no longer needed. For n phases, $m = \log n$ level set functions $\phi_i : \Omega \rightarrow R$ are needed. The union of the zero-level sets of ϕ_i will represent the edges in the segmented image. The “vector

level set function” $\Phi = (\phi_1, \dots, \phi_m)$ and the “vector Heaviside function”

$H(\Phi) = (H(\phi_1), \dots, H(\phi_m))$, whose components are only 1 or 0, are applied to define the segments or phases in the domain Ω in the following way: two pixels (x_1, y_1) and (x_2, y_2) in Ω will belong to the same phase or class, if and only if

$H(\Phi(x_1, y_1)) = H(\Phi(x_2, y_2))$. In other words, the classes or phases are given by the level sets of the function $H(\Phi)$, i.e. one class is formed by the set

$\{(x, y) | H(\Phi(x, y)) = \text{constant_vector} \in H(\Phi(\Omega))\}$, (one phase or class contains those pixels (x, y) of Ω having the same value $H(\Phi(x, y))$). Characteristic function χ_i and constant values X_i can be defined as the followed sample.

In case, there are 9 phases, then 3 level sets are needed to describe it. And use χ_{ijk} and X_{ijk} to denote χ_i and X_i , i is for ϕ_1 , j is for ϕ_2 , k is for ϕ_3 . i, j, k can only be either 0 or 1, 1 means H, 0 means 1-H. e.g.

$$\chi_{111} = H(\phi_1)H(\phi_2)H(\phi_3)$$

$$\chi_{011} = (1 - H(\phi_1))H(\phi_2)H(\phi_3).$$

Correspondingly

X_{111} is the conductivity of area $\phi_1 > 0, \phi_2 > 0, \phi_3 > 0$

X_{011} is the conductivity of area $\phi_1 < 0, \phi_2 > 0, \phi_3 > 0$.

Then the energy functional is

$$E(X_i, \chi_i) = \sum_l \sum_{1 \leq l \leq n = 2^m} \left\| X_l * \int_{\Omega} R_l \chi_l dp - M_l \right\|_2^2 + \lambda \sum_{1 \leq i \leq m} \int_{\Omega} |\nabla H_{\epsilon}(\phi_i)| dp$$

And the solution of f is $f(z) = X_i, z \in \chi_i$

In case, there are 4 phases, the energy functional is

$$\begin{aligned}
E(X_I, \chi_I) &= \\
&= \sum_i \left\| X_{11} \int_{\Omega} R_i H(\phi_1) H(\phi_2) dx dy + X_{10} \int_{\Omega} R_i H(\phi_1) (1 - H(\phi_2)) dx dy \right. \\
&X_{01} \int_{\Omega} R_i (1 - H(\phi_1)) H(\phi_2) dx dy + X_{00} \int_{\Omega} R_i (1 - H(\phi_1)) (1 - H(\phi_2)) dx dy - M_i \Big\|_2^2 \quad (4-3) \\
&+ \lambda \int_{\Omega} |\nabla H(\phi_1)| + \lambda \int_{\Omega} |\nabla H(\phi_2)|
\end{aligned}$$

The following is one numerical method for Equation 4-3.

Define

$$\begin{aligned}
T_{11} &= \sum_i \int_{\Omega} R_i H(\phi_1) H(\phi_2) dx dy, \\
T_{10} &= \sum_i \int_{\Omega} R_i H(\phi_1) (1 - H(\phi_2)) dx dy, \\
T_{01} &= \sum_i \int_{\Omega} R_i (1 - H(\phi_1)) H(\phi_2) dx dy, \\
T_{00} &= \sum_i \int_{\Omega} R_i (1 - H(\phi_1)) (1 - H(\phi_2)) dx dy, \\
DIF &= \sum_{i,j} X_{ij} T_{ij} - \sum_i M_i
\end{aligned}$$

then Euler-Lagrange Equations are

$$\begin{aligned}
\frac{\partial \phi_1}{\partial t} &= \delta_{\varepsilon}(\phi_1) \left\{ \lambda_1 \operatorname{div} \left(\frac{\nabla \phi_1}{|\nabla \phi_1|} \right) - DIF \right. \\
&\left. \left(\sum_i R_i ((X_{11} - X_{01}) H(\phi_2) + (X_{10} - X_{00}) (1 - H(\phi_2))) \right) \right\}
\end{aligned}$$

Similarly,

$$\begin{aligned}
\frac{\partial \phi_2}{\partial t} &= \delta_{\varepsilon}(\phi_2) \left\{ \lambda_1 \operatorname{div} \left(\frac{\nabla \phi_2}{|\nabla \phi_2|} \right) - DIF \right. \\
&\left. \left(\sum_i R_i ((X_{11} - X_{10}) H(\phi_1) + (X_{01} - X_{00}) (1 - H(\phi_1))) \right) \right\}
\end{aligned}$$

For X_{11}

$$X_{11} T_{11} + X_{10} T_{10} + X_{01} T_{01} + X_{00} T_{00} - \bar{M} T_{11}^T = 0$$

Similar formulas for X_{10}, X_{01}, X_{00}

Hence

$$\begin{pmatrix} T_{11}^T T_{11} & T_{11}^T T_{10} & T_{11}^T T_{01} & T_{11}^T T_{00} \\ T_{10}^T T_{11} & T_{10}^T T_{10} & T_{10}^T T_{01} & T_{10}^T T_{00} \\ T_{01}^T T_{11} & T_{01}^T T_{10} & T_{01}^T T_{01} & T_{01}^T T_{00} \\ T_{00}^T T_{11} & T_{00}^T T_{10} & T_{00}^T T_{01} & T_{00}^T T_{00} \end{pmatrix} \begin{pmatrix} X_{11} \\ X_{10} \\ X_{01} \\ X_{00} \end{pmatrix} = \begin{pmatrix} T_{11}^T \bar{M} \\ T_{10}^T \bar{M} \\ T_{01}^T \bar{M} \\ T_{00}^T \bar{M} \end{pmatrix}$$

4.2.2.3 Piecewise texture model

In some cases, the intensity of each object is not constant but follows certain texture, i.e. the intensity function of object I is $f_I(x) = \sum_j \alpha_I^j B_I^j(x)$, where $B_I^j(x)$ provide the basis for describing the object I texture [109, 116, 117], and α_I^j are the corresponding expansion coefficients for the object I. Suppose the texture basis $B_I^j(x)$ for those objects are known and the upper bound of the number of objects is also known, then the energy functional is

$$E(\alpha_I^j, \chi_I) = \sum_I \sum_{1 \leq I \leq n = 2^m} \left\| \int_{\Omega} R_I \chi_I \sum_j \alpha_I^j B_I^j(x) dp - M_I \right\|_2^2 + \lambda \sum_{1 \leq i \leq m} \int_{\Omega} |\nabla H_\varepsilon(\phi_i)| dp \quad (4-4)$$

Now, the unknowns are the coefficients of those bases. And the solution of f is

$$f(z) = \sum_j \alpha_I^j B_I^j(z) \quad z \in \chi_I$$

4.2.2.4 General piecewise smooth model

In case no prior information about number of objects and no prior information about intensity, the problem can be solved using only two level set functions. The idea of two-level set is from Vese and Chan [41]. They successfully applied multiphase level set to solve segmentation problem. Because there is no prior information available, the advantage of reducing unknowns from number of pixels to number of parameters is lost. However, because of the isotropic diffusion, it is still better than total variation method

on speed. Furthermore, this model can do segmentation and reconstruction simultaneously.

Define function

$$f = \begin{cases} f^{++}, \phi_1 > 0 \text{ and } \phi_2 > 0 \\ f^{+-}, \phi_1 > 0 \text{ and } \phi_2 < 0 \\ f^{-+}, \phi_1 < 0 \text{ and } \phi_2 > 0 \\ f^{--}, \phi_1 < 0 \text{ and } \phi_2 < 0 \end{cases}$$

Using the Heaviside function, the relation between f and the level set functions can be expressed by

$$f = f^{++}H(\phi_1)H(\phi_2) + f^{+-}H(\phi_1)(1-H(\phi_2)) + f^{-+}(1-H(\phi_1))H(\phi_2) + f^{--}(1-H(\phi_1))(1-H(\phi_2))$$

Then the energy functional is

$$\begin{aligned} E(u, \phi_1, \phi_2) = & \\ = & \sum_i \left\| \int_{\Omega} R_i f^{++} H(\phi_1) H(\phi_2) dx dy + \int_{\Omega} R_i f^{+-} H(\phi_1) (1 - H(\phi_2)) dx dy \right. \\ & \left. \int_{\Omega} R_i f^{-+} (1 - H(\phi_1)) H(\phi_2) dx dy + \int_{\Omega} R_i f^{--} (1 - H(\phi_1)) (1 - H(\phi_2)) dx dy - M_i \right\|_2^2 \quad (4-5) \\ & + \lambda_1 \int_{\Omega} |\nabla u^{++}|^2 H(\phi_1) H(\phi_2) dx dy + \lambda_1 \int_{\Omega} |\nabla u^{+-}|^2 H(\phi_1) (1 - H(\phi_2)) dx dy \\ & + \lambda_1 \int_{\Omega} |\nabla u^{-+}|^2 (1 - H(\phi_1)) H(\phi_2) dx dy + \lambda_1 \int_{\Omega} |\nabla u^{--}|^2 (1 - H(\phi_1)) (1 - H(\phi_2)) dx dy \\ & + \lambda_2 \int_{\Omega} |\nabla H(\phi_1)| + \lambda_2 \int_{\Omega} |\nabla H(\phi_2)| \end{aligned}$$

And define

$$\begin{aligned} DIF = & \sum_i \int_{\Omega} R_i u^{++} H(\phi_1) H(\phi_2) dx dy + \sum_i \int_{\Omega} R_i u^{+-} H(\phi_1) (1 - H(\phi_2)) dx dy \\ & + \sum_i \int_{\Omega} R_i u^{-+} (1 - H(\phi_1)) H(\phi_2) dx dy + \sum_i \int_{\Omega} R_i u^{--} (1 - H(\phi_1)) (1 - H(\phi_2)) dx dy - (\bar{M} + EM) \end{aligned}$$

We deduce the Euler-Lagrange equations for u^{++}

$$\sum_i R_i \cdot DIF_i^{++} = \lambda_1 \Delta u^{++} \text{ in } \{\phi_1 > 0, \phi_2 > 0\}, \frac{\partial u^{++}}{\partial n} = 0 \text{ on } \{\phi_1 = 0, \phi_2 \geq 0\} \text{ and } \{\phi_1 \geq 0, \phi_2 = 0\}$$

where

$$DIF_i^{++} = \int_{\Omega} R_i u^{++} dx dy - M_i$$

Similarly we have the Euler-Lagrange equations for u^{++}, u^{-+}, u^{--}

$$\sum_i R_i \cdot DIF_i^{++} = \lambda_1 \Delta u^{++} \text{ in } \{\phi_1 > 0, \phi_2 < 0\}, \frac{\partial u^{++}}{\partial n} = 0 \text{ on } \{\phi_1 = 0, \phi_2 \leq 0\} \text{ and } \{\phi_1 \geq 0, \phi_2 = 0\}$$

$$\sum_i R_i \cdot DIF_i^{-+} = \lambda_1 \Delta u^{-+} \text{ in } \{\phi_1 < 0, \phi_2 > 0\}, \frac{\partial u^{-+}}{\partial n} = 0 \text{ on } \{\phi_1 = 0, \phi_2 \geq 0\} \text{ and } \{\phi_1 \leq 0, \phi_2 = 0\}$$

$$\sum_i R_i \cdot DIF_i^{--} = \lambda_1 \Delta u^{--} \text{ in } \{\phi_1 < 0, \phi_2 < 0\}, \frac{\partial u^{--}}{\partial n} = 0 \text{ on } \{\phi_1 = 0, \phi_2 \leq 0\} \text{ and } \{\phi_1 \leq 0, \phi_2 = 0\}$$

the Euler-Lagrange equations for ϕ_1 and ϕ_2

$$\begin{aligned} \frac{\partial \phi_1}{\partial t} = & -\frac{\partial E(\phi_1 + \varepsilon v)}{\partial \varepsilon} = \delta_{\varepsilon}(\phi_1) \left\{ \lambda_2 \operatorname{div} \left(\frac{\nabla \phi_1}{|\nabla \phi_1|} \right) - \left(\sum_i R_i u^{++} \cdot DIF_i + \lambda_1 |\nabla u^{++}|^2 \right) H(\phi_2) - \right. \\ & - \left(\sum_i R_i u^{-+} \cdot DIF_i + \lambda_1 |\nabla u^{-+}|^2 \right) (1 - H(\phi_2)) + \left(\sum_i R_i u^{--} \cdot DIF_i + \lambda_1 |\nabla u^{--}|^2 \right) H(\phi_2) + \\ & \left. + \left(\sum_i R_i u^{--} \cdot DIF_i + \lambda_1 |\nabla u^{--}|^2 \right) (1 - H(\phi_2)) \right\} \end{aligned}$$

Similarly

$$\begin{aligned} \frac{\partial \phi_2}{\partial t} = & \delta_{\varepsilon}(\phi_2) \left\{ \lambda_2 \operatorname{div} \left(\frac{\nabla \phi_2}{|\nabla \phi_2|} \right) - \left(\sum_i R_i u^{++} \cdot DIF_i + \lambda_1 |\nabla u^{++}|^2 \right) H(\phi_1) + \right. \\ & + \left(\sum_i R_i u^{-+} \cdot DIF_i + \lambda_1 |\nabla u^{-+}|^2 \right) H(\phi_1) - \left(\sum_i R_i u^{-+} \cdot DIF_i + \lambda_1 |\nabla u^{-+}|^2 \right) (1 - H(\phi_1)) + \\ & \left. + \left(\sum_i R_i u^{--} \cdot DIF_i + \lambda_1 |\nabla u^{--}|^2 \right) (1 - H(\phi_1)) \right\} \end{aligned}$$

4.2.2.5 Model for tomography with guiding image

In some medical imaging applications, image of one physical property is given and the image of another physical property is wanted. For example, the MRI guided Noise Tomography (MR-NT). In MR-NT the MR image, which is the map of proton density, is

given, and the map of conductivity is wanted. In this case, geometry information, like shape and position, of each phase can be achieved by segmenting the given guiding image. Then using that information to compute wanted value for each object. If we do segmentation and reconstruction separately, resolution mismatch may occur. This can produce severe bias due to blurring of an organ's tracer intensity across the organ boundary. The proposed model below combines segmentation and reconstruction together and it is beneficial to both segmentation the given image and reconstruction for the new image with noisy and limited data.

Denote

u – given guiding image

u_I – the segmented guiding image for class I

Parameters λ_1, λ_2 - trade off between terms

Other notations are same as above. By assuming the wanted value is piecewise constant and there are at most n phases, then the energy functional is

$$E(X_I, \chi_I, u_I) = \sum_{l,i} \left\| \sum_{1 \leq l \leq n=2^m} X_I * \int_{\Omega} R_l \chi_I dA - M_i \right\|_2^2 + \lambda_1 \sum_{1 \leq l \leq m} \int_{\Omega} |\nabla H(\phi_l)| + \lambda_2 \sum_{1 \leq l \leq n=2^m} \int_{\Omega} |u - u_I|^2 \chi_I dx dy \quad (4-6)$$

And the solution of f is $f(z) = X_i, \quad z \in \chi_i$

The first term is still the fidelity term, this term is mainly for reconstruction. The second term penalize the length of the boundary. This term works for both segmentation and reconstruction. The third term is for segmentation. This term is borrowed from [39], which is for Mumford-Shad model based segmentation. Here we assume the guing image is also piecewise constant. This model solves the tomography problem with guiding

images. It is also simultaneously capable of not only segmentation for both guiding and reconstructed images but also denoising the guiding image.

4.3 Application on Noise Tomography

4.3.1 Introduction of Noise Tomography

Noise Tomography, which aims to determine the distribution of the conductivity in the sample, is a new non-invasive medical imaging technique invented by MRI Devices Cooperation. The NT technique is designed to use the correlations in the detected electronic thermal noise in an RF probe array and the relationship between conductivity and the noise power coupled between the sample and probe to measure the electrical conductivity distribution within the sample. Many applications of conductivity distribution in diagnostic imaging have been documented. For example, gastrointestinal and oesophageal function [4, 5], hyper- or hypothermic treatment of malignant tumors [6, 7], imaging of the head [8, 9, 118], pulmonary function [10], cancer detection [11, 12, 119], measurements of cardiac output and investigation to locate the focus of epileptic seizures [13].

4.3.2 Electronic Noise

Historically, the electronic thermal noise generated within the sample has not been encoded during the Magnetic Resonance Imaging (MRI) process. The pulse sequences and gradient encoding do not encode the noise but the new methods of partially parallel imaging (SENSE, SMASH, etc., [16] [15]) demonstrate that the probe sensitivity patterns are encoding functions for the MRI signal. The sensitivity patterns also encode the noise to approximately the same extent as they encode the signal. This is true because the electronic thermal noise of the tissue is normally dominant and the physical size and structure of the coil dictate the acquisition site of the 'body' noise. Although the regions

of MRI signal acquisition and noise acquisition are similar they are not the same, because the probe's magnetic field is associated with MRI signal acquisition whereas the probe's electric field is associated with noise acquisition. If several probes and receiver channels are used in MRI signal acquisition, the noise in a given channel can be assumed to be significantly localized by the electric field profile of the probe associated with that channel. This is a critical concept because it indicates that noise can have an associated information content. The association exists because the noise originates in tissues of the body and is acquired in a predictable and repeatable way by means of a local probe.

The NT technique refines existing technology by measuring only the covariance of noise within a multiple receiver system. This is important because, in principle, the amount of non-sample noise is largely irrelevant since correlating the two noise outputs eliminates the uncorrelated noise by averaging.

To determine the distribution of the conductivity in the sample, the NT technique uses the non-resonant electronic thermal noise of the tissue sample, detected by an array of RF probes, and the known, or calculated overlap of the electromagnet fields of those probes. Electronic thermal noise is a basic property of all matter and has been well characterized in both one-dimensional (Johnson/Nyquist) and three-dimensional (Black Body Radiation) cases. This NT technique is based on a combination of the fluctuation dissipation theorem and the principle of reciprocity. The objective of the NT technique is to use the noise correlation between the different channels in an array of RF probes to plot the conductivity distribution within the sample.

When an oscillating RF probe is placed near a conducting sample, energy in the probe is dissipated in the sample and the impedance of the probe is changed. This change

in impedance is a function of the internal impedance of the probe and of the coupling between the sample and the probe. Thevenin's theorem shows that the thermal noise power detected across a circuit is proportional to the equivalent resistance of the circuit. Therefore, if an RF probe is moved with respect to the sample and the resulting change in noise power is measured, the change in coupling between the sample and the coil may be determined. A similar effect on the impedance of the circuit and the detected noise power will occur if the probe is kept in a fixed location and the conductivity of the sample changed.

Utilizing these principals, a one-dimensional conductivity map of the sample may be constructed by simply moving the probe at a fixed distance from the surface of the sample and measuring the changes in the sample noise. Adding an array of coils, which are measured in parallel, will increase the sampling rate and therefore the imaging rate. This arrangement, however, will determine only one piece of information per coil position. In order to determine n independent parameters about the sample, a minimum of n independent coil positions must be measured.

4.3.3 Intercoil Noise Correlation

In order to increase the sample information obtained from any given probe position and to reduce the effects of non-sample noise sources, the noise correlation between different coils in an array of coils will be measured. Using the normalized noise covariance will provide up to $n(n-1)/2$ different pieces of sample information from each position of the coil array and will reduce the effects of non-sample related detector noise sources. The noise correlation between channels is proportional to:

$$\int \sigma(\vec{r}) \vec{E}_j(\vec{r}) \cdot \vec{E}_k(\vec{r}) dV$$

Where E_i, E_k are the electric field resulting from the two probes at the point r in space and $\sigma(r)$ is the conductivity at the point r in space.

4.3.4 Relation with Tomography Models

For this Noise Tomography problem, this distribution of conductivity is wanted. Hence σ is the unknown function. The noise correlation

$$M_{jk} = \int \sigma(\vec{r}) \vec{E}_j(\vec{r}) \cdot \vec{E}_k(\vec{r}) dV$$

generated by coil i and coil j is the collected data, $R_{jk}(\vec{r}) = \vec{E}_j(\vec{r}) \cdot \vec{E}_k(\vec{r})$ is the fixed function determined by the character of the machine.

The goal here is to find conductivity map σ with given M_{jk} and R_{jk} .

4.3.5 Experiments and Results

All programs were produced by using Matlab, and ran on a Compaq PC with 1GHz CPU speed.

4.3.5.1 Experiment in one dimension

The phantom sample is a disc with a diameter of 16 cm and a width 5 cm.

Figure 4-1 shows the result of the experiment using MMSLS without using any prior information. The red curve shows where the phantom disc actually is, and the blue curve shows the result by using the MMSLS to binary field model. The unit of x-axis is the centimeter. By using the real position and disc width, the ideal norm of RX-M is calculated as 28.2831. The resulting norm, using MMSLS, is 33.6771. The CPU time for this reconstruction was 6.875 seconds.

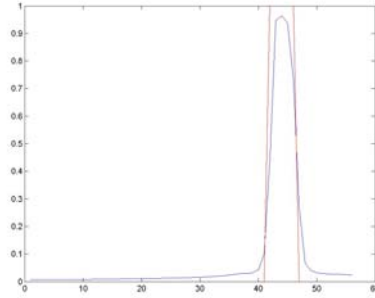


Figure 4-1. Experiment result in 1 dimension

4.3.5.2 Experiment in two dimensions

In this experiment, there are only 231 equations with which to reconstruct the image. But to achieve resolution of $2\text{mm}\times 2\text{mm}$, 10000 unknowns need to be solved. Furthermore, the measured data itself is very noisy because the data is noise correlation. Therefore this inverse problem is extremely ill posed. Figure 4-2 shows the experiment result. Figure 4-2A is the MR image of the phantom. The phantom is constructed of a 197mm (7.75") ID by 180mm long acrylic tube that is filled with a solution of Cu_2SO_4 (2.0 grams/Liter) and NaCl (4.5 grams/Liter). The conductivity of this solution is on the order of 0.8S/m. There are three smaller acrylic tubes, each of which is 180mm long, contained within the 197mm OD tube. Figure 4-2B shows the photo of the phantom. If the container is ignored, the digitized real image should look like the image in Figure 4-2C. Figure 4-2D is the result by using MMSLS to binary field model. The reconstructed image has a resolution of $1.97\text{mm}\times 1.97\text{mm}$. The CPU time is 25 seconds. The solved relative conductivity of saline solution and water is 1.0 and 0.2, respectively. The black dots (around the periphery of the blue area) are the result of automatic segmentation. If it is assumed that the relative conductivity of distilled water is 0, and the relative conductivity of saline solution is 1, then the norm of RX-M is $1.9712\text{e-}006$. To compare the result of MMSLS and traditional algorithms, Figure 4-2E and 4-2F show the

result by using pixel-wise method Total Variation and ART. The reconstructed image (Figure 3-6) by Total Variation Method has a resolution of 3.97mm×3.97mm. The CPU time is 189 seconds. The reconstructed image (Figure 4-2F) by ART has a resolution of 14.1mm*14.1mm. The CPU time is 32 seconds.

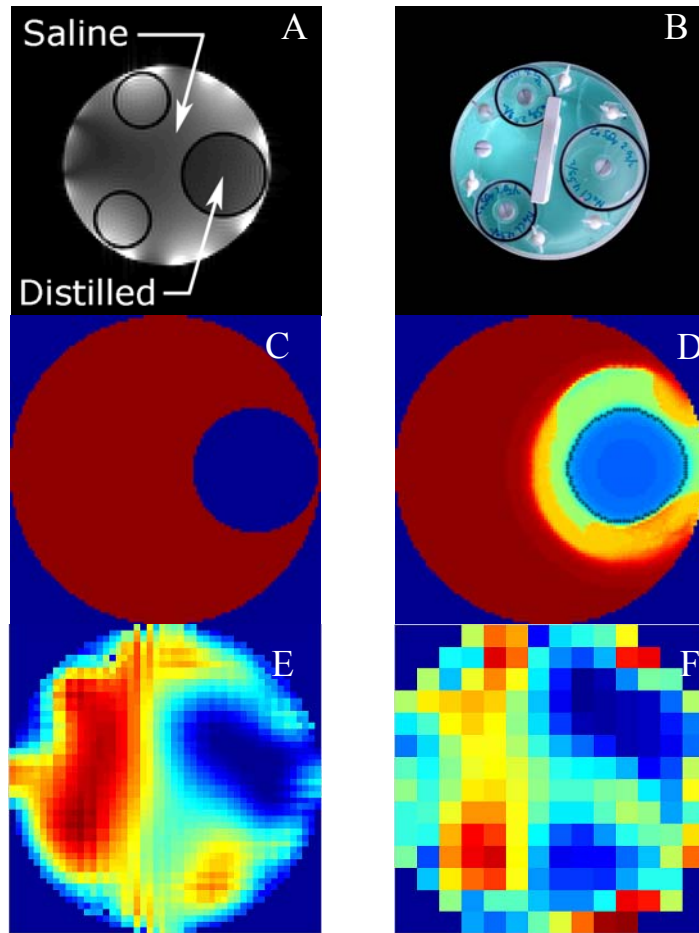


Figure 4-2. Experiment result in 2 dimensions. A) MRI Image of Phantom, B) NT Phantom Photo, C) Digitized NT Phantom, D) Reconstructed image by MMSLS, E) Reconstructed image by Total Variation, F) Reconstructed image by ART

In this experiment, the model for Total Variation algorithm is

$$E(f) = \sum_l \left\| \int_{\Omega} R_l(x) f(x) dx - M_l \right\|_2^2 + \int_{\Omega} |\nabla f(x)| dx, \text{ subject to } ub \geq f(x) \geq lb$$

where ub and lb are the upper bound and least bound of $f(x)$ and are given as prior information. And the method introduced in [97] is applied for the ART algorithm.

4.3.5.3 Experiment in two dimensions with guiding image

In this experiment MR image is used as the guiding image and tried to generate more accurate conductivity map with the same tomography data in the previous experiment. The model for tomography with guiding image is applied in this experiment. Because there are 3 kinds of objects: Cu_2SO_4 , $NaCl$, and containers, 2 level sets are used to describe the geometry properties of those 3 objects.

Figures 4-3 display the results based on the ideal guiding image. Figure 4-3A is the ideal guiding Image. Figure 4-3B through D is the segmentation results of the ideal guiding Image according to vector level set function defined in 2.3.2. Figure 4-3E is the reconstructed conductivity distribution map. The solved relative conductivity of saline solution, water and plastic is 1.0000, 0.2805 and 0.0399.

Figures 4-4 display the results based on the real MR image of the phantom. Figure 4-4A is the real MR Image. Figure 4-4B to 4-4D is segmentation result based on the real MR Image. Figure 4-4E is the reconstructed conductivity distribution map. The solved relative conductivity of saline solution, water and plastic is 1.0000, 0.1873 and 0.1230.

With the same tomography and an extra guiding image, the result 4-4 E is much better than 4-2 D. Furthermore, even though the MR image used here is very non-uniform, but the MMSLS to Tomography with guiding image model still can segment it accurately. It can be seen that this model can not only make the reconstruction better with the guiding image but also can segment the guiding image better with the tomography data.

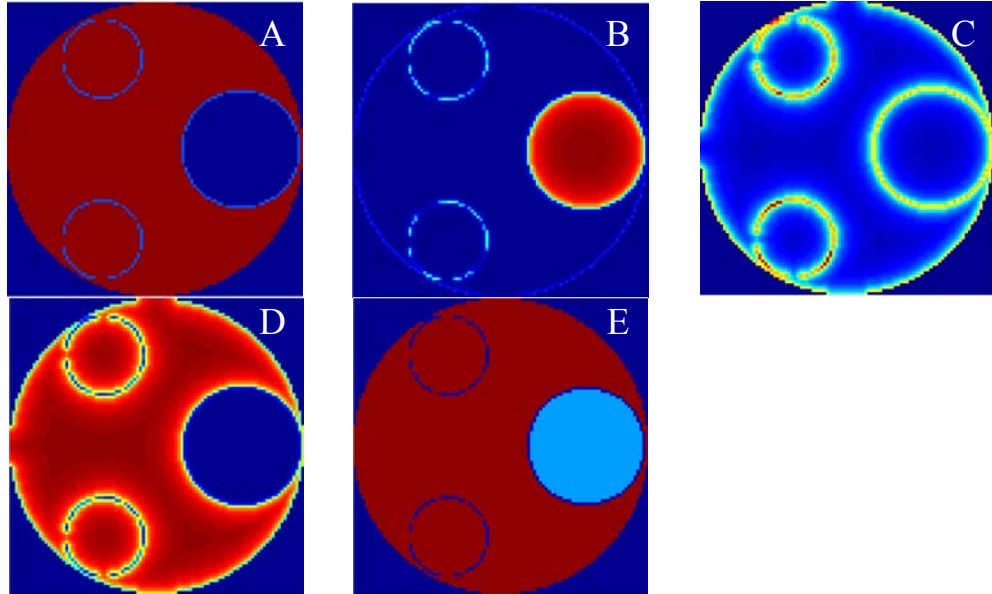


Figure 4-3. Experiment result in 2 dimensions with ideal guiding image. A) Ideal MR Image, B) Segmented Object 1, C) Segmented Object 2, D) Segmented Object 3, E) Reconstructed conductivity distribution map

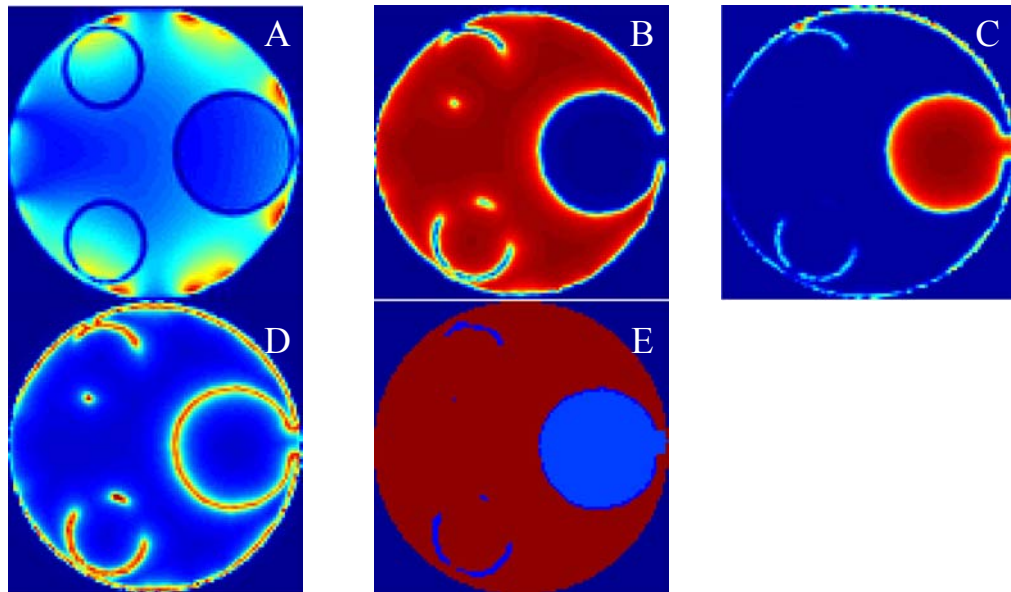


Figure 4-4. Experiment result in 2 dimensions with real MR guiding image. A) real MR Image, B) Segmented Object 1, C) Segmented Object 2, D) Segmented Object 3, E) Reconstructed conductivity distribution map

4.3.5.4 Experiment in two dimensions with guiding image by fast sweeping

In this experiment, the fast algorithm for Level Set Based Optimization [43] is applied to MMSLS binary field model. The computation time is significantly reduced.

And the reconstruction result is accurate.

Figure 4-5 shows the result by using ideal guiding image. The CPU time is 2.047 seconds. The solved relative conductivity of saline solution, water & plastic (water and plastic can not distinguished by binary field model) is 0.918, 0.289.

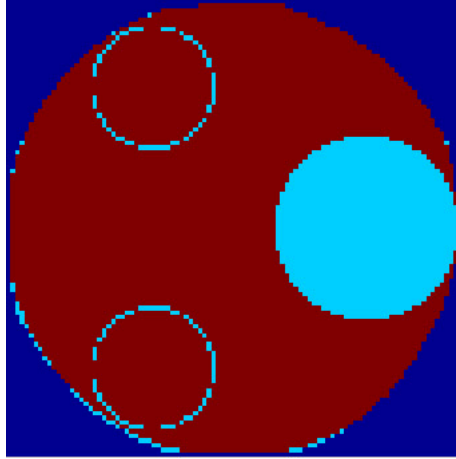


Figure 4-5. Reconstructed image by fast sweeping

4.4 Conclusion

A novel algorithm MMSLS for Tomography problem with extremely noisy and limited data is introduced. This algorithm is flexible. It can be used for any geometry with or without prior information. It is very easy to change the model for different cases. Furthermore, this approach has no special requirements. Hence it may be easily applied to a variety of Tomography problems.

The MMSLS algorithm has proven itself to provide accurate results. The reconstructed image by MMSLS has higher resolution and better visualization than conventional method. And the object property (relative conductivity in our experiments) is also accurately calculated.

Because the MMSLS algorithm is object based, not pixel-based, this approach, for an equivalent output resolution, uses no more than 5% of the time used by traditional pixel-based methods in the 2D experiment. If fast sweeping is applied, the reconstruction

time can be no more than 0.3% of the time used by traditional method. Actually, it is also the key idea of this work that change a pixel-based problem with numerous unknowns to be a object based problem with only few unknown parameters.

Moreover, the reconstructed image, using MMSLS, is smooth, and the edge is perfectly preserved. The visualization is therefore much better than when using other approaches. And mesh generation is no longer crucial, because a finer mesh can be generated with only a small addition to the calculation.

Another impressive advantage of this approach is that it can accomplish segmentation and reconstruction at the same time. Actually, the zero level set is the desired segmentation. This is a very useful feature in clinical application.

CHAPTER 5 FIBER TRACKING BY FRONT PROPAGATION

In this chapter, front propagation method is applied to fiber tracking for DW-MRI. The proposed method solves multi-diffusion-direction, branches and tracking back problems existing in fiber tracking problems.

5.1 Introduction

Diffusion-weighted MRI (DW-MRI) is a technique used for relating image intensities to the relative mobility of endogenous tissue water molecules. Two equal and opposite large magnetic field gradients are applied before the data are acquired. In the absence of any motion of the water molecules, the magnetic spins will be de-phased by the first gradient, and then completely re-phased by the second gradient. However, because the actual motion of the water molecules is that of a random walk, the second gradient will not completely re-phase the spins. The signal intensity will therefore be exponentially attenuated proportional to the mean diffusion length. Areas with relatively high mean diffusion length will appear dark on the MRI images relative to areas with low mean diffusion length.

Diffusion Tensor Imaging (DTI) is an application of diffusion imaging where several sets of DW-MRI are acquired with the diffusion gradients applied in different directions. This technique enables the detection of diffusion anisotropy in various mediums such as brain white matter. The diffusive properties of an anisotropic medium can be described with a 3 X 3 symmetric tensor. The eigenvalues of the diffusion tensor are the diffusion coefficients in the three principal directions of diffusivity, and the

eigenvector corresponding to the largest eigenvalue is the main diffusivity direction in the medium. It is then possible to construct image maps from the main diffusivity direction, and for various anisotropy indices calculated from the eigenvalues. The anisotropy indices range from 0, in the case of completely isotropic diffusion, to 1, in the case of completely anisotropic diffusion. And the index is called fractional anisotropy (fa).

Let $\lambda_1, \lambda_2, \lambda_3$ be the three eigenvalues and $\varepsilon_1, \varepsilon_2, \varepsilon_3$ be the three eigenvectors; fractional

$$\text{anisotropy may be defined as } fa = \frac{\sqrt{(\lambda_1 - \lambda_2)^2 + (\lambda_2 - \lambda_3)^2 + (\lambda_1 - \lambda_3)^2}}{\sqrt{2}\sqrt{\lambda_1^2 + \lambda_2^2 + \lambda_3^2}}.$$

Experimental evidence has shown that water diffusion is anisotropic in organized tissues such as muscles or brain white matter. In the last decade, the quantitative description of this anisotropy with DTI has become well established in the research environment and its first applications in the clinic are now being reported. These applications employ both the directional anisotropy that can be measured by DTI as well as removal of this anisotropy through the use of the tensor trace. For example, DTI is presently being explored as a research tool to study brain development, multiple sclerosis, amyotrophic lateral sclerosis (ALS), stroke, schizophrenia and reading disability, while trace imaging has become an essential part of clinical acute stroke assessment. As first shown by Basser et al. [120], the diffusion ellipsoid obtained from DTI can not only provide a quantitative orientation-independent measure of diffusion anisotropy, but also the predominant direction of water diffusion in image voxels. However, it was not until the end of the decade and the beginning of the new millenium that the first successful *in vivo* fiber tracking results were published [121-123]. The reason for this time lag between the availability of the tensor diagonalization techniques that provide the vector

information and the actual mapping of the fibers is due to the inherent complexity of connecting these macroscopic voxel-based vectors in a reproducible three-dimensional manner. At present, new tracking algorithms are being developed rapidly. In order to better utilize this promising technology, it is important to understand the basis of the anisotropy contrast in DTI and the limitations imposed by using a macroscopic technique to visualize microscopic restrictions. These basics are briefly reviewed, while a more comprehensive overview is presented by Beaulieu et al. [124]

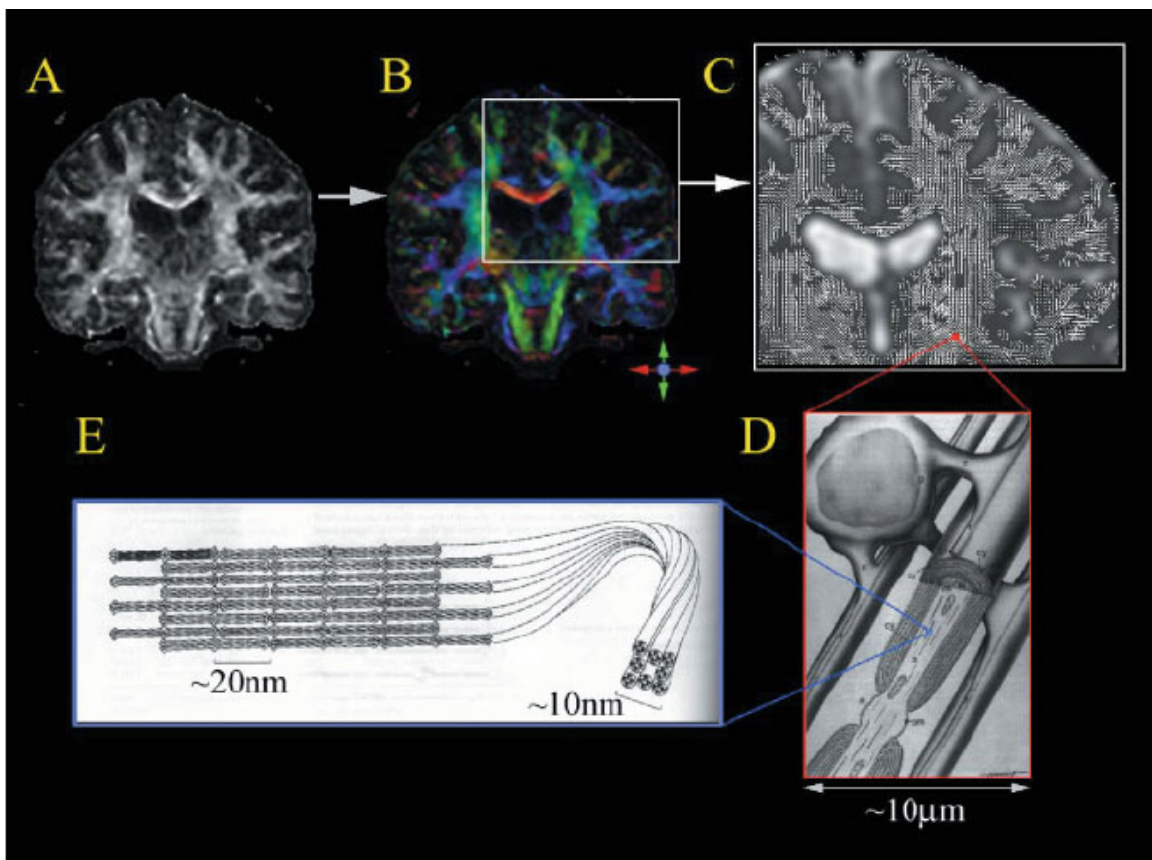


Figure 5-1. White matter structure and its relationship with the information provided by DTI. A) anisotropy map, B) color-coded map, C) vector map, D) a pixel contains bundles of axons and neuroglial cells, E) axon filled with neuronal filaments

5.1.1 Understanding the Basis of DTI

DTI essentially provides two types of information about the property of water diffusion; the extent of diffusion anisotropy and its orientation. By assuming that the largest principal axis of the diffusion tensor aligns with the predominant fiber orientation in an MRI voxel, we can obtain 2D or 3D vector fields that represent the fiber orientation at each voxel. The 3D reconstruction of tract trajectories, or tractography, is a natural extension of such vector fields. Before further describing tractography, it is important to discuss what exactly DTI measures and how the data relate to the tract trajectories we are trying to derive from the measurement.

Figure 5-1 is the Figure 1 in [125]. This figure explains the basis of DTI. As we mentioned above, in DWI, areas with relatively high mean diffusion length will appear darker on the MR images compared to areas with low mean diffusion length. Figure 5-1 A) is a slice of anisotropy image based on DWI. DTI is a set of DWI acquired with the diffusion gradients applied in different directions. In typical DTI measurements, the voxel dimensions are in the order of 1–5 mm and DTI measures the averaged diffusion properties of water molecules inside it. Figure 5-1B and C show the tracts that are running along various directions that are large enough to discern visually. Figure 5-1B uses color to show the directions. Please notice the colored arrows beside B. The red indicates fibers running along the right-left direction, green inferior-superior, and blue anterior-posterior. Figure 5-1C is the vector field map. Very often, image resolution is sufficiently high for the white matter tracts to contain several voxels. The white matter tracts, in turn, consist of densely packed axons (neuronal projections) in addition to various types of neuroglia and other small populations of cells. Figure 5-1D shows a cell. Inside the voxel, water molecules are distributed between these cell types and the

extracellular space (80–85% are intracellular). Thus, even a voxel within a single white matter tract consists of very inhomogeneous environment, and water molecules are likely to experience high anisotropy as judged from the cytoarchitecture of the axon. Inside an axon, water molecules are surrounded by high concentration of neuronal filaments, which are polymers of protein molecules. Figure 5-1E shows the neuronal filaments in an axon. Each monomer protein has a molecular weight of 50–150 kDa. The neuronal filament is far larger than that, and multiple filament bundles are densely packed in the axon. The axonal membrane as well as the well-aligned protein fibers within an axon restricts water diffusion perpendicular to the fiber orientation, leading to anisotropic diffusion. Myelin sheaths that surround the axons may also contribute to the anisotropy for both intra- and extracellular water. These contributions have been studied in detail by Beaulieu [124] using non-myelinated axons, showing that the contribution of myelin may be significant, but that the axonal contribution dominates. In addition to the inhomogeneity in terms of the cellular environment of water molecules, inhomogeneity of axonal orientation within one voxel is also an important factor to be considered.

Despite this multi-directional environment, previous DTI studies have shown that water diffusion in many regions of the white matter is highly anisotropic (Figure 5-1A) and that the orientation of the largest principal axis aligns to the predominant axonal orientation. However, when studying axonal architecture using DTI, it is very important to understand the limitations arising from the inhomogeneity of the water environment. First, the conventional DTI data acquisition and processing methods may not be able to properly handle **a voxel containing more than one population of axonal** tracts with different orientations. This issue will be discussed in more detail below. Second, DTI

cannot provide information on **cellular-level axonal connectivity**. Multiple axons from individual cells may merge into or branch out from one voxel. Within a voxel, cellular-level axonal information of multiple compartments is averaged. The third important limitation is that **afferent and efferent pathways of axonal tracts** cannot be judged from the direction of water diffusion.

To resolve the problem of multiple fiber orientations within a single voxel, high angular resolution diffusion imaging (HARD) was proposed by Tuch *et al.* in [126, 127]. In HARD, a geodesic, high b -value diffusion gradient sampling scheme is applied. In regions of fiber crossing the diffusion signal exhibited multiple local maxima/minima as a function of diffusion gradient orientation, indicating the presence of multiple intravoxel fiber orientations. The multimodality of the observed diffusion signal precluded the standard tensor reconstruction, so instead the diffusion signal was modeled as arising from a discrete mixture of Gaussian diffusion processes in slow exchange, and the underlying mixture of tensors was solved for using a gradient descent scheme. The multi-tensor reconstruction resolved multiple intravoxel fiber populations corresponding to known fiber anatomy.[127]

We will first discuss recent 3D tract reconstruction techniques that employ 3D vector fields obtained from DTI measurements. Because of the advantages of HARD-MRI, we propose our fiber reconstruction method for HARD-MRI.

5.1.2 Existing Fiber Reconstruction Methods

Currently, there are several different approaches to reconstruct white matter tracts, which can be roughly divided into three types. Techniques classified in the first category are based on line propagation algorithms that use local tensor information for each step of the propagation. The main differences among techniques in this class stem from the way

information from neighboring pixels is incorporated to define smooth trajectories or to minimize noise contributions. [128-130] The second type of approach is front evolution methods. In this kind of method, all possible directions are tried, the result obtained is first the front, and then the track corresponding to that front [131, 132]. The basic ideas of those two kinds of methods are introduced here.

5.1.2.1 Line propagation algorithms

The most intuitive way to reconstruct a 3D trajectory from a 3D vector field is to propagate a line from a seed point by following the local vector orientation. Notice, if a line is propagated simply by connecting pixels, which are discrete entities, the vector information contained at each pixel may not be fully reflected in the propagation. In the simple example illustrated in Figure 5-2A, axonal tracts are running along 30° from the vertical line. When applying the discrete ‘pixel connection’ approach, a judgment has to be made about which pixel should be connected (for instance, is the 30° vector angle pointing at pixel (1, 2) or (2, 2)?). No matter what the judgment is, it should be clear that this simple pixel connection scheme cannot represent the real tract even in such a simple case. Because in this simplest method, only the node (discrete integers in coordinates) has direction and the fiber only passes through the nodes, hence the field is discrete number field. The simplest way to convert the discrete voxel information into a continuous tracking line is to linearly propagate ‘a line’, in a continuous number field. It is called continuous field because it is assumed that the whole voxel has the same direction and any point (continuous in coordinates) has direction. This conversion from the discrete to continuous number field is shown in Figure 5-2B.

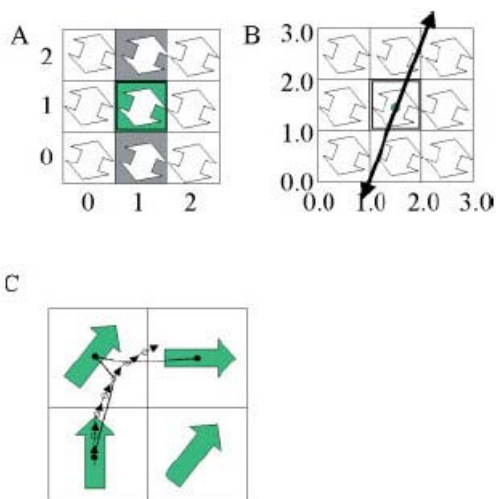


Figure 5-2. Linear line-propagation approach. Double-headed arrows indicate fiber orientations at each pixel. Tracking is initiated from the center pixel. A) discrete number field. The shaded pixels are connected, B) continuous number field. A line instead of a series of pixels is propagated. C) interpolation approach to perform nonlinear line propagation. Large arrows indicate the vector of the largest principal axis. For every step size, a distance-weighted average of nearby vectors is calculated.

The simple linear approach demonstrated in Figure 5-2A, B can be modified to create a smooth (curved) path, which should be more accurate when the curvature of the constructed line is steep with respect to imaging resolution. A schematic diagram of a simple interpolation approach that can achieve such a smooth path is shown in Figure 5-2C. In this example, the line is propagated with a small, predefined step size. Whenever it moves to a new coordinate, a distance-averaged vector orientation is calculated. In this most simple example, the average distance between two pixels closest to the new coordinate was used to draw a smooth line between pixels. In more rigorous approaches, diffusion tensors, rather than the vector of the largest principal axis, are interpolated at each coordinate as the line is being propagated. Notice Figure 5-2C used a different vector field than A and B; the reason is that the result of interpolation approach is same as continuous propagation method for the vector field in B.

With interpolated diffusion tensors, we have the following propagation method. Let white matter fiber tract trajectory be represented as a 3D space curve, i.e., a vector, $r(s)$, parameterized by the arc length, s , of the trajectory. The Frenet equation describing the evolution of $r(s)$ is

$$\frac{dr(s)}{ds} = t(s) \quad (5-1)$$

where $t(s)$ is the unit tangent vector to $r(s)$ at s . These vectors are depicted in Figure

5-3.

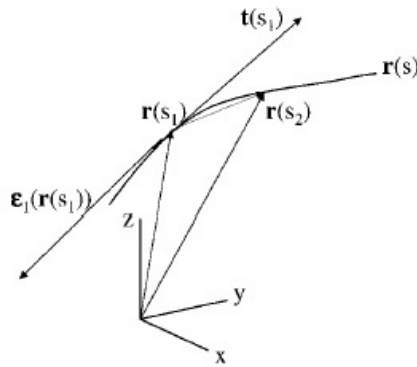


Figure 5-3. White matter fiber trajectory as a space curve $r(s)$. The local tangent vector, $t(s_1)$, is identified with the eigenvector, $\varepsilon_1(r(s_1))$, associated with the largest eigenvalue of the diffusion tensor, \mathbf{D} , at position $r(s_1)$

Since the normalized eigenvector, ε_1 , associated with the largest eigenvalue of the diffusion tensor, \mathbf{D} , lies parallel to the local fiber tract, the direction in coherently organized white matter. Within acceptable experimental error, several groups have confirmed this to be true in the human heart. A key idea in this fiber tract following algorithm is to equate the tangent vector, $t(s)$, and the unit eigenvector, ε_1 , calculated at position, $r(s)$:

$$t(s) = \varepsilon_1(r(s)) \quad (5-2)$$

Combine (1) and (2) , we have

$$\frac{dr(s)}{ds} = \varepsilon_1(r(s)) \text{ with subject to } r(0) = r_0 \quad (5-3)$$

Where r_0 specifies a starting point on the fiber tract. This procedure can now be repeated starting at the new point, $r(s_1) \dots$, and can be iterated to predict the location of discrete points along the fiber trajectory, $r(s)$.

5.1.2.2 Front evolution methods

Front evolution methods are based on the step-wise evolution of a front from an initial seed point. The speed and direction of evolution of the front are calculated from the local diffusion information, such that evolution is fastest along the direction of fastest diffusion.

Parker, Wheeler-Kingshott and Barker first introduced the front evolution method in [131]. The method in [131] is based on the fast marching method [133]. There are 4 steps in this method. First step is the evolution of a front from a seed point using a variant of the fast marching method at a rate governed by a speed function. $T(r) = T(r') + \frac{|r - r'|}{F(r)}$.

Where $T(r)$ is what we want to find, which is the propagation front. r' is chosen to be the neighbor for which $(r - r')$ is most closely aligned with the direction of normal to the front, $n(r)$. $F(r)$ is the speed function, which is defined as

$$F_1(r) = \frac{1}{1 - \min(\left(\left(\varepsilon_1(r) \bullet \bar{n}(r) \right), \left(\varepsilon_1(r') \bullet \bar{n}(r) \right), \left(\varepsilon_1(r) \bullet \varepsilon_1(r') \right) \right))} \quad (5-4)$$

or

$$F_2(r) = \min(F_2(r'), \left| \varepsilon_1(r') \bullet \bar{n}(r) \right|) \quad (5-5)$$

Where $\varepsilon_1(r)$ is the dominant tensor direction at pixel r . The second step is the generation of paths from all points in a given data set to the seed point.

$T(r) = \min_{\gamma} \int_A^r |\nabla T(\gamma(\tau))| d\tau$, where γ is the path. The third step is the creation of a

connectivity metric, ϕ , which assigns a measure of connectivity for a given path based on the worst case along the length of the path of the property to which they are sensitive.

Define

$$\phi_1(\gamma) = \min_{\tau} F(\gamma(\tau)) = \min_{\tau} \frac{1}{|\nabla T(\gamma(\tau))|} \quad (5-6)$$

or

$$\phi_2(\gamma) = \min_{\tau} (|w(\gamma(\tau)) \bullet \varepsilon_1(\gamma(\tau))|) \quad (5-7)$$

The last step is the selection of a subset of the paths as being reasonable pathways of connection, which are points with a high connectivity to the seed point.

Tournier et al. proposed another front evolution method in [132]. Although this technique holds certain similarities to the Fast Marching Algorithm proposed by Parker et al., here the front is not evolved in a voxel-by-voxel manner, and there is no gradient descent to establish the actual tracks. Hence this method is faster than Parker's.

5.1.3 Several Considerations in Fiber reconstruction

For any fiber reconstruction method, there are several general considerations.

5.1.3.1 Termination criteria

Line propagation or front evolution must be terminated at some points. The most intuitive termination criterion is the extent of anisotropy. In a low anisotropy region, such as gray matter, there may not be a coherent tract orientation within a pixel and the orientation of the largest principal axis is more sensitive to noise errors (for isotropic

diffusion, the anisotropy information is dominated by noise and becomes purely random). The fractional anisotropy of the gray matter is typically in the range 0.1–0.2. Therefore, one simple termination approach is to set the threshold for tracking termination at 0.2. Another important criterion is the angle change between pixels. For the linear line propagation model, large errors occur if the angle transition is large. Even for the interpolation approach, it should be noted that the diffusion tensor calculation assumes that there is no consistent curvature of axonal tracts within a voxel. The presence of curvature violates the assumption that the diffusion process along any arbitrary axis is Gaussian, thereby invalidating the routine tensor calculation. Therefore, it is preferable to set a threshold that prohibits a sharp turn during line propagation. The significance of this angle-transition threshold depends on the particular trajectories of tracts of interest and the image resolution. An image resolution of 1–3 mm, for example, is high enough to smoothly reconstruct the curvature of trajectories of major tracts in the brainstem and the corticocortical association fibers connecting the functional regions of the brain. Under such favorable conditions, the angles between connected vectors are small and the termination criteria are dominated by the magnitude of the fractional anisotropy. However, for smaller tracts in environments that are structurally highly convoluted, such as sub-cortical U-fibers, the same resolution may be too coarse to smoothly represent the trajectories and, thus, analysis for the errors in tensor calculations and fiber tracking due to the curvature becomes more important. While at this moment there are no comprehensive simulation studies in this regard, some preliminary data on the effect of the turning radius on the tracking results in particular examples can be found in recent reports.

5.1.3.2 Effect of noise

3D vector field obtained from DTI contains noise and, as a consequence, the calculated vector direction may deviate from the real fiber orientation. One of the drawbacks of line propagation methods is that noise errors accumulate as the propagation becomes longer. The extent of these errors as a function of signal-to-noise ratio (SNR) has been evaluated for linear and interpolated models. The results show a dependence on the shape of the trajectory, anisotropy, resolution and the particular interpolation method used. The noise effect can be reduced using smoothing or interpolation techniques, which averages vector or tensor information among neighboring pixels with a cost in the reduction in effective resolution. More information can be found in [134].

5.1.3.3 Branching

White matter tracts often have extensive branching, which renders tracking computationally complex. For example, bifurcation of a line during propagation is already a mathematically involved issue. From a programming point of view, merging two lines rather than splitting a line into two can much more easily handle this problem. In this approach, tracking is initiated from all pixels within the brain and tracking results that penetrate the pixel of interest are kept. In other words, instead of using the pixel of interest as a seed pixel, all pixels in the brain are used as seed pixels.

5.1.3.4 Algorithms to interpolate a tensor field

In case the resolution of MRI image is low, it is necessary to interpolate the tensor field to get the smooth fiber. There are several ways to generate the interpolated tensor field.

Since the tensor field is from MR images, the first possible object to interpolate is the raw diffusion weighted MR images [123], and then use the interpolated high

resolution MR images to calculate the tensor field. This is the most defensible method; however there are considerable computational expenses.

The second choice is *matrix interpolation*, wherein the tensor matrix, \mathbf{D} , is calculated once per sample point, and then interpolated component-wise to produce a tensor at intermediate locations. Were the components of the tensor matrix simply linear combinations of the measured channels, then matrix interpolation would be equivalent to raw image interpolation. However, in reality, the components of the tensor matrix are not linear combinations of the measured channels.

The last choice is to interpolate eigenvalues or eigenvectors. Kindlmann, Weinstein and Hart [135] called this kind of interpolation *eigensystem interpolation*. This has immediate relevance for the barycentric map methods of assigning color and shading, and the lit-tensor shading model. This style of interpolation has the tremendous benefit of doing all the eigensystem calculations once as a pre-process, and storing the results at each dataset point. Despite its obvious benefits, there is a subtle issue of *correspondence*, which complicates eigensystem interpolation.

5.1.3.5 Display of experimental tracks

Track display is important for understanding the 3D shape, anatomical location, relative spatial relationships, and internal fiber structure of pathways. The precise anatomical location of tracks can be visualized using *2D anatomical overlays* of tracks onto anatomical background images. If any bead in a pathway is found to lie inside a given voxel, that voxel is assigned the designated color of that pathway. Background images were either I_0 (from DT-MRI) or co-registered 3D T_1 -weighted MP-RAGE images. Visualization of whole-brain track data in 3D can be difficult because of overlapping tracks and limitations in computer graphics. Thus tracks representing

pathways of interest were selectively extracted and displayed. From the whole-brain data, tracks are extracted if they pass into a *spatial selection volume* (SSV). This selection procedure is passive and does not alter the quality of the tracks. The SSVs can be combined with logical operations to obtain a pathway or its component subsets.

5.1.4 Limitations of Existing Methods

Linear propagation methods suffer from three major disadvantages. Firstly, there is no (or at best limited) natural mechanism to allow for the branching of tracts from a single start point (an anatomically reasonable occurrence at the spatial resolution of DTI data, is seen, for example, in the corona radiata); (which means) meaning that connectivity is restricted to a representation as a one-to-one mapping between points in different regions. It is possible to produce a limited impression of diverging pathways with streamline-like methods by utilizing multiple interpolated start points within the start voxel. However, the density of traces after the point of branching or fanning will reduce as the traces diverge when using these techniques, thus undersampling (in general in a non-uniform manner) subsequent connected regions. This change in density will not in general represent any reduction in packing density of the underlying axons. Therefore, this kind of method cannot take advantage of high angular resolution data. The second major restriction is that there is no attempt to determine how reasonable, or likely, any path is in representing a “true” pathway of connections as demonstrated by Pierpaoli et al. [136]. Furthermore, this approach suffers from a high susceptibility to noise; the error caused by noise could be accumulated during the propagation.

Front propagation methods overcome those shortcomings. First, it allows for the branching of tracts from a single start point, because the front can propagate to any number of directions. Second, the fiber is along the fastest direction of the front and the

speeds in other directions are also known, hence it is easy to determine how reasonable or likely, any path is in representing a “true” pathway of connection. Third, because the evolving element is the front instead of one point on a line in the front- propagation methods, the error caused by local noise may be remitted by propagation from other points.

However, in Parker et al. [131], the front evolution result is a time map, \mathbf{T} , from the seed. To find the paths of connection, a gradient descent has to be established. This computation for determination of connection paths is not simple. Tournier et al. [132] introduced another front propagation method using a fiber orientation probability density function. This method is not the voxel-by-voxel manner, hence the front can evolve to different directions from one seed simultaneously, but the speeds in different directions are different. The speeds are decided by fiber orientation probability density functions. It should be more accurate because it is not voxel-by-voxel manner, however the computation complexity could be dramatically increased. Another drawback of the method of Tournier et al. [132] is that the result is only the front, no “true” path of connection is available.

5.2 Methods

5.2.1 Motivations of the Proposed Method

In this work, we are trying to (partially) solve the problems in existing fiber reconstruction methods.

Since front propagation method can solve the main problems in linear propagation method (see 5.1.4), we also apply front propagation method to track the fibers.

To avoid computation complexity [132], we still use voxel-by-voxel method. That is, we assume the fiber always passes through the nodes. If resolution is low and kinks in

the reconstructed path are evident, interpolation techniques should provide an advantage in accuracy. On the other hand, if the resolution is sufficiently high, the non-interpolating techniques offer faster calculation. According to Mori and Ziji [125], when using DTI images with $1 \times 1 \times 3$ mm resolution, the stretch of the corticospinal tract between the pons and the motor cortex has a rather small average angle of $7.8 \pm 5.8^\circ$ (SD) between connecting pixels, for which the effect of interpolation should be minimal. In case the resolution is not high enough, we need to do interpolation according to 5.1.3.4 before fiber reconstruction.

To find the “true” connection path, the closest point method [31] is applied in our algorithm. In this method, the closest path from the seed to any points in propagated region of the front is recorded during the propagation; then there is no more effort to find the connection path after front propagation. Here we assume the reconstructed fiber tends to minimize its length. Therefore, the “true” connection path can be found in no effort in our algorithm and the calculation for gradient descent [131] is avoided.

Also, a novel definition for propagation speed is applied in our algorithm. According to recent literature [125, 131, 137], the reconstructed fiber should have the following 3 properties: first, the tangential direction of the reconstructed fiber should be same as the direction of water diffusion which is the vector field given by DWI; second, the reconstructed fiber should have no sharp turns that tend to minimize its length; and third, fibers do not pass through gray matter. To achieve the first two properties, Parker et al. [131] define the propagation speed as Equation 5-4 or 5-5 in 5.1.2.2. Formula 5-4 ensures that front evolution will occur most rapidly if both $\varepsilon_1(r)$ and $\varepsilon_1(r')$ are close to being co-linear with each other. The incorporation of the term $F_2(r')$ in Equation 5-5

provides a “memory” of previous iterations of the front position. This can be interpreted as embedding connectivity information already established between the start point and in the value of F_2 . Those definitions are very reasonable. But we notice, first, only one tensor direction $\varepsilon_1(r)$ is considered in formula (5-4) and (5-5). In case there are more than one fiber in one voxel, this approach has no solution. Therefore, in our algorithm all directions from HARD MRI data are considered. Second, we notice that formula (5-4) and (5-5) use the worst case speed. People may argue that it should be better if we consider all those terms together instead of simply choosing the smallest number among them. To address this objection, we propose to use a polynomial to describe all terms together. Given a point r and a tensor direction $\varepsilon_1(r)$ at that point, we want to find the next point where the fiber should go. Since each neighbor of r may be a candidate, for each neighbor r^i we construct local fiber connecting r and the neighbor by a polynomial and force it to pass through those two points with the tangential direction $\varepsilon_1(r)$ at r and $\varepsilon_1(r^i)$ at r^i , then the local fiber follows the first property. To follow the second property, we calculate the length of those curves defined by those polynomials and find the shortest one. And then we choose the corresponding r^i as the next point of r . Because the length of the curve is decided by curvature and torso, the shortest curve has most likely no sharp turn and hence follows the second property of the reconstructed fiber. To smoothly connect those piecewise polynomials, we need to avoid sharp turns at the connection nodes, hence the angle between the direction in previous point of r and the direction of the next point of r is calculated, and a threshold is set to avoid sharp turn.

The third property of the reconstructed fiber is used as a termination condition in our algorithm. Our algorithm is based on the idea of fast marching, and the termination

condition of fast marching method is when the set of neighborhoods becomes empty [74]. We delete an entry from the set of neighborhoods when the next propagating point of this entry is isotropic or when a sharp turn happens.

To deal with noise problem and interpolation before fiber reconstruction, we proposed a method in [134]. Please refer to this paper for details. To display the tracking result, 1.5 T MR image is used as background.

5.2.2 Data Description

There are four sets of data used as input for the proposed method. First, the three-dimensional diffusion direction field generated with DWI data. In [134], we reported the details. For the tracking algorithm, we assume that the input data has low noise, high resolution, and more than 1 directions in some voxels. Second, the segmentation result of gray matter was generated with 1.5 T MRI data. The segmentation result is used as termination result in our algorithm. Third, seeds, the start region of the fibers, were given by experts; fourth, the targets (i.e. the interested regions the fibers may pass through) were given by experts.

5.2.2 Front Evolution and Path Record

The first step toward determining paths of connection to a given start, or seed, involves the growth of a volume from this point. This is achieved using a modified version of the fast marching algorithm, a rapid implementation of boundary-value level sets methods [138]. We are primarily interested in the behavior of the surface of the volume (the front). The speed, at which the front propagates from the start point(s), is linked to the information contained in the field. Each iteration of the front position evolution involves the determination of the speed at candidates, which are the neighbors of the front. Let

r : the current point which is on the front

r' : the previous point of r on the fiber

r'' : the next possible point on the fiber neighboring r .

$d(r,i)$: the i^{th} fiber direction at r

$d(r',k)$: the k^{th} fiber direction at r' which is used to connect r and r'

$C(r,r'',i,j)$: the cubic polynomial that pass through r and r'' , the tangential direction of $C(r,r'',i,j)$ is $d(r,i)$ at r and $d(r'',j)$ at r''

Then the speed $S(r,r'',i,j)$ from r to r'' with $d(r,i)$ and $d(r'',j)$ direction is defined as

$$S(r,r'',i,j) = \frac{\text{Length}(C(r,r'',i,j)) + \text{Length}(C(r',r,k,i))}{\text{Length}(r'-r'')} \quad (5-8)$$

and the speed $S(r,r'')$ from r to r'' is defined as

$$S(r,r'') = \frac{1}{\min_{i,j} S(r,r'',i,j) - \text{const}} \quad (5-9)$$

Cubic polynomial $C(r,r'',i,j)$ is used here to approximate the local fiber path, so the first property of the reconstructed fiber is satisfied. The definition of Equation 5-1 is a measure of the length of the local fiber. The definition of Equation 5-2 is the inverse of the minimum length of local fibers which connects r and r'' . So the second property of the reconstructed fiber is satisfied. *const* is a constant number used to exaggerate the difference of speeds. For 3D, there are 26 neighbors for each voxel. The neighbors which have already in the same fiber or which are not gray matter are not considered as candidates. Here the third property of the reconstructed fiber is satisfied. Notice the speed

is defined for each direction of r , the missing branch problem of [131] mentioned in previous section can be avoided.

In each iteration, we calculate the speeds for all neighbors of the current point r , and then find the greatest speed among all neighbors. Notice all neighbors are considered, not only the neighbors of r , but also neighbors of each front point]; hence the branching problem and noise accumulation problem in linear propagation method are solved. If the greatest speed is greater than a threshold, then add the neighbor r'' , which has the greatest speed, into the fiber. Save r and r'' and the directions used to generate the greatest speed for the next iteration and tracking back in the future. r is called the closest point of r'' . So r' is the closest point of r . We save all the speed information for the neighbor speed contest in the future. If the greatest speed is less than the threshold, then change the current point r to be another possible point on the front and mark r as an impossible point. We continue this process, until no possible points available or the fiber arrives at a point in the target region.

We repeat the front evolution process for each seed.

5.2.4. Tracking Back

After the process of front evolution, the fiber starts from one seed may have many branches, see Figure 5-1E. We need find the shortest path to connect the target and seed. Based on the closest point idea (or “greedy” algorithm), we start from the point r that the fiber touches in the target. We then read the saved record of the fiber to find the closest point r' of r , save it, and then find the closest point of r' , and save it too. We repeat this process until we track the fiber back to the seed. This is the shortest path connecting the seed and the target point.

Figure 5-4 shows the flow chart of the proposed algorithm.

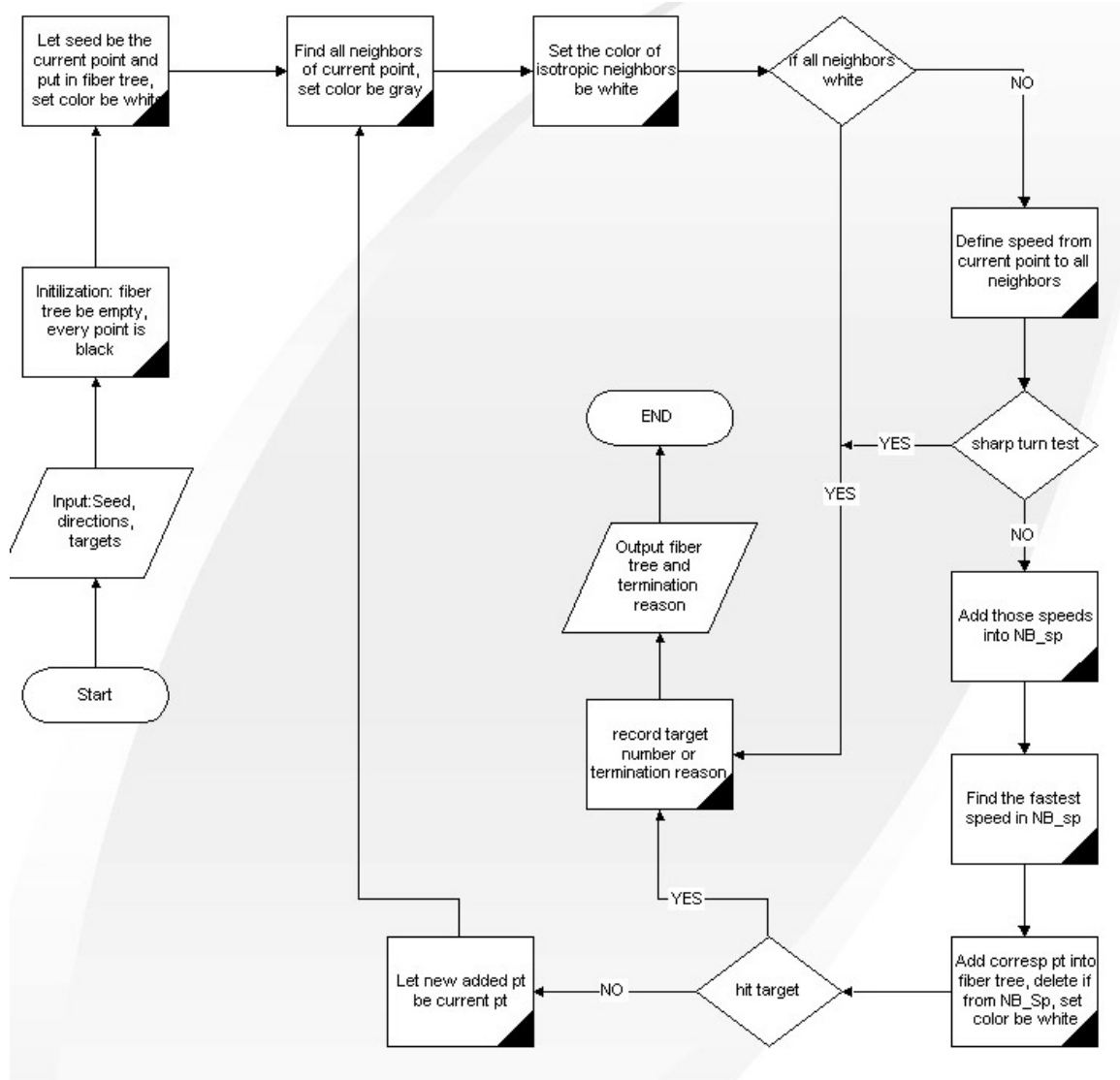


Figure 5-4. Flow chart of fiber tracking by fast marching on grids

5.3 Experiments and Results

The proposed tracking method was applied to human MRI data. Given one region of seeds and two regions of targets, fibers starting from the seeds will touch one of those two regions or touch none of them. The purpose of this experiment is to find the ratio of touching and the path of those fibers.

DWI brain data were acquired using a GE 3.0-tesla scanner using a single-shot spin echo EPI sequence. The scanning parameters for the DWI acquisition are: repetition time(TR) = 1000ms, echo time(TE) = 85 ms, the field of view (FOV) = 220 mm× 220 mm. 24 axial sections covering the entire brain with the slice thickness = 3.8mm and the intersection gap = 1.2mm.

Because it is required that the fiber has to pass through grids, this algorithm is reasonable when high resolution DWI is available. In general case, it is difficult to get the high resolution DWI, hence the DWI data for this experiment is interpolated. The interpolated and denoised tensor direction field is generated according to [134]. Dr Yijun Liu provided the seeds and target regions. There are 149 start points.

The proposed tracking method was applied. The total tracking time is 240 seconds. Figure 5-5 shows the data and results. Out of 149 seeds, 92 touched target 1, 11 touched target 2, with a ratio 8.4:1. Figure 5-5A is the seeds region, the background is MR Image of that slice. Figure 5-5B is the mask for seeds slice, fiber can not go out of the mask because there is no fiber in white matter, this mask is used as a termination condition. Figure 5-5C is the map of target regions. The yellow region is target 1. The pink region is target 2. The background is the MR Image of this slice. Figure 5-5D is the mask on targets slice. Figure 5-5E is one example of the reconstructed fiber. We can see that the reconstructed fiber has several branches. It shows that the proposed method solves the branching problem. Figure 5-5F shows the correspondence between seeds and targets. The fibers start from yellow region arrive target 1, the fibers start from red region arrive target 2. The fibers that start from the blue region miss both targets. Figure 5-5G and H show all reconstructed fibers in 3D anatomic images. The lower slice is the seed slice.

The upper slice is the f_a map of targets slice. The two targets are shown by different colors in the f_a map. Fibers arrive different targets are shown by different colors. G and H are different views for the same image.

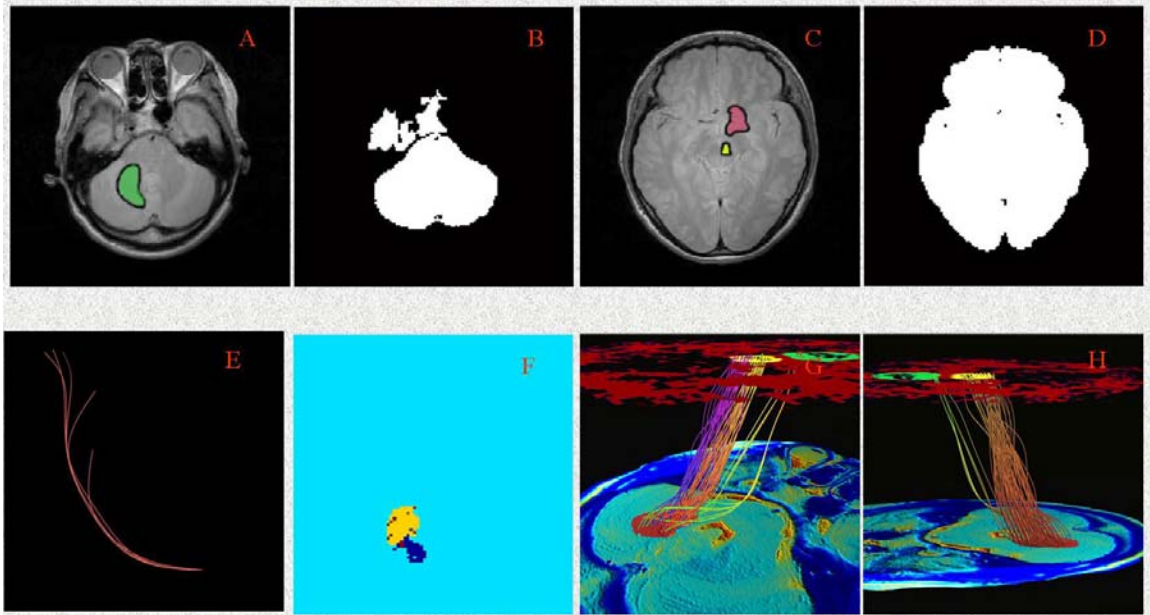


Figure 5-5. Fiber tracking results. A) the seeds region, B) the mask for seeds slice, C) the map of target regions, D) the mask on targets slice, E) one example of reconstructed fiber, F) the correspondence between seeds and targets, G) and H) all reconstructed fibers in 3D anatomic images

5.4 Conclusion

A novel tracking algorithm is proposed. To solve the problems in existing front evolution methods, there are three major differences between this work and other front evolution methods. First, local polynomial fitting is used to define evolution speed. Second, the closest point method [31] is applied to find the most reasonable path to connect two points. Third, fast marching method is modified to deal with multi-diffusion-directions in some voxels.

The proposed method solves multi-diffusion-direction, branches and tracking back problems existing in fiber tracking problems. There is one parameter (the threshold for

speed) to choose, hence it is easy to use. The method is fast: it only spent several minutes in all of our experiments. Experiments on simulated and human brain data show the effectiveness of this method.

The drawback of this algorithm is that it requires that the fiber to pass through grids which is not reasonable when the image resolution is low. A more general algorithm will be shown in a separate work.

LIST OF REFERENCES

- [1] M. Kass, A. Witkin, and D. Terzopoulos, "Snakes: Active contour models," *International Journal of Computer Vision*, vol. 1, pp. 321-331, 1987.
- [2] P. Perona and J. Malik, "Scale-space and edge detection using anisotropic diffusion," *IEEE Trans. Pattern Anal. and Mach. Intell.*, vol. 12, pp. 629-639, 1990.
- [3] M. Bertalmio, G. Sapiro, V. Caselles, and C. Ballester, "Image inpainting," presented at SIGGRAPH Computer Graphics Proceedings, 2000.
- [4] A. J. Baxter, Y. F. Mangnall, E. J. Loj, B. H. Brown, D. C. Barber, A. G. Johnson, and N. W. Read, "Evaluation of applied potential tomography as a new non-invasive gastric secretion test," *Gut*, vol. 30, pp. 1730-1735, 1988.
- [5] S. J. Watson, R. H. Smallwood, B. H. Brown, P. Cherian, and K. D. Bardhan, "Determination of the Relationship Between the pH and Conductivity of Gastric Juice.," *Physiol. Meas.*, vol. 17, pp. 21 - 27, 1996.
- [6] F. A. Duck, *Physical Properties of Tissue -- A Comprehensive Reference Book*. London: Academic Press, 1990.
- [7] P. H. Moller, K. G. Tranberg, B. Blad, P. H. Henriksson, L. Lindberg, L. Weber, and B. R. R. Persson, "EIT for measurement of temperature distribution in laser thermotherapy.," in *Clinical and Physiological Applications of Electrical Impedance Tomography.*, vol. 24, D. Holder, Ed. London: UCL Press, 1993, pp. 217-226.
- [8] F. J. McArdle, B. H. Brown, and A. Angel, "Imaging cardiosynchronous impedance changes in the adult head.," in *Clinical and Physiological Applications of Electrical Impedance Tomography*, vol. 20, D. Holder, Ed. London: UCL Press, 1993, pp. 177-184.
- [9] D. S. Holder, "Physiological constraints to imaging brain function using scalp electrodes," in *Clinical and Physiological Applications of Electrical Impedance Tomography*, vol. 21, D. Holder, Ed. London: UCL Press, 1993, pp. 185-200.
- [10] N. D. Harris, A. J. Suggett, D. C. Barber, and B. H. Brown, "Applications of applied potential tomography (APT) in respiratory medicine," *Clin. Phys. Physiol. Meas.*, vol. 8, pp. 155-165, 1987.

- [11] B. Blad and B. Baldetorp, "Impedance spectra of tumor tissue in comparison with normal tissue: A possible clinical application for electrical impedance tomography," *Physiological Measurement*, vol. 17 Suppl 4A, pp. 105-115, 1996.
- [12] N. Chauveau, "Ex vivo discrimination between normal and pathological tissues in human breast surgical biopsies using bioimpedance spectroscopy," *Annals of the New York Academy of Sciences*, vol. 873, pp. 42-50, 1999.
- [13] J. C. Buell, "A practical, cost-effective, noninvasive system for cardiac output and hemodynamic analysis," *American Heart Journal*, vol. 116, pp. 657-664, 1988.
- [14] D. Weinstein, L. Zhukov, and G. Potts, "Localization of Multiple Deep Epileptic Sources in a Realistic Head Model via Independent Component Analysis," School of Computing, University of Utah, Salt Lake City UUCS-2000-004, 2000.
- [15] D. Sodickson and W. Manning, "Simultaneous acquisition of spatial harmonics (SMASH): Ultra-fast imaging with radiofrequency coil arrays," *Magn Reson Med*, vol. 38, pp. 591 - 603, 1997.
- [16] K. P. Pruessmann, M. Weiger, M. B. Scheidegger, and P. Boesiger, "SENSE: Sensitivity Encoding for Fast MRI," *Magn Reson Med*, vol. 42, pp. 952 - 962, 1999.
- [17] D. LeBihan, "Diffusion, perfusion and functional magnetic resonance imaging," *J Mal Vasc*, vol. 20, pp. 203-14, 1995.
- [18] M. E. Moseley, Y. Cohen, J. Mintorovitch, L. Chileuitt, J. Suruda, D. Norman, and P. Weinstein., "Evidence of anisotropic self-diffusion in cat brain," presented at 8th Annual Meeting of SMRM, Amsterdam, 1989.
- [19] M. E. Moseley, J. Kucharczyk, H. S. Asgari, and D. Norman, "Anisotropy in diffusion weighted MRI," *Magn. Reson. Med*, vol. 19, pp. 321-326, 1991.
- [20] P. J. Basser and C. Pierpaoli, "Microstructural and physiological features of tissues elucidated by quantitative diffusion tensor MRI," *Magn. Reson. Med*, vol. 111(B), pp. 209-219, 1996.
- [21] D. Mumford and J. Shah, "Optimal approximation by piecewise smooth functions and associated variational problems," *Communications in Pure and Applied Mathematics*, vol. 42, pp. 557-685, 1989.
- [22] L. Rudin, S. J. Osher, and E. Fatemi, "Nonlinear total variation based noise removal algorithms," *Physica D*, vol. 60, pp. 259-268, 1992.
- [23] R. Acar and C. R. Vogel, "Analysis of total variation penalty methods for ill-posed problems," *Inverse Problems*, vol. 10, pp. 1217-1229, 1994.

- [24] D. Strong, "Adaptive total variation minimization image restoration," UCLA, 1997.
- [25] T. Chan and D. Strong, "Relation of Regularization Parameter and Scale in Total Variation Based Image Denoising," Dept. of Math, UCLA, Los Angeles CAM 96-7, 1996.
- [26] Y. Chen and W. Wunderli, "Adaptive total variation for image restoration in BV space," *J. Math. Anal. Appl*, vol. 272, pp. 117-137, 2002.
- [27] Y. Chen, S. Levine, M. Rao, and J. Stanich, "Functions of $p(x)$ -Growth in Image Restoration," *submitted to SIAM J. Appl Math*, 2003.
- [28] S. Osher and J. A. Sethian, "Fronts propagating with curvature dependent speed: algorithms based on Hamilton-Jacobi formulations," *J. Comput. Phys.*, vol. 79, pp. 12-49, 1988.
- [29] H.-K. Zhao, S. Osher, and R. Fedkiw, "Fast surface reconstruction using the level set method," presented at IEEE Workshop on Variational and Level Set Methods (VLSM'01), Vancouver, Canada, 2001.
- [30] S. Chen, B. Merriman, M. Kang, R. E. Caflisch, C. Ratsch, L. Cheng, M. Gyure, R. P. Fedkiw, and S. Osher, "Level set method for thin film epitaxial growth," *J. Comput. Phys.*, vol. 167, pp. 475-500, 2001.
- [31] Y. R. Tsai, "Rapid and Accurate Computation of the Distance Function Using Grids," UCLA CAM, Los Angeles 00-36, 2000.
- [32] B. Pompe, P. Blihd, D. Hoyer, and M. Eiselt, "Using mutual information to measure coupling in the cardiorespiratory system," *IEEE Eng Med Biol Mag*, vol. 17, pp. 32-39, 1998.
- [33] A. Collignon, F. Maes, D. Vandermeulen, P. Suetens, and G. Marchal, "Automated multimodality image registration using information theory," presented at Processing in medical Images, Brest, France, 1995.
- [34] G. Hermosillo, C. Chefd'Hotel, and O. Faugeras, "A variational methods for multimodal image matching," *Intl. J. Comp. Visi*, vol. 50, pp. 329-345, 2002.
- [35] C. Ballester, M. Bertalmio, V. Caselles, G. Sapiro, and J. Verdera, "Filling-in by joint interpolation of vector fields and grey levels," *IEEE Trans. Image Process*, vol. 10, pp. 1200-1211, 2001.
- [36] T. F. Chan and J. Shen, "Mathematical models for local non-texture inpaintings," *SIAM J. Appl Math*, vol. 62, pp. 1019-1043, 2001.
- [37] T. F. Chan, S. H. Kang, and J. Shen, "Euler's elastica and curvature based inpaintings," *SIAM J. Appl. Math*, vol. 63, pp. 564-592, 2002.

- [38] S. Esedoglu and J. H. Shen, "Digital inpainting based on the Mumford-Shah-Euler image model," *European J Appl Math*, vol. 13, pp. 353-370, 2002.
- [39] T. F. Chan and L. A. Vese, "Active contours without edges," *IEEE Trans. Med. Imag.*, vol. 10, pp. 266-277, 2001.
- [40] P. Blomgren, T. F. Chan, P. Mulet, and C.K.Wong, "Total Variation Image Restoration: Numerical Methods and Extensions," presented at IEEE International Conference On Image Processing, 1997.
- [41] L. A. Vese and T. F. Chan, "A multiphase level set framework for image segmentation using the Mumford and Shah model," UCLA CAM, Los Angeles 01-25, 2001.
- [42] M. Sussman, P. Smereka, and S. Osher, "A level set approach for computing solutions to incompressible two-phase flow," *J. Comput. Phys.*, vol. 5, pp. 146-159, 1994.
- [43] B. Song and T. F. Chan, "A Fast Algorithm for Level Set Based Optimization," *SIAM J. on Scientific Computing*, 2003.
- [44] V. Caselles, F. Catte, T. Coll, and F. Dibos, "A geometric model for active contours in image processing," *Numerische Mathematik*, vol. 166, pp. 1-31, 1993.
- [45] R. Malladi, J. Sethian, and V. B., "Shape modeling with front propagation:A level set approach," *IEEE Trans Pattern Anal machine Intell*, vol. 17, pp. 158-175, 1995.
- [46] V. Caselles, R. Kimmel, and G. Sapiro, "Geodesic active contours," *International Journal of Computer Vision*, vol. 22, pp. 61-79, 1997.
- [47] S. Kichenassamy, A. Kumar, P. Olver, A. Tannenbaum, and A. Yezzi., "Gradient flows and geometric active contour models," presented at IEEE ICCV, Boston, 1995.
- [48] A. Yezzi, S. Kichenassamy, A. Kumar, P. J. Olver, and A. Tannenbaum, "A geometric snake model for segmentation of medical imagery," *IEEE Trans. Med. Imag.*, vol. 16, pp. 199-209, 1997.
- [49] S. C. Zhu and A. Yuille, "Region competition:Unifying snakes, region growing, and Bayes/MDL for multiband image segmentation," *IEEE PAMI*, vol. 18, pp. 884-900, 1996.
- [50] T. F. Chan and L. Vese, "A level set algorithm for minimizing the Mumford-Shah functional in image processing," presented at IEEE Computer Society Proceedings of the 1st IEEE Workshop on Variational and Level Set Methods in Computer Vision, Vancouver, Canada, 2001.

- [51] D. Cremers, C. Schnörr, and J. Weickert, "Diffusion-snakes combining statistical shape knowledge and image information in a variational framework," presented at IEEE Intl. Workshop on Variational and Levelset Methods, Vancouver, 2001.
- [52] A. Tsai, A. Yezzi, W. Wells, C. Tempany, D. Tucker, A. Fan, E. Grimson, and A. Willsky, "Model-based curve evolution technique for image segmentation," presented at CVPR, Hawaii, 2001.
- [53] T. Cootes, C. Beeston, G. Edwards, and C. Taylor, "Unified framework for atlas matching using active appearance models," presented at Int'l Conf. Inf. Proc. in Med. Imaging, 1999.
- [54] Y. Wang and L. H. Staib, "Boundary Finding with Correspondence Using Statistical Shape Models," presented at CVPR, Santa Barbara, CA, 1998.
- [55] T. Cootes, C. Taylor, D. Cooper, and J. Graham, "Active shape model--their training and application," *Computer Vision and Image Understanding*, vol. 61, pp. 38-59, 1995.
- [56] T. Cootes and C. Taylor, "Mixture model for representing shape variation," *Image and Vision Computing*, vol. 17, pp. 567-574, 1999.
- [57] L. Staib and J. Duncan, "Boundary finding with parametrically deformable contour methods," *IEEE Trans Patt Analysis and Mach Intell*, vol. 14, pp. 1061-1075, 1992.
- [58] A. Yuille, P. W. Hallinan, and D. S. Cohen, "Feature extraction from faces using deformable templates," *Int J Computer Vision*, vol. 8, pp. 99-111, 1992.
- [59] H. D. Tagare, "Deformable 2-D Template Matching Using implementation of the Mumford-Shah functional for image segmentation, denoising, interpolation, and magnification," *IEEE Trans. on Image Proc.*, vol. 10, pp. 1169-1186, 2001.
- [60] M. E. Leventon, E. Grimson, and O. Faugeras, "Statistical shape influence in geodesic active contours," presented at IEEE Conf. CVPR (2000), 2000.
- [61] Y. Chen, S. Thiruvankadam, F. Huang, H. Tagare, D. Wilson, and A. Geiser, "On the Incorporation of shape priors into geometric active contours," presented at IEEE Workshop in Variational and Level Set Methods in Computer Vision, Vancouver, Canada, 2001.
- [62] Y. Chen, H. Tagare, S. R. Thiruvankadam, F. Huang, D. Wilson, K. S. Gopinath, R. W. Briggs, and A. Geiser, "Using prior shapes in geometric active contours in a variational framework," *International Journal of Computer Vision*, vol. 50, pp. 315-328, 2002.

- [63] N. Paragios, M. Rousson, and V. Ramesh, "Matching Distance Functions: A Shape-to-Area Variational Approach for Global-to-Local Registration," presented at ECCV, Copenhagen, Denmark, 2002.
- [64] N. Paragios and R. Deriche, "Geodesic Active Contours for Supervised Texture Segmentation," presented at CVPR, Cofu, Greece, 1999.
- [65] D. G. Kendall, "Shape-manifolds, Procrustean metrics, and complex projective spaces," *Bulletin London Mathematics Society*, vol. 16, pp. 81-121, 1984.
- [66] C. G. Small, *The Statistical Theory of Shape Springer Series in Statistics*. New York: Springer-Verlag, 1996.
- [67] E. A. Geiser, D. C. Wilson, D. Wang, D. A. Conetta, J. D. Murphy, and A. D. Hutson, "Autonomous epicardial and endocardial boundary detection in echocardiographic short-axis images," *Journal of the American Society of Echocardiography*, vol. 11, pp. 338-348, 1998.
- [68] P. Thevenaz and M. Unser, "Optimization of mutual information for multiresolution image registration," *IEEE Trans. on Image Proc.*, vol. 9, pp. 2083-2099, 2000.
- [69] P. Viola and W. M. Wells, "Alignment by maximization of mutual information," *IJCV*, vol. 24, pp. 137-154, 1997.
- [70] A. Tsai, J. A. Yezzi, and A. S. Willsky, "Curve evolution implementation of the Mumford-Shah functional for image segmentation, denoising, interpolation, and magnification," *IEEE Trans. on Image Proc.*, vol. 10, pp. 1169-1186, 2001.
- [71] N. Paragios, "Geodesic Active Regions and Level Set Methods: Contributions and Applications in Artificial Vision," in *School of Computer Engineering*. Nice, France: University of Nice/Sophia Antipolis, 2000.
- [72] N. Paragios, "A variational approach for segmentation of the left ventricle in MR cardiac images.," presented at 1st IEEE Workshop on Variational and Level Set Methods in Computer Vision, Vancouver, B C, 2001.
- [73] T. Cootes, C. Taylor, D. Cooper, and J. Graham, "Active shape model - their training and application," *Computer Vision and Image Understanding*, vol. 61, pp. 38-59, 1995.
- [74] J. A. Sethian, "Fast marching methods," *SIAM Review*, vol. 41, pp. 199-235, 1999.
- [75] B. C. Vemuri, Y. Chen, and Z. Wang, "Registration Assisted Image Smoothing and Segmentation," presented at ECCV, Copenhagen, Denmark, 2002.

- [76] F. Richard and L. Cohen, "A New Image Registration Technique with Free Boundary Constraints: Application to Mammography," presented at ECCV, Copenhagen, Denmark, 2002.
- [77] S. Soatto and A. J. Yezzi, "DEFORMATION: Deforming Motion, Shape Average and the Joint Registration and Segmentation of Images," presented at ECCV, Copenhagen, Denmark, 2002.
- [78] M. E. Leventon, O. Faugeras, E. Grimson, and W. Wells, "Level set based segmentation with intensity and curvature priors," presented at Mathematical Methods in Biomedical Image Analysis, 2000.
- [79] C. Ballester, M. Bertalmio, V. Caselles, G. Sapiro, and J. Verdera, "Filling-in by joint interpolation of vector fields and grey levels," *IEEE Trans. on Image Proc.*, vol. 10, pp. 1200-1211, 2001.
- [80] T. F. Chan, J. Shen, and L. Vese, "Variational PDE models in image processing," *Amer. Math. Soc. Notice*, vol. 50, pp. 14-26, 2003.
- [81] T. F. C. a. J. Shen, "Non-texture inpainting by curvature driven diffusions," *J. Visual Comm. Image Rep*, vol. 12, pp. 436-449, 2001.
- [82] V. Caselles, J. M. Morel, and C. Sbert, "An axiomatic approach to image interpolation," *IEEE Trans. Med. Imag.*, vol. 7, pp. 376-386, 1998.
- [83] D. Sodickson, *Spatial Encoding Using Multiple RF Coils: SMASH Imaging and Parallel MRI*: John Wiley & Sons Ltd, 2000.
- [84] K. P. Pruessmann, M. Weiger, M. B. Scheidegger, and P. Boesiger, "Coil sensitivity encoding for fast MRI," presented at 6th Intl. Soc. Mag. Reson. Med, Sydney, Australia, 1998.
- [85] M. Angel, G. Ballester, Y. Machida, Y. Kassai, Y. Hamamura, and H. Sugimoto, "Robust Estimation of Coil Sensitivities for RF Subencoding Acquisition Techniques," presented at 9th Intl. Soc. Mag. Reson. Med, 2001.
- [86] F. H. Lin, Y. J. Chen, J. W. Belliveau, and L. L. Wald, "Estimation of coil sensitivity map and correction of surface coil magnetic resonance images using wavelet decomposition," presented at 9th Intl. Soc. Mag. Reson. Med, Brighton, UK, 2001.
- [87] M. Cohen, R. DuBois, and M. Zeineh, "Rapid and effective correction of RF inhomogeneity for high field magnetic resonance imaging," *Hum Brain Mapp*, vol. 10, pp. 204-211, 2000.
- [88] P. B. Roemer, W. A. Edelstein, C. E. Hayes, S. P. Souza, and O. M. Mueller, "The NMR phased array," *Magn Reson Med*, vol. 16, pp. 192-225, 1990.

- [89] J. W. Murakami, C. E. Hayes, and E. Weinberger, "Intensity correction of phased array surface coil images," *Magn Reson Med*, vol. 35, pp. 585-590, 1996.
- [90] K. P. Pruessmann, M. Weiger, M. B. Scheidegger, and P. Boesiger, "Coil sensitivity maps for sensitivity encoding and intensity correction," presented at 6th Intl. Soc. Mag. Reson. Med, Sydney, 1998.
- [91] S. O. L. Rudin, and E. Fatemi., "Nonlinear total variation based noise removal algorithms.," *Physica D*, vol. 60, pp. 259-268, 1992.
- [92] G. Aubert and L. Vese, "A variational method in image recovery," *SIAM J. Numer. Anal*, vol. 34, pp. 1948-1979, 1997.
- [93] C. A. McKenzie, E. N. Yeh, M. A. Ohliger, M. D. Price, and D. K. Sodickson, "Self-Calibrating Parallel Imaging With Automatic Coil Sensitivity Extraction," *Magn Reson Med*, vol. 47, pp. 529-538, 2002.
- [94] V. Heels-Bergen, R. Teunis, Fuderer, and Miha, "Magnetic resonance imaging method and apparatus." USA: US Philips Corporation, 1996.
- [95] K. Paulson, W. Breckon, and M. Pidcock, "Optimal measurements in electrical impedance tomography," *IEEE EMBS*, vol. 14, pp. 1730, 1992.
- [96] M. Vauhkonen, D. V. asz, P. A. Karjalainen, E. Somersalo, and J. P. Kaipio, "Tikhonov Regularization and Prior Information in Electrical Impedance Tomography," *IEEE Trans. Med. Imag.*, vol. 17, pp. 285-293, 1998.
- [97] G. T. Herman and L. Meyer, "Algebraic reconstruction techniques can be made computationally efficient," *IEEE Trans. Med. Imag.*, vol. 12, pp. 600-609, 1993.
- [98] A. M. Cormack, "Representation of a function by its line integrals, with some radiological applications I," *J. Appl. Physics*, vol. 34, pp. 2722-2727, 1963.
- [99] A. M. Cormack, "Representation of a function by its line integrals, with some radiological applications II," *J. Appl. Physics*, vol. 35, pp. 195-207, 1964.
- [100] S. R. Deans, *The Radon Transform and some of its Applications*. New York: Wiley, 1983.
- [101] J. Qi and R. Leahy, "Resolution and noise properties of MAP reconstructions in fully 3D PET," *IEEE Trans. Med. Imag.*, vol. 19, pp. 493-506, 2000.
- [102] T. Hebert and R. Leahy, "A generalized EM algorithm for 3D Bayesian reconstruction from Poisson data using Gibbs distributions," *IEEE Trans. Med. Imag.*, vol. 8, pp. 194-202, 1989.
- [103] T. K. Moon, "The Expectation-Maximization algorithm," *IEEE Trans Signal Processing*, vol. 13, pp. 47-60, 1996.

- [104] J. A. Bilmes, "A gentle tutorial of the EM algorithm and its application to parameter estimation for Gaussian mixture and hidden Markov model," University of California, Berkeley Technical Report ICSI-TR-97-021, 1997.
- [105] R. Leahy and J. Qi, "Statistical approaches in quantitative positron emission tomography," *Statistics and Computing*, vol. 10, pp. 147-165, 2000.
- [106] M. Cheney and D. Isaacson, "A layer-stripping algorithm for impedance imaging," *IEEE EMBS*, vol. 13, pp. 3-4, 1991.
- [107] J. Sylvester, "A convergent layer stripping algorithm for radially symmetric impedance tomography problem," *Comm. Partial Differential Equations*, vol. 17, pp. 1955-1994, 1992.
- [108] E. Somersalo, M. Cheney, D. Isaacson, and E. L. Isaacson, "Layer-stripping: A direct numerical method for impedance imaging," *Inverse Problems*, vol. 7, pp. 899-926, 1991.
- [109] E. L. Miller, M. Kilmer, and C. Rappaport, "A new shape-based method for object localization and characterization from scattered field data," *IEEE Trans. Geoscience and Remote Sensing*, vol. 38, pp. 1682-1696, 2000.
- [110] H. Feng, W. C. Karl, and D. A. Castanon, "A curve evolution approach to object-based tomographic reconstruction," *IEEE Trans. Med. Imag.*, vol. 12, pp. 44-57, 2003.
- [111] D. F. Yu and J. A. Fessler, "Edge-preserving tomographic construction with nonlocal regularization," *IEEE Trans. Med. Imag.*, vol. 21, pp. 159-173, 2002.
- [112] T. F. Chan and X. C. Tai, "Level set and total variation regularization for elliptic inverse problems with discontinuous coefficients," *Journal of Computational Physics*, vol. 193, pp. 40-66, 2003.
- [113] A. O. Hero, R. Piramuthu, J. A. Fessler, and S. R. Titus, "Minimax emission computed tomography using high resolution anatomical side information and B-spline models," *IEEE Transactions on Information Theory*, vol. 45, pp. 920-938, 1999.
- [114] T. F. Chan and S. Esedoglu, "A Multiscale Algorithm for Mumford-Shah Image Segmentation," UCLA, Los Angeles cam03-77, Dec 17, 2003 2003.
- [115] F. Gibou and R. Fedkiw, "Fast hybrid k-means level set algorithm for segmentation," *Preprint, in review*, pp. <http://math.stanford.edu/~fgibou>, 2003.
- [116] A. Kaup and T. Aach, "Coding of segmented images using shape independent basis functions," *IEEE Trans. Med. Imag.*, vol. 7, pp. 937-947, 1998.

- [117] M. Eden, M. Unser, and R. Leonardi, "Polynomial representation of pictures," *Signal Process*, vol. 10, pp. 385-393, 1986.
- [118] G. Cusick, D. S. Holder, A. Birkett, and K. G. Boone, "A system for impedance imaging of epilepsy in ambulatory human subjects," *Innov. Tech. Biol. Med.*, vol. 15(Suppl. 1), pp. 34-39, 1994.
- [119] M. Radai, S. Abboud, and M. Rosenfeld, "Evaluation of impedance technique for detecting breast carcinoma using a 2-D numerical model of the torso," *Annals of the New York Academy of Sciences*, vol. 873, pp. 360 - 369, 1999.
- [120] P. Basser, J. Mattiello, and D. LeBihan, "Estimation of the effective self-diffusion tensor from the NMR spin echo," *J. Magn. Reson. B*, vol. 103, pp. 247-254, 1994.
- [121] S. Mori, B. Crain, V. Chacko, and P. C. M. van Zijl, "Three dimensional tracking of axonal projections in the brain by magnetic resonance imaging," *Ann. Neurol.*, vol. 45, pp. 265-269, 1999.
- [122] R. Xue, P. C. M. van Zijl, B. J. Crain, M. Solaiyappan, and S. Mori, "In vivo three-dimensional reconstruction of rat brain axonal projections by diffusion tensor imaging," *Magn. Reson. Med*, vol. 42, pp. 1123-1127, 1999.
- [123] T. E. Conturo, N. F. Lori, T. S. Cull, E. Akbudak, A. Z. Snyder, J. S. Shimony, R. C. McKinstry, H. Burton, and M. E. Raichle, "Tracking neuronal fiber pathways in the living human brain.," presented at Natl Acad. Sci. USA, 1999.
- [124] C. Beaulieu, "The basis of anisotropic water diffusion in the nervous system," *NMR Biomed*, vol. 15, pp. 435-455., 2002.
- [125] S. Mori and P. C. M. v. Zijl, "Fiber tracking: principles and strategies - A technical review," *NMR in Biomedicine*, vol. 15, pp. 468-480, 2002.
- [126] D. S. Tuch, R. M. Weisskoff, J. W. Belliveau, and V. J. Wedeen, "High angular resolution diffusion imaging of the human brain," presented at 7th Intl. Soc. Mag. Reson. Med, Philadelphia, 1999.
- [127] D. S. Tuch, T. G. Reese, M. R. Wiegell, N. Makris, J. W. Belliveau, and V. J. Wedeen, "High angular resolution diffusion imaging reveals intravoxel white matter fiber heterogeneity," *Magn Reson Med*, vol. 48, pp. 577-582, 2002.
- [128] P. J. Basser, S. Pajevic, C. Pierpaoli, J. Duda, and A. Aldroubi, "In vivo fiber tractography using DT-MRI data," *Magn Reson Med*, vol. 44, pp. 625-632, 2000.
- [129] N. F. Lori, E. Akbudak, J. Shimony, T. Cull, A. Snyder, R. Guillery, and T. Conturo, "Diffusion tensor fiber tracking: Methods, experimental results, and error simulations," presented at Diffusion NMR and MRI: From the Single Molecule to the Entire Human Brain., 2001.

- [130] N. F. Lori, E. Akbudak, J. S. Shimony, T. S. Cull, A. Z. Snyder, R. K. Guillory, and T. E. Conturo, "Diffusion tensor fiber tracking of human brain connectivity: acquisition methods, reliability analysis and biological results," *NMR in Biomedicine*, vol. 15, pp. 493-515, 2002.
- [131] G. J. M. Parker, C. A. M. Wheeler-Kingshott, and G. J. Barker, "Estimating distributed anatomical connectivity using fast marching methods and diffusion tensor imaging," *IEEE Trans. Med. Imag.*, vol. 21, pp. 505-512, 2002.
- [132] J. D. Tournier, F. Calamante, D. G. Gadian, and A. Connely, "A novel fibre-tracking technique: front evolution using a fibre orientation probability density function," presented at ISMRM 10th Scientific Meeting & Exhibition, Hawaii, 2002.
- [133] J. A. Sethian, "A fast marching level set method for monotonically advancing fronts," *Proc. Nat. Acad. Sci.*, vol. 93, pp. 1591-1595, 1996.
- [134] Y. Chen, Y. J. Liu, G. J. He, W. Guo, Q. G. Zeng, F. Huang, and X. L. Yan, "Estimation, Smoothing, and Characterization of Appranet Diffusion Coefficient Profiles from High Angular Resolution DWI," presented at 2004 IEEE Computer Society Conference on Computer Vision and Pattern Recognition, Washington ,DC, 2004.
- [135] G. Kindlmann, D. Weinstein, and D. Hart, "Strategies for direct volume rendering of diffusion tensor fields," *IEEE Transactions on Visualization and Computer Graphics*, vol. 6, pp. 124-138, 2000.
- [136] C. Pierpaoli, A. Barnett, S. Pajevic, R. Chen, L. Penix, A. Virta, and P. Basser, "Water diffusion changes in Wallerian degeneration and their dependence on white matter architecture," *NeuroImage*, vol. 13, pp. 1174-1185, 2001.
- [137] D. S. Tuch, "Mapping cortical connectivity with diffusion MRI," presented at IEEE ISBI, Washington, D.C, 2002.
- [138] J.A.Sethian, "A fast marching level set method for monotonically advancing fronts," *Proc. Nat. Acad. Sci.*, vol. 93, pp. 1591-1595, 1996.

BIOGRAPHICAL SKETCH

I was born in Anhui province, China, on March 10, 1973. At the age of seventeen, I finished high school and entered the mathematics Department of Anhui University in the fall of 1989. I received my bachelor's degree in science in July 1993 (as I turned 20 years of age.) In 1996, I obtained a master's degree of engineering in the field of computer aided geometric design (CAGD) from Hefei University of Technology. In the fall of 1996, I took a job at Beijing Forestry University as a mathematics lecturer, where I worked until the 1999.

I joined the Ph.D. program of the Department of Mathematics at the University of Florida in August 1999. The next year, I began work with Dr. Chen on medical image processing. It became apparent to me that this field was the most exciting thing I had encountered in my whole life. Since the spring of 2001, I have worked in Diagnostic imaging, Invivo Corporation, Gainesville on a number of joint projects.